THESIS

ELECTRODEPOSITION AND SPECIATION STUDY OF DIFFERENT TRANSITION METAL ANTIMONIDES FOR APPLICATION INTO LITHIUM ION BATTERIES

Submitted by

Jacob Ray Kershman

Department of Chemistry

In partial fulfillment of the requirements

For the Degree of Master of Science

Colorado State University

Fort Collins, Colorado

Fall 2010

Master's Committee:

Department Chair: Ellen R. Fisher

Advisor: Amy L. Prieto

C. Michael Elliott
Matthew J. Kipper

ABSTRACT

ELECTRODEPOSITION AND SPECIATION STUDY OF DIFFERENT TRANSITION METAL ANTIMONIDES FOR APPLICATION INTO LITHIUM ION BATTERIES

Several new deposition setups were designed and tested to increase the uniformity of depositions of Cu_2Sb. It was shown that the jacketed beaker setup produces the most uniform films compared to other setups used. This setup was used to obtain the average thickness and mass measurements of a triplicate set of films deposited at deposition times of 1, 2.5, 5, 7, and 10 minutes. The thickness (determined by AFM) and weight were both linear and corresponded to a growth rate of 300 nm per minute or 0.2 mg of Cu_2Sb per minute. Preliminary battery testing revealed that the thinner films cycled much better than thicker films. Films thicker than ~1 μm did not cycle well at all, and cleaved completely off the surface of the electrode during cycling.

Cu_2Sb was successfully electrodeposited into commercial alumina filters. The Cu_2Sb wires were ordered in a different direction compared to the electrodeposition on planar substrates ([101] versus [001] direction). A two step anodization process was shown to produce self-ordered AAO templates with pore sizes between 30 and 40 nm. It was shown that the mechanical and electrochemical polishing steps are not necessary to obtain the self-ordered templates. Promising results have been shown with multiple methods to break through the barrier layer of these alumina templates. Even when the barrier layer is removed a native oxide is formed within a few seconds on the surface of

the aluminum which blocks the electrodeposition of copper. The backside of the template indicated that the breakthrough was only in localized spots.

Previously, crystalline Cu_2Sb was electrodeposited at single potential through the complexation of the metals in aqueous solution using citric acid at pH 6. This direct electrodeposition is unusual for intermetallic materials and the reason for the Cu_2Sb case is not well understood. In order to determine why this material deposits under these solution conditions, a deeper understanding of the speciation in solution must be obtained. To study what metal-ligand complexes are present in the Cu-Sb-Citrate deposition, solution electrospray ionization mass spectrometry (ESI-MS) was employed. ESI-MS results were shown to be a qualitative technique to study the solution chemistry of the Cu_2Sb system. These results have been compared to speciation calculations, UV-Vis, titrations, and literature results. The heterometallic species [CuSb(HCit)(Cit)], previously only reported in solids that had been crystallized out of solution, was discovered in solution through ESI-MS. In addition, ESI-MS data pointed to $[Sb(HCit)_2]^-$ as the most abundant antimony citrate species over previously reported $[SbH_{-1}Cit]^-$. The additional species from ESI-MS gave rise to the development of two new balanced reactions for the deposition of Cu_2Sb, in hope of the realization of understanding why Cu_2Sb deposits.

By understanding the solution chemistry, other transition metal antimonides were electrodeposited from aqueous citrate solutions. It is shown that through the co-deposition reaction, which is dependent on the solution chemistry and the fast interstitial diffusion of metals through antimony diffusion in the solid state, many different intermetallic antimonides can be deposited including: crystalline NiSb, the co-deposition

of FeSb, and several copper-rich copper antimonide phases including $Cu_{11}Sb_3$, Cu_4Sb, $Cu_{0.95}Sb_{0.05}$, and possibly other mixed copper antimonide phases. This leads to a better understanding of the electrodeposition of the Cu_2Sb system, which can lead to further improvement of the electrodeposition other transition metal antimonides and intermetallics.

ACKNOWLEDGEMENTS

Graduate school is an endeavor that involves many people. Since starting my journey at CSU I have been surrounded by people that helped form me into a better scientist, thinker, and person. I would like to acknowledge all of the teachers, friends, and people along the way that have made this possible, including all of the unofficial advisors throughout my education that pushed me to achieve more then I dreamed possible.

I would like to thank Dr. Derek Johnson, Dr. James Mosby, Shannon Riha, Dan Shissler, and the rest of the Prieto Group for many helpful discussions, training, constructive criticism, and good times. In addition, I would like to thank the reviewers of this thesis and the time they spent changing the words around to make them sound better and finding those overlooked mistakes. I also appreciate the constructive criticism of my committee members and the push they gave me to think about my project deeper and probe further, in order to understand the interaction of the all components with more breadth. I would like to thank Drs. Pat McCurdy and Sandeep Kohli (Central Instrument Facility) with their assistance with the SEM, EDS, and XRD. In addition, I would also like to thank Don Dick for his valuable help with the mass spectrometer. Most importantly, this work would not have been possible without the help of Dr. Amy Prieto. I want to thank her for her valuable input, patience, and providing me the opportunity to work on this project.

Finally, this would not have been possible without the work ethic instilled in me by my parents. I appreciate them always pushing me farther by encouraging me to work to the best of my abilities, no matter what. Ultimately, to my love and best friend, Sherry: your support, patience, and help were always more than I deserved. You are the best wife I could ask for. May God, who has guided us together on our journey and blessed us so generously, continue to provide us with new opportunities and generosity in the future. With God, all things are possible.

TABLE OF CONTENTS

LIST OF TABLES

LIST OF FIGURES

LIST OF ACRONYMS

AAM	Anodized Alumina Membranes
AAO	Anodic Aluminum Oxide
AC	Alternating Current
ACS	American Chemical Society
AFM	Atomic force microscopy
AGC	Automatic Gain Control
ASME	American Society of Mechanical Engineers
CE	Current Efficiency
CE	Collision Energy
CID	Collision Induced Dissociation
Cit	Citrate
CRM	Charged Residue Model
CV	Cyclic Voltammogram
DC	Direct Current
DEC	Diethyl Carbonate
DMC	Dimethyl Carbonate
EC	Ethylene Carbonate
EDS	Energy Dispersive X-ray Spectroscopy
ESI-MS	Electrospray Ionization Mass Spectroscopy
EXAFS	X-ray Absorption Fine Structure Spectroscopy
FE	Faradic Efficiency
IEM	Ion Evaporation Model
ISO	International Organization for Standardization
IT	Injection Time
M-L	Metal-Ligand Complex
NMR	Nuclear Magnetic Resonance
OCP	Open Circuit Potential
PAA	Porous Anodic Alumina
PFA	Perfluoroalkoxy
PSA	Pressure Sensitive Adhesive
RMS	Root Mean Square
SEI	Solid Electrolyte Interface
SEM	Scanning Electron Microscope
SSCE	Saturated Sodium Calomel Electrode
TEM	Transmission Electron Microscopy
TIC	Total Ion Count
UV	Ultraviolet
Vis	Visible
WE	Working Electrode
XPS	X-ray Photoelectron Spectroscopy
XRD	X-ray Diffraction

1. Chapter 1 - Electrodeposition of Cu_2Sb and the Effect of Thickness on Battery Cycling Performance

1.1. Introduction

Lithium ion (Li-ion) battery research has increased dramatically in recent years due to the large applicability of the technology. The research is focused on the ever increasing need for longer battery life and the need to power our many electronic devices and battery powered vehicles. There is a diminishing return on the improvements being made to the current carbon anode based lithium ion battery technology. By switching to a different anode it is possible to increase the Li-ion capacity of the electrode, but many of the alternative anode materials have problems with cyclability. One of the problems with alternative anode materials is a large volume change, that is associated with the lithium intercalation and de-intercalation, which leads to pulverization after a few cycles.

Intermetallic compounds have been studied as alternative anode materials due to their relatively low volume expansion upon lithium intercalation. In particular, Cu_2Sb has been studied as a compound of interest because it has a low volume change when lithium is inserted and copper is extruded. The extruded copper is thought to help with the electrical conductivity and it is the same metal used as the current collector.[1] When the extruded copper is taken into consideration the total expansion is only 94%.[2] This along with a theoretical volumetric capacity of 2,132 mAh mL^{-1} (compared to carbon's 818 mAh mL^{-1}) make Cu_2Sb a very promising anode material.[1] Fransson *et al.* characterized the different phases that Cu_2Sb undergoes upon lithium insertion and proposed the mechanism shown in Figure 1.1.[1]

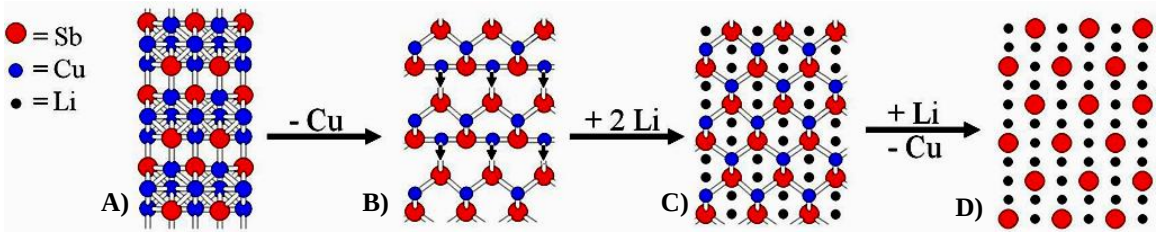

Figure 1.1. Schematic illustrations of the phases formed during the electrochemical transformation of Cu_2Sb to Li_3Sb: (A) Cu_2Sb, [010] projection, (B) "CuSb" component of Cu_2Sb [110] projection, (C) Li_2CuSb [110] projection, and (D) Li_3Sb [110] projection. (Complete reaction: $3Li + Cu_2Sb \rightarrow Li_3Sb + 2Cu$). Reproduced from Fransson *et al.*[1]

Recently, work performed in our laboratory demonstrated a method to produce crystalline films of Cu_2Sb in room temperature, aqueous solutions, by direct electrodeposition.[3] This technique has many advantages over previous preparation methods such as: classical solid state reactions, chemical reduction from solution, ball milling, or pulsed laser deposition techniques.[1, 4-11] One of these advantages is the ability to deposit on a variety of surfaces that can serve a wide range of applications.

During the preliminary work on the electrodeposition of Cu_2Sb it was apparent that the electrodeposition is more sensitive to experimental conditions than common single element depositions, such as the electrodeposition of copper out of an acidic copper sulfate solution. An example of this sensitivity is: the color of the Cu_2Sb films (evidence of film quality) would change from the dark purple color of high quality Cu_2Sb films, and then fluctuate to light purple, grayish-silver, or even black all without the solution composition or any obvious experimental conditions being changed. These problems needed to be addressed in order to produce multiple sets of consistent Cu_2Sb films for the purpose of examining the relationship between film thickness, weight, and the anode cycle performance. With careful control over solution concentrations, which most experimental conditions have, the most obvious variable is the electrode placement. To obtain consistent uniform films, several experimental setups were preformed where

the visual film quality, XRD powder patterns, and current profiles of the depositions were monitored, in order to select the final setup that produced the most uniform Cu_2Sb films.

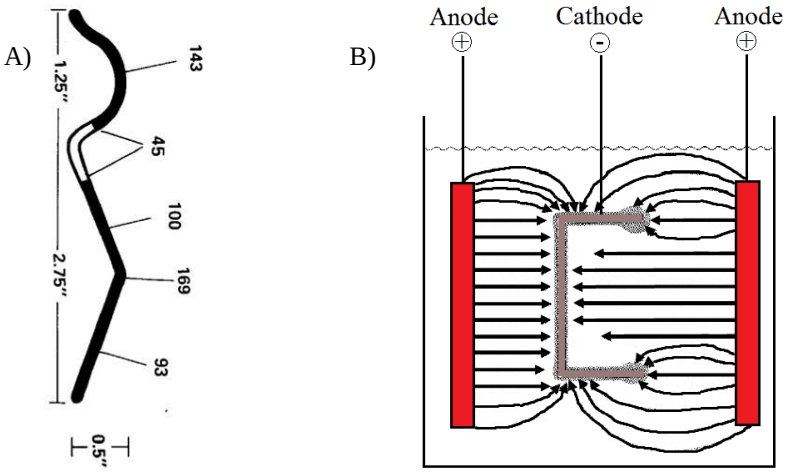

Figure 1.2. The effect of non uniform electric field on the deposition of a film (A) Percent distribution of nickel deposit on a contoured panel. The un-shaded area represents recessed area that was rated separately. The checkpoint is labeled 100% and the other areas describe the percent distribution based on the checkpoint. Reproduced from Dibari *et al.*[12] (B) Non-uniform electric field lines between anode and cathode due to the shape of the substrate, which causes non-uniform current density and metal distribution. Reproduced from Kanani *et al.*[13]

There are two main experimental parameters that affect the uniformity and thickness of a film. These are the surface roughness of the working electrode and the distance or position between the working electrode and the counter electrode. Both of these parameters affect the electric field between the electrodes. The electric field strength ultimately affects the migration of reactants to the surface of the electrode. A high electric field leads to a high current density and a high deposition rate. In turn, the surface roughness affects the electric field, because the electric field lines originate perpendicular to the substrate surface. Dibari *et al.* studied the performance of electrodeposited nickel-chromium coatings on a contoured panel with a cross-section reproduced in Figure 1.2A.[12] From the numbers in Figure 1.2A is it clear that the deposit is thickest at the peaks and thinnest in the recessed areas. The electric field lines originate perpendicular to the substrate surface, so the closer the field lines are to one

another, the stronger the field and more material deposits. This clearly demonstrates that the surface roughness of the substrate affects the uniformity of the deposit. Figure 1.2B shows how a particular "U" shaped substrate affects the electric field lines. Notice how many more arrows are at the sharp points and how non-uniform the electric field lines are dispersed, which in turn changes the thickness of the film distributed on the surface.[13]

The positioning between the working and counter electrodes affect the electric field as well, since the resistance between the electrodes is proportional to the distance separating the electrodes. Thus, if this distance is short, the resistance between the electrodes will be small and the field strength at the electrode's surface will be high. Slight changes in the roughness of the substrate influences the deposition to a point, but it is important to note that depending on how rough the surface is (in our case we used a well polished electrode), the electrode will appear flat on the scale of the diffusion layer after the first few seconds of the deposition, so the slight roughness of a polished film will be negligible.

One way to reduce a non-uniform electric field leading to irregularities in the deposition quality and thickness is to use a high surface area electrode, place the electrodes at the same distance apart, and keep the electrodes parallel to one another. These parameters were investigated in order to determine the effect that they have on the Cu_2Sb deposition in order to achieve reproducible film quality for battery cycling and to better understand the growth rate.

1.2. Experimental

The electrodeposition solution was prepared using units of molality (m) rather than molarity (M), (added a specified amount of solvent before the addition of the solutes). The following were combined and dissolved with the aid of mechanical stirring

for 48 hours: doubly deionized 18Ω water (Milli-Q Plus System, 4-bowl, Millipore) 0.025 m antimony (III) oxide (Sb_2O_3 nanopowder, <250 nm particle size (BET), ≥99.9% trace metals basis, Sigma Aldrich) and 0.4 m anhydrous citric acid (denoted H_3Cit, puriss. p.a., 99.5+%, ACS reagent, Sigma Aldrich). After the Sb_2O_3 dissolved, 0.075 m Copper (II) Nitrate Trihydrate ($Cu(NO_3)_2 \cdot 3H_2O$, purum. p.a., 98.0-103% RT, Sigma Aldrich) was added. Solutions changed from clear to light blue following the addition of Cu. This solution can be stored indefinitely with no noticeable degradation in performance. The pH probe (Thermo Orion 9157 BNMD Orion triode 3-in-1 pH electrode equipped with auto temperature compensation) was calibrated with buffers of pH 1.68 (Orion potassium tetraoxalate dehydrate buffer), 4.00 (Fisher potassium biphthalate buffer), 7.00 (potassium phosphate monobasic-sodium hydroxide buffer), and 10.00 (potassium carbonate-potassium borate-potassium hydroxide buffer) using a Thermo Orion 3 star series pH meter. The solution was brought to pH 6.0 with saturated KOH, at which time the solution became much darker blue. The solution was heated to a temperature between 45-55 °C for the depositions.

SEM images were taken with a JEOL JSM-6500F equipped with an energy dispersive X-ray spectroscopy (EDS) detector from Thermo Electron. Images were taken at 15 kV. For thickness studies, atomic force microscopy (AFM, Nanosurf Easyscan 2, Nanoscience Instruments) was performed in contact mode using single crystal silicon tips (Aluminum reflex coating, tip height 14μm, radius < 10 nm, resonant frequency 190 kHz, spring constant 48 N/m). AFM images and average line data were processed using Scanning Probe Image Processor, SPIP™, (Image Metrology) software version 4.2.2.0. Surface roughness values were derived from the AFM images using ten-point height roughness (Rz) and the root mean square (RMS) roughness (Rq) using American Society

Of Mechanical Engineers (ASME) B46.1 and International Organization for Standardization (ISO) 4287 standards.[14-15] A minimum of two images were taken for each sample in each trial of the thickness study.

The electrodepositions and open circuit potential (OCP) measurements were completed on a Gamry Instruments, Reference 3000, controlled by Gamry Framework version 5.60 software, using a three electrode set up, consisting of the following electrodes: (1) a saturated sodium calomel electrode (SSCE) reference electrode (+0.236 V versus standard hydrogen electrode), (2) copper working electrode (details described below), and (3) 25 x 25 mm platinum gauze (Aldrich, 52 mesh, 99.9% trace metals basis) counter electrode. The Cu_2Sb was deposited on copper foil (0.25 mm thick, 99.98% metals basis, Sigma Aldrich) punched out in 5/8 inch circles. Some of the copper electrodes were mechanically polished to a mirror finish by first attaching the copper to a brass slug with Crystalbond™ adhesive (509 Amber, Aremco Products). Upon cooling, the copper was mechanically polished (Buehler) with 3 µm followed by 1 µm diamond paste (MetaDi Supreme, Buehler USA) on 8" Microcloth with pressure sensitive adhesive (PSA) (Buehler). The paste was kept wet during the process using MetaDi fluid (extender for diamond abrasive, Buehler).

1.3. Results

1.3.1. Preliminary Characterization of Cu_2Sb depositions

In common electrodeposition procedures uniform films are obtained from solutions that are stirred during the deposition.[13, 16] When the diffusion layer thickness becomes excessively large, the diffusion of species to the surface will be perturbed due to convective currents (from heating solution and vibrational noise from the environment) and density gradients (from reduced species near the surface), which will lead to un-

uniform diffusion to the electrode surface causing un-uniform film deposition.[17] Interestingly, it is important that the solution is NOT stirred for the electrodeposition of Cu_2Sb. XRD powder patterns of films deposited from solutions that are stirred match closest to $Cu_{11}Sb_3$, or another copper-rich copper antimonide phase (since many have very similar peak positions) rather than Cu_2Sb. The copper rich phases obtained from stirred solutions could be an indication that stirring replenishes a copper species to the surface of the working electrode faster than occurs in static solutions. See Chapter 4 for more discussion on the deposition of copper-rich copper antimonide compounds. The powder pattern comparing a deposition in a static solution versus a stirred solution is shown in Figure 1.3.

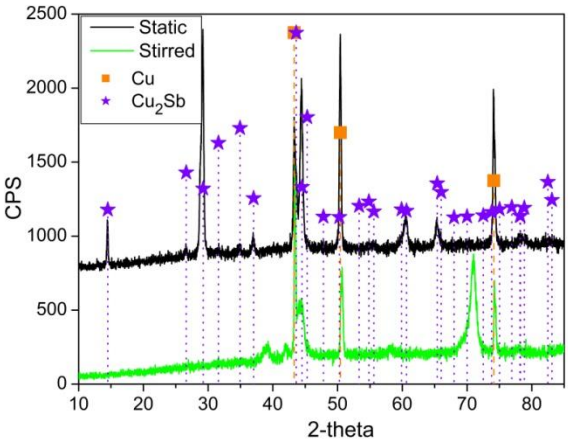

Figure 1.3. XRD powder pattern of deposition preformed in a stirred solution (top) compared to static solution (bottom). Films deposited at -1.05 V versus SSCE in 0.025 m Sb_2O_3, 0.075 m $Cu(NO_3)_2 \cdot 3H_2O$ and 0.4 m citric acid brought to pH 6.0 with KOH. The stirred solution does not produce the Cu_2Sb product, rather a copper-rich, copper antimonide phase.

There is a pronounced difference in the crystallinity of the electrodeposited films on polished versus non polished substrates as shown in Figure 1.4A. The polished films have a higher peak height and sharper, more narrow peaks. The polished films also have a preferred orientation in the (00ℓ) direction: (001), (002), (003), (004), and (005). This plane is parallel to the substrate, which means that the smoother surface allows for the

Cu_2Sb material to be deposited in layers building on top of the substrate. The films produced look visibly uniform, which is confirmed under magnification. Images of Cu_2Sb films deposited for one minute on a polished copper substrate are shown in Figure 1.4B and C.

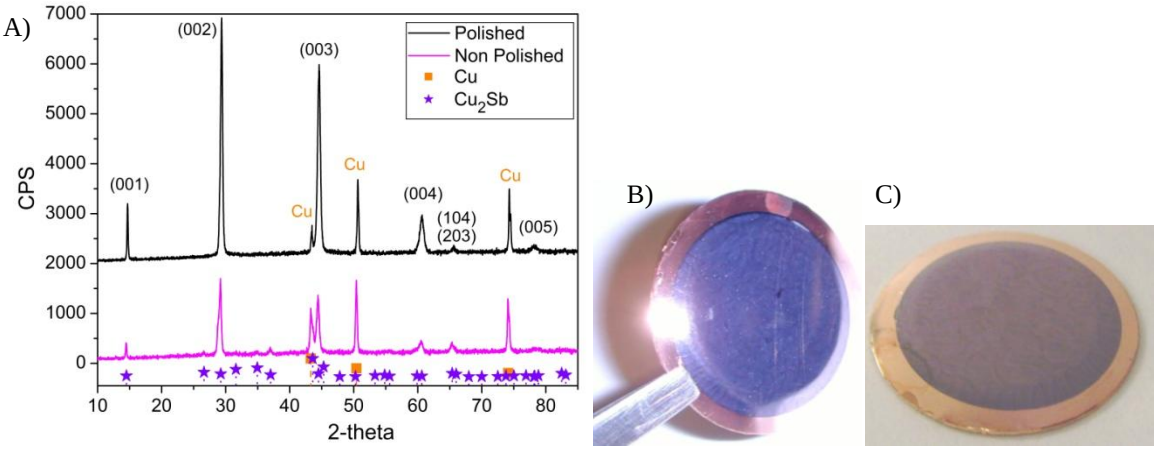

Figure 1.4. Cu_2Sb deposited on polished versus non polished copper substrate. A) XRD powder patterns of Cu_2Sb electrodeposited on polished versus non polished copper substrates for 10 minutes. B) and C) Digital images of Cu_2Sb electrodeposited for one minute on polished substrate. Films deposited at -1.05 V versus SSCE in 0.025 m Sb_2O_3, 0.075 m $Cu(NO_3)_2 \cdot 3H_2O$ and 0.4 m citric acid brought to pH 6.0 with KOH.

1.3.2. Deposition Setup Designs and Modifications

In order to test the battery performance of the Cu_2Sb in Swagelok-type cells, a modified perfluoroalkoxy (PFA) Swagelok tube fitting (union, 1/2 in. tube fitting, PFA-820-6) was used as the working electrode for the electrodeposition of Cu_2Sb. The set up previously used to deposit Cu_2Sb is shown in Figure 1.5A and is called the parallel plate method.[3] The back of the copper working electrode is covered in nail polish and the bare side is placed parallel to the high-surface-area counter electrode. The corresponding current profile of a Cu_2Sb deposition, performed in this setup, is shown in Figure 1.6A. The current reaches a higher steady-state value than the other current profiles shown in Figure 1.6 since the area of this particular electrode was larger than the area of the electrodes in the Swagelok setup. While this is a common means to perform

electrodeposition, it does not fit the design parameters of the Swagelok cell and it requires special consideration to maintain a consistent distance between the working and counter electrodes. The progression of cell designs incorporating the Swagelok union working electrode is shown in Figures 1.5B-F. The corresponding current profiles of the deposition curves are shown in Figure 1.6B-F. A brief discussion of the short comings of each setup will be given below.

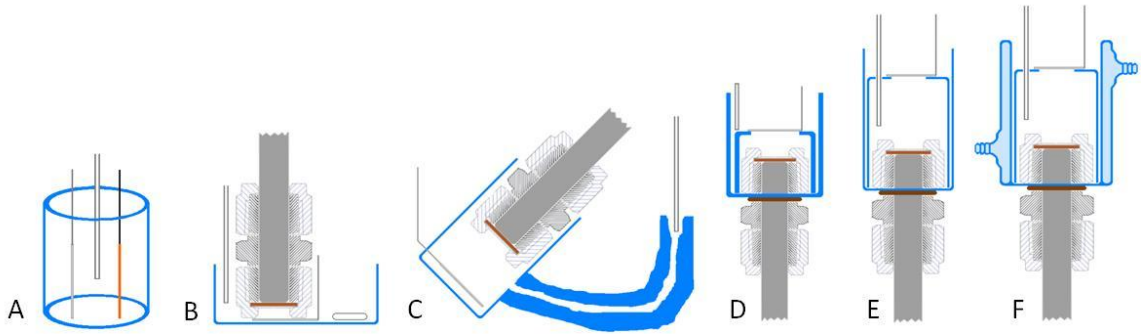

Figure 1.5. Different Cell designs used to deposit Cu_2Sb films. A) Setup A was the original parallel plate method. B-E) Different modified Swagelok setups. F) Jacketed upside down Swagelok set up.

Looking at the cell design in Figure 1.5B it becomes obvious that any gas formation at the counter electrode will diffuse to the working electrode and get trapped. This slowly creates a barrier between the surface of the working electrode and the deposition solution, and after 20 seconds the current profile decays as shown in Figure 1.6B. Furthermore, the reference electrode is not at an ideal position relative to the working electrode. The next modification led to the cell design shown in Figure 1.5C. This cell design alleviated the trapping of gas formed at the counter electrode, but as seen in Figure 1.6C this setup still suffered from a slight decay in the current profile over time, which means that the deposition current is not reaching a steady state and the film will not be uniform.

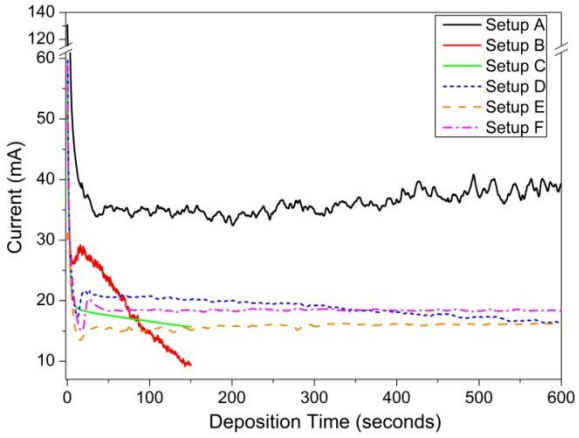

Figure 1.6. Current profiles of films deposited in different cell designs. All films deposited at -1.05 V versus SSCE in 0.025 m Sb_2O_3, 0.075 m $Cu(NO_3)_2 \cdot 3H_2O$ and 0.4 m citric acid brought to pH 6.0 with KOH. The labeling of the current profile corresponds to the labeling of cell designs shown in Figure 1.5. The deposition set up significantly effects the current profile, which has a direct correlation to the thickness and uniformity of the Cu_2Sb films deposited. Setup E and F has the flattest most uniform current profile.

The next step in cell design is shown in Figure 1.5D, which produces uniform films for deposition times under 2.5 minutes, however, problems arose at long times indicated by the current profile (Figure 1.6D) where it started to decay after approximately 5 minutes. This decay in current shows that something was changing in the deposition and film quality would suffer. Another short coming of the cell setup shown in Figure 1.5D is that the reference electrode is near the counter electrode, which increases the difference between the potential being applied to the working electrode and the desired potential, producing non-uniform films. The next modification permitted a larger volume of electrolyte to be added between the working and the counter electrodes, as seen in the cell design shown in Figure 1.5E. In addition, the reference electrode was placed closer to the working electrode. This cell design produced uniform films with the current reaching a steady state value even for a 20 minute deposition. The setups shown up to this point did not address the solution cooling slowly over time. To keep the solution at a constant temperature, the next cell modification led to the cell design shown in Figure 1.5F. The jacketed condenser in Figure 1.5F kept the temperature stable to

within 52 ± 0.5 °C for hours at a time. The steady state current obtained from depositions performed out of the setup shown in Figure 1.5F is higher than the steady state current obtained from depositions perform out of cell shown in Figure 1.5E. This is most likely due to the greater control over the temperature of the deposition bath with the modified setup and higher deposition rates due to the increased temperature.

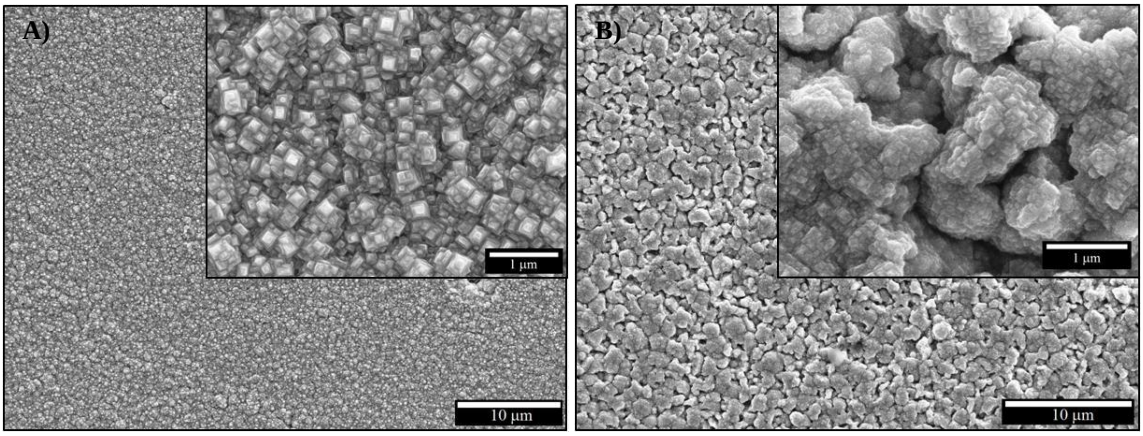

Figure 1.7. SEM images showing the effect of impurities on film morphology. A) A Cu_2Sb film which appears dark purple to the naked eye. B) A Cu_2Sb film which appears light purple to the naked eye. The insets of A and B (scale bars 1 μm) are close ups showing the surface topography. All films deposited at -1.05 V versus SSCE in 0.025 m Sb_2O_3, 0.075 m $Cu(NO_3)_2 \cdot 3H_2O$ and 0.4 m citric acid brought to pH 6.0 with KOH.

Although the current profile from the deposition carried out in the cell shown in Figure 1.5F looks uniform at long times (Figure 1.6F) and the weights of the deposited films are linear with deposition time, the color of the film is not consistent between different deposition times. Films deposited for times longer than 5 minutes are light purple instead of dark purple, as were the films deposited for times shorter than 5 minutes. When viewed under magnification it can be observed that the films deposited for longer times have a higher surface roughness. The SEM images are shown in Figure 1.7A (short deposition times) and Figure 1.7B (long deposition times). The surface (except for cubic Cu_2Sb structure in the higher magnification image in the inset) of the film deposited at short times (dark purple) is smooth in comparison to the morphology of

the film surface deposited at long times (light purple). The rough surface in Figure 1.7B inset (higher magnification) reveals the same cubic morphology observed in the inset of Figure 1.7A, but with a lower packing density that may indicate that an impurity phase is being deposited along with Cu_2Sb.

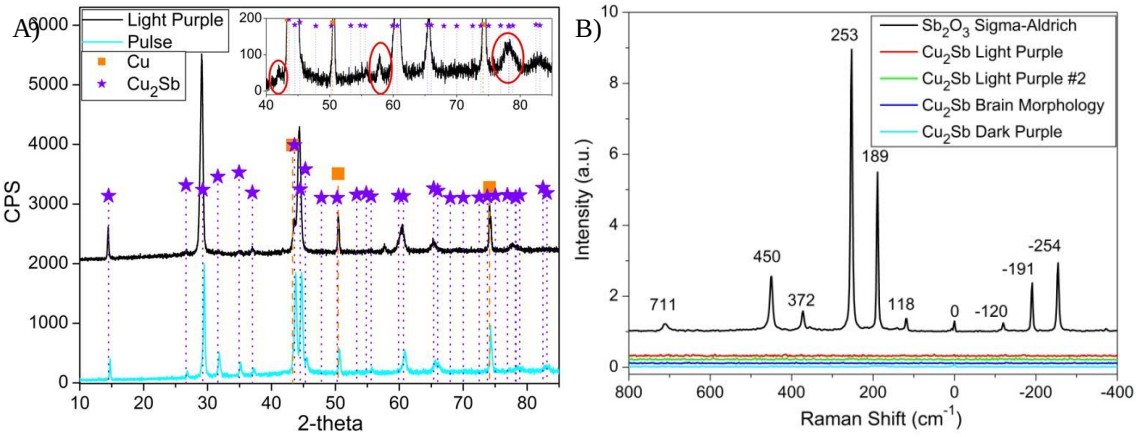

Figure 1.8. Comparison of Cu_2Sb films with different colors using XRD and Raman spectroscopy. A) XRD powder pattern of Cu_2Sb light purple in color films deposited for 10 minutes times (top) compared to that of a Cu_2Sb film electrodeposited using a pulse sequence (bottom). Pulse electrodeposited film contains no impurity peaks, while the rough light purple film in inset shows impurity peaks at 42, 57, and 78º 2-theta. (B) Raman spectrum of Sb_2O_3 (Sigma Aldrich) and Raman spectra of Cu_2Sb films with varying morphology and color show no antimony oxide present. All films deposited at -1.05 V versus SSCE in 0.025 m Sb_2O_3, 0.075 m $Cu(NO_3)_2 \cdot 3H_2O$ and 0.4 m citric acid brought to pH 6.0 with KOH.

XRD powder pattern was used to probe the origin of the different surface morphology and visible color of films deposited at different times. The initial powder pattern of the films deposited at long times identifies only the presence of Cu_2Sb as shown in Figure 1.8A. However, under closer examination there are small impurity peaks present at 42, 57, and 78º 2-theta. An XRD of the same light purple film was taken again, but this time a 4x longer scan was performed. This longer scan (Figure 1.8 inset) highlighted the same three impurity peaks. Identification of these peaks is difficult because they are all very close to a variety of copper-rich copper antimonide compounds as well as different antimony oxides. Both of these impurities could be produced when the diffusion layer thickness grows larger at long deposition times. The copper-rich

copper antimonide compounds have already been shown to be produced when the solution is stirred, which leads to convection currents being the most likely suspect when this diffusion layer thickness is large. Conversely, the antimony oxide phases could be produced by a local pH change near the electrode surface during the deposition. Since the working electrode is positioned horizontally, any Sb_2O_3 precipitate formed from increasing the pH would fall directly to the surface of the electrode and become incorporated into the film. To investigate these two possibilities as to the cause for the light purple films, Raman spectroscopy was performed because antimony oxide is Raman active.

The two common forms of Sb_2O_3 are the cubic phase senarmontite and the orthorhombic phase valentinite. The Raman spectrum in Figure 1.8B of an antimony oxide (Sb_2O_3 nanopowder, <250 nm particle size (BET), ≥99.9% trace metals basis, Sigma Aldrich) matches the senarmontite phase according to literature results by Zeng *et al.*[18] and are significantly different than the orthorhombic phase Sb_2O_3 reported by Deng *et al.*[19] As shown in Figure 1.8B none of the samples of electrodeposited Cu_2Sb, regardless of their morphology or color, give any Raman peaks that match what is reported in the literature for both antimony oxide phases. Looking back at the powder XRD pattern in Figure 1.8A, all the peaks match different copper-rich copper antimonide phases, but one at 77.5º 2-theta, that does not closely match any antimony oxide phase. The Raman and XRD results, combined with the logic of convection currents causing mixing at long deposition times, lead to the conclusion that the copper-rich copper antimonide species as the most likely reason for the rough morphology.

To alleviate the problem of impurity inclusion at long deposition times, a different deposition technique was applied. Since the films deposited for a short amount of time

were dark purple and did not have these other phases present, a potential pulse deposition procedure was used. The pulse deposition consisted of switching the potential on at -1.05 V versus SSCE for a specified amount of time (between 20 and 40 seconds) after which the potential was shut off and the OCP was measured. When the OCP became relatively constant (usually after 1 to 2 minutes) the potential was cycled on again at -1.05 V versus SSCE. This process was repeated until the total on (deposition) time specified was achieved. This method produced dark purple smooth films with no impurity peaks in the XRD for all deposition times tested up to 10 minutes. A representative XRD powder pattern for the pulsed deposition is shown in Figure 1.8A (bottom).

1.3.3. Implementation of Final Design for Growth Rate Study

Pulse deposition achieves the desired uniform product, however, a second desire is to study the film deposited to understand film growth, which should be done at constant deposition potential. Based on the experiments discussed above, the cell design shown in Figure 1.5F does not produce impurity free Cu_2Sb from depositions carried out at all of the desired times. To accomplish this, it was decided to revert back to the parallel plate method (Figure 1.5A). The same polished high purity copper circles used in the Swagelok working electrode were used in the new deposition cell setup shown in Figure 1.9A, but they were masked using Kapton® Polyimide Film with silicone adhesive cut into donuts with an opening of diameter of 13/32 inches (1.0” outer diameter x 13/32” inner diameter, CS Hyde Company). Figure 1.9B shows the working electrode setup with copper backing attached to the polished working electrode using a Kapton tape mask.

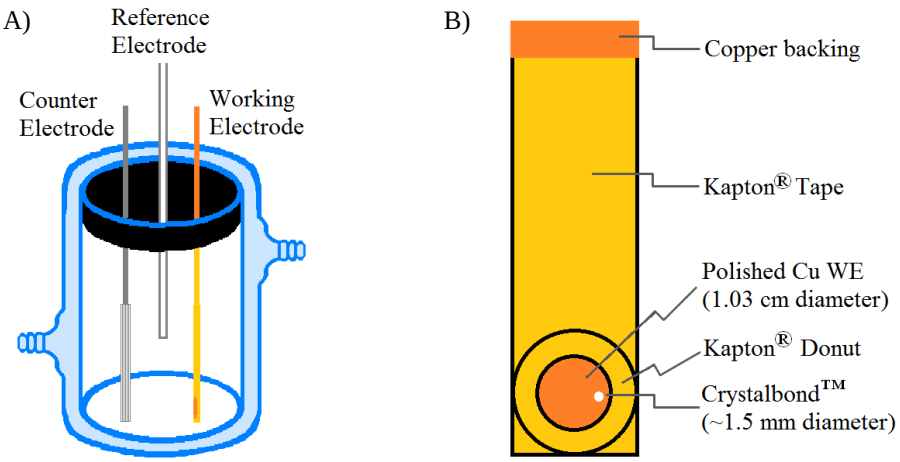

Figure 1.9. A) Final jacketed beaker deposition cell design. B) Modified polished copper working electrode used for depositions.

To determine if this final cell design fits the design parameters to obtain uniform films, the current transients from depositions conducted using this cell design were compared to the previous Swagelok design in Figure 1.5F. Figure 1.10 compares the current profile of the jacketed Swagelok based deposition cell (Figure 1.5F) to the jacketed beaker deposition cell setup (Figure 1.9). The jacketed beaker deposition cell setup has the expected current transient in which there is an initial current increase due to double layer charging, nucleation and growth, followed by the decay as the deposition becomes diffusion limited and reaches a steady state. As expected, the current profile of a deposition carried out in the jacketed breaker cell setup looks similar to the current profile in Figure 1.6A, but with less current variability. On the contrary, the current profile of the films deposited in the Swagelok cell setup (Figure 1.5F) has an additional feature (starting at 20 seconds) that occurs after the steady state is close to being reached. This rise in current only occurs when the electrode is placed horizontal in the solution rather than vertical. This increase in current is probably due to a density gradient being established due to the reduction of species at the surface of the electrode, since they can settle within the Swagelok "cup" shape. At the 20 second mark the density gradient is

large enough that the solution starts to turnover and mixes, creating a greater flux of new species to the surface giving the current increase. Because the solution is slowly being mixed due to these gradients, there is a greater flux of copper species to the surface and copper rich impurities are electrodeposited along with Cu_2Sb. This matches well with the previous analysis of the film using Raman and XRD. This comparison enforces the idea that the parallel plate cell is superior to the Swagelok cell to achieve consistently uniform films, which is further supported by the films deposited having a consistent dark purple color and the XRD pattern showing no sign of impurities.

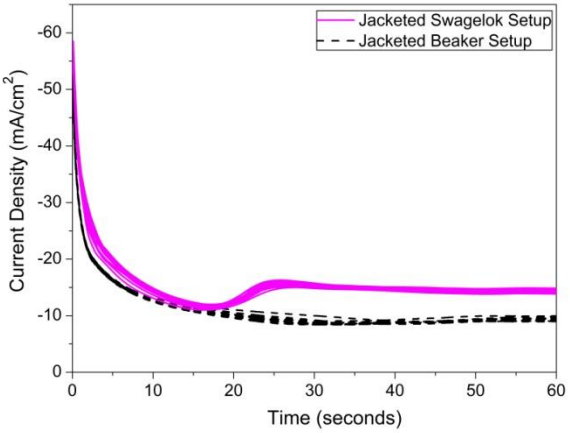

Figure 1.10. Current profiles comparing 16 depositions from the Swagelok cell (Figure 1.5F) to 20 depositions of the jacketed beaker parallel plate cell (Figure 1.9A). All films deposited at -1.05 V versus SSCE in 0.025 m Sb_2O_3, 0.075 m $Cu(NO_3)_2 \cdot 3H_2O$ and 0.4 m citric acid brought to pH 6.0 with KOH.

After finding a deposition cell that produces uniform films, the relationship between deposition time and film thickness can be examined. To accomplish this, films were deposited for five different times: 1, 2.5, 5, 7, and 10 minutes. After the films were deposited, an AFM was used as a profilometer to measure the thickness of the film by scanning over the step edge between the deposited Cu_2Sb and the bare polished copper. An issue that became quickly relevant with the working electrode shown in Figure1.9B is at long times the silicone adhesive of the Kapton tape started to dissolve at the very edge, due to the warm citric acid solvent. The samples deposited at times longer than 5

minutes did not give reproducible thickness measurements due this "bleeding" effect. For this reason, a spot approximately 1.5 mm in diameter of Crystalbond™ 509 adhesive (SPI supplies) was applied as pictured in Figure 1.9B. The Crystalbond adhesive did not dissolve in the citric acid, was easy to apply, and could be removed completely with a brief acetone rinse. The step edge, between the deposited Cu_2Sb and the polished copper substrate left by the Crystalbond, provided consistent measurements of the thickness using the AFM. Figure 1.11 is plot of the average thickness versus deposition time of a triplicate set of films deposited at 1, 2.5, 5, 7, and 10 minutes. The data was processed and analyzed as described in Appendix 1.1, but in brief: several lines crossing the step edge between the Cu_2Sb and the polished copper surface (greater than 10 lines) were averaged using SPIP software, and then the difference between Cu_2Sb and the polished copper surface was measured using Excel. The inset in Figure 1.11 is the corresponding average mass versus deposition time of the corresponding films. The Cu_2Sb film's thickness increases with increasing deposition time at a rate of 300 nm per minute (0.2 mg/min). The error bars are the standard deviation of the three films measured.

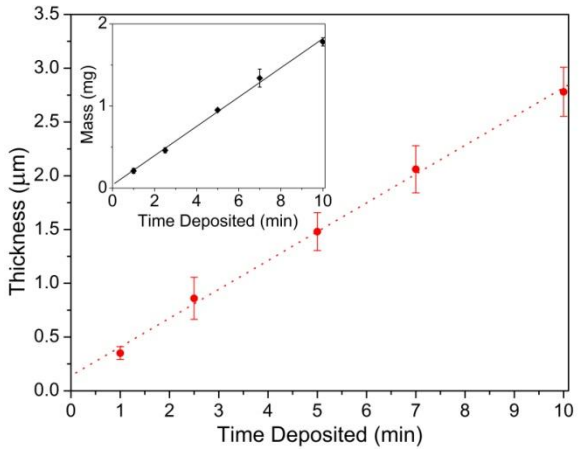

Figure 1.11. Average thickness of three trials of Cu_2Sb deposited at different times measured by AFM. Inset is the average mass and standard deviation of the corresponding films. Films were deposited using cell setup in Figure 1.9. The films were deposited using cell set up in Figure 1.9. All films deposited at -1.05 V versus SSCE in 0.025 m Sb_2O_3, 0.075 m $Cu(NO_3)_2 \cdot 3H_2O$ and 0.4 m citric acid brought to pH 6.0 with KOH.

In order to determine the amount of the error that is due to surface roughness of the film, the AFM data was analyzed to calculate the ten-point height roughness (Rz) and the root mean square (RMS) roughness (Rq) using ASME B46.1 and ISO 4287 standards.[14-15] The ten-point height is defined as the average distance between the 5 highest peaks (z_{pi}) and the 5 deepest valleys (z_{vi}) within the assessment length as shown in equation 1.1. [20]

$$Rz = \left(\frac{1}{5}\sum_{i=1}^{5} z_{pi}\right) - \left(\frac{1}{5}\sum_{i=1}^{5} z_{vi}\right) \qquad \text{Eq. 1.1}$$

The RMS roughness is calculated using equation 1.2, where L is the evaluation length and z is the height.

$$Rq = \sqrt{\frac{1}{L}\int_{0}^{L} z^2(x)dx} \qquad \text{Eq. 1.2}$$

Roughness data was taken from 5 individual lines on the polished copper substrate and the surface of the Cu_2Sb films electrodeposited for different times. The data was collected from two separate AFM images for each deposition time and three films were deposited for each time. Error bars are based on the standard deviation of the roughness calculations for all three trials at each time point (30 lines in total). An interesting observation of the result shown in Figure 1.12 is the films get rougher the longer the depositions were carried out. The ten-point height has a much greater roughness because only the five lowest values are measured where as the average roughness of the entire line is taken into account for the RMS roughness. The RMS roughness is helpful for understanding how the average roughness changes versus deposition time, while the ten-point height is beneficial for looking at the magnitude between the peaks and valleys. A plot depicting what the roughness values represent for

a specific line of one of the films is shown in Appendix 1.2. The roughness plot in Figure 1.12 helps explain the larger error bars at long times as the films become thicker (Figure 1.11).

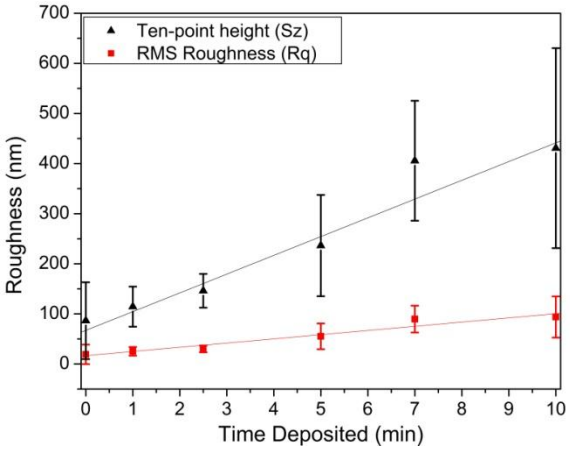

Figure 1.12. Ten-point height roughness (Rz) and the root mean square (RMS) roughness (Rq) using ASME B46.1 standards of films measured for thickness measurement in Figure 1.11. All films deposited at -1.05 V versus SSCE in 0.025 m Sb_2O_3, 0.075 m $Cu(NO_3)_2 \cdot 3H_2O$ and 0.4 m citric acid brought to pH 6.0 with KOH.

More information about the films can be gained by comparing the experimental weights and thicknesses to what the theoretical values should have been based on how much charge was passed during the deposition. Additionally, the efficiency of a deposition can be calculated in what is called: current efficiency (CE)[14] or Faradic efficiency (FE).[21] The calculation for CE is shown in brief below, but a more detailed explanation can be found elsewhere.[16, 21]

Current efficiency can be defined as the number of coulombs passed for the specific process of interest (Q_j) divided by the total number of coulombs passed (Q_{Total}) as shown in Equation 1.3.[16]

$$CE = \frac{Q_J}{Q_{Total}} x\ 100 \qquad \text{Eq. 1.3}$$

An alternative to this is the amount of weight of metal of interest (w_j) deposited divided by the total amount that would have been deposited (w_{Total}) if all of the current went to the deposition of the metal of interest as shown in Equation 1.4.[16]

$$CE = \frac{W_J}{W_{Total}} x\ 100 \qquad \text{Eq. 1.4}$$

Further relating these values into quantities that are measured during the process is shown in Equation 1.5:

$$CE = \frac{\frac{wnF}{A_{wt}}}{It} x\ 100 \qquad \text{Eq. 1.5}$$

where:

w = weight of metal deposited (g)
n = number moles of electrons required to reduce the metal (mol)
F = Faradays constant 96,487 (C/mol)
A_{wt} = molecular weight of metal deposited (g/mol)
I = total current passed (A)
t = time of deposition (seconds)

Now this equation can be modified for alloys by taking into account each metal in the alloy and multiplying by the mole fraction of the alloy of interest as shown in Equation 6:

$$CE = \frac{\left(\frac{wX_{Cu}n_{Cu}F}{A_{wt_{Cu}}}\right)+\left(\frac{wX_{Sb}n_{Sb}F}{A_{wt_{Sb}}}\right)}{It} x\ 100 \qquad \text{Eq. 1.6}$$

Which is equal to the formula in equation 1.7 from Eliaz *et al.* [21]

$$FE = \frac{W}{It}\sum \frac{X_i n_i F}{A_{wt}} \qquad \text{Eq. 1.7}$$

The current efficiency was calculated along with the theoretical weight and thickness. These calculated values and the actual measured values of weight and thickness are shown in Table 1.1 for Cu_2Sb films deposited for different amount of times. The reason for the large standard deviation at short times is due to the relative error in the measurement of the weight of the film. For example: the one minute depositon only has a weight of 0.2 mg, so a change in the weight by just 0.01 mg will change the weight measured by 5%. The weighing error was reduced by weighing the film three times prior

to the deposition and after the deposition. Heavier films have a lower standard deviation, in part, because of this weighing error.

Table 1.1. Average current efficiency as well as average theoretical mass and thickness calculations compared to actual measurements for the triplicate set of Cu_2Sb depositons at the specifed times. One standard deviation is given. All films deposited at -1.05 V versus SSCE in 0.025 m Sb_2O_3, 0.075 m $Cu(NO_3)_2 \cdot 3H_2O$ and 0.4 m citric acid brought to pH 6.0 with KOH.

Time	Current	Weight (mg)		Thickness (μm)	
(min)	Efficiency (%)	Theoretical	Actual	Theoretical	Actual
1	98 ± 15	0.21 ± 0.004	0.21 ± 0.03	0.39 ± 0.01	0.46 ± 0.08
2.5	98 ± 9	0.47 ± 0.02	0.46 ± 0.03	0.86 ± 0.03	0.91 ± 0.05
5	102 ± 8	0.94 ± 0.06	0.95 ± 0.02	1.71 ± 0.11	1.52 ± 0.11
7	102 ± 1	1.32 ± 0.12	1.34 ± 0.11	2.39 ± 0.22	2.37 ± 0.05
10	99 ± 1	1.79 ± 0.06	1.78 ± 0.05	3.25 ± 0.12	3.02 ± 0.12

For the CE calulations only two reactions (reduction of copper and antimony) were taken into account, since the material can be weighed. There is probably some hydrogen evolution and a complicated reduction process occuring that should decrease the efficiency of the deposition. Since some of the values are over 100%, other side reactions would actually decrease, not increase, the efficiency. If the films were copper rich the CE would increase further than what is reported in Table 1.1. However, if the films are slightly antimony rich this would decrease the CE from what is reported. Keeping this in mind, even if the antimony content in the films were increased to a 2:2 from the 2:1 ratio of copper to antimony, the CE from above would only decrease by 5%. If the antimony content is indeed inflated higher than it should be, it must be amorphous, since there is no evidence of crystalline antimony from the powder pattern. To determine the actual amount of antimony present, films deposited at different times should be deposited on gold. The Cu_2Sb films should then be dissolved in nitric acid and then quantitative analysis should be completed using a technique such as atomic absorbance spectroscopy (AAS) to determine the concentration of the metals versus standard solutions.

1.3.4. Preliminary Results on the Thickness Effect on the Cyclability for Cu_2Sb Anode

Through the previous results it was shown that uniform films of Cu_2Sb can be deposited free from impurities in the jacketed beaker design (shown in Figure 1.9A). These films can now be evaluated for anode performance through battery testing. Since it was shown that thickness increases linearly with deposition time, the effect of the thickness of the anode can be evaluated. The films can be cycled between charged and discharged many times to evaluate how the film's capacity holds up over a set of 50 cycles to determine how thickness affects this process.

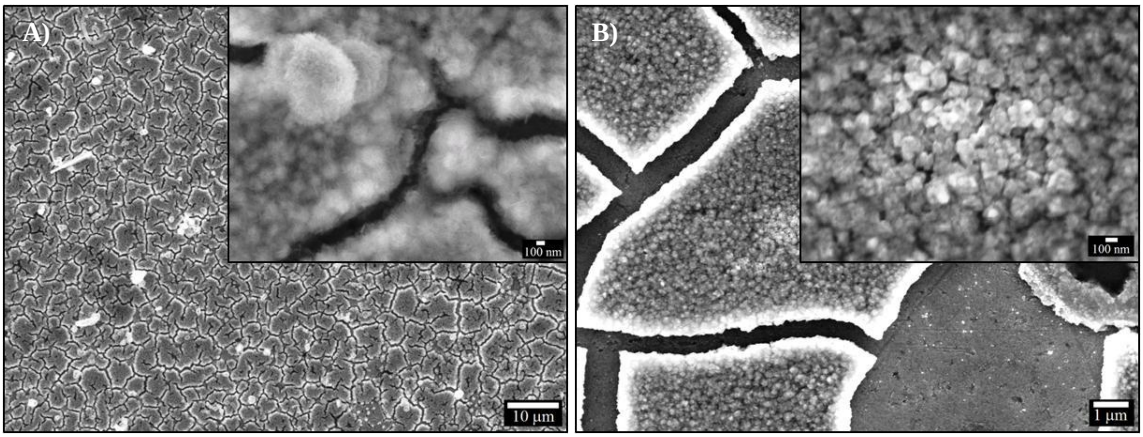

Figure 1.13. SEM of two films deposited for different times after 50 battery cycles (charge and discharge). A) 1 min (~300 nm) B) 2.5 min (~1 µm). The films deposited for greater than 2.5 minutes have pulverized to such an extent that they were lifted completely off the surface. After 50 cycles the SEI layer is completely covering Cu_2Sb particles in the film deposited for 1 min, where the film deposited for 2.5 min is starting to cleave off the surface and does not have a well established SEI layer. Films deposited at -1.05 V versus SSCE in 0.025 m Sb_2O_3, 0.075 m $Cu(NO_3)_2 \cdot 3H_2O$ and 0.4 m citric acid brought to pH 6.0 with KOH. Films were cycled at a rate of gravimetric capacity/5 (11.5 µA for 1 min and 30 µA for 2.5 min) between 0.6 V (discharge) and 1.0 V (charge) versus Li/Li^+ in a solution of 1.0 M $LiPF_6$ ethylene carbonate (EC):diethyl carbonate (DEC):dimethyl carbonate (DMC) (1:1:1 by volume).

The preliminary battery cycling data collected, indicates that the thicker films (greater than 1 µm) do not perform as well as the thinnest films.[22] This is thought to be from the mechanical pulverization of the film from the expansion of the Cu_2Sb crystal lattice upon lithium intercalation.[2] It is helpful to look at the morphology of the battery cycled films under magnification. Figure 1.13 shows the difference between the ~300

nm and the ~1 μm thick Cu_2Sb films under magnification by SEM after 50 cycles of charge and discharge of the anode film. The ~300 nm thick film has very small crystallites that have pulverized from the battery cycling process, but they are kept intact with the solid electrolyte interface (SEI). The ~1 μm thick film has crystallites that are much larger and are not covered with the SEI. Furthermore, there are many places on the film where entire pieces of the Cu_2Sb film have fallen off the surface of the copper. Films thicker than 1 μm do not cycle well at all and completely lose all electrical contact and fall off the surface where they cannot even be analyzed.

1.4. Conclusion

Several new deposition setups were designed and tested for the desire of increased uniformity of Cu_2Sb depositions. It was shown that the jacketed beaker setup (Figure 1.9) produces the most uniform films compared to other setups used. The Swagelok based deposition cell setup (Figure 1.5F) had to be abandoned since the films had a rough morphology that led to a light purple color caused by copper-rich phases of copper antimonide being deposited as confirmed by XRD analysis. It was shown, through Raman spectroscopy, that these rough, light purple films did not contain Sb_2O_3. The copper-rich impurities may have been caused by a combination of convective currents disturbing the large diffusion layer thickness at long times and changes in density from deposition by products left near the electrode surface. These two factors may lead the solution to turnover and behave more like a stirred solution due to convective mixing. It was shown that it is necessary that the films are not stirred or the major electrodeposition product will switch to a copper rich phase, namely $Cu_{11}Sb_3$, rather than Cu_2Sb. The Swagelok set up was only useful if a pulse deposition technique could be applied. The idea of Swagelok cell is good for defining surface area; however, the horizontal

placement of the electrode along with the defining “cup” shape introduces problems: limited diffusion to surface, an interface where species can settle with density changes from electrodeposition, and large issues with convection which is more apparent at longer times.

The jacketed beaker deposition cell setup (Figure 1.9) was used to obtain the average thickness and mass measurements of a triplicate set of films deposited at deposition times of 1, 2.5, 5, 7, and 10 minutes. The thickness (determined by AFM) and weight were both linear and corresponded to a growth rate of 300 nm per minute or 0.2 mg of Cu_2Sb per minute. Preliminary battery testing revealed that the thinner films cycled much better than thicker films. Films thicker than ~1 μm did not cycle well at all, and cleaved completely off the surface of the electrode during cycling.

1.5. References

1. Fransson, L. M. L.; Vaughey, J. T.; Benedek, R.; Edstrom, K.; Thomas, J. O.; Thackeray, M. M., Phase transitions in lithiated Cu_2Sb anodes for lithium batteries: an in situ X-ray diffraction study. *Electrochemistry Communications* **2001,** *3* (7), 317-323.

2. Thackeray, M. M.; Vaughey, J. T.; Johnson, C. S.; Kropf, A. J.; Benedek, R.; Fransson, L. M. L.; Edstrom, K., Structural considerations of intermetallic electrodes for lithium batteries. *Journal of Power Sources* **2003,** *113* (1), 124-130.

3. Mosby, J. M.; Prieto, A. L., Direct Electrodeposition of Cu_2Sb for Lithium-Ion Battery Anodes. *J. Am. Chem. Soc.* **2008,** *130* (32), 10656-10661.

4. Fransson, L. M. L.; Vaughey, J. T.; Edstrom, K.; Thackeray, M. M., Structural transformations in intermetallic electrodes for lithium batteries - An in situ x-ray diffraction study of lithiated MnSb and Mn_2Sb. *Journal of the Electrochemical Society* **2003,** *150* (1), A86-A91.

5. Song, S. W.; Reade, R. P.; Cairns, E. J.; Vaughey, J. T.; Thackeray, M. M.; Striebel, K. A., Cu_2Sb thin-film electrodes prepared by pulsed laser deposition for lithium batteries. *Journal of the Electrochemical Society* **2004,** *151* (7), A1012-A1019.

6. Sarakonsri, I.; Johnson, C. S.; Hackney, S. A.; Thackeray, M. M., Solution route synthesis of InSb, Cu_6Sn_5 and Cu_2Sb electrodes for lithium batteries. *Journal of Power Sources* **2006,** *153* (2), 319-327.

7. Vitkina, T. Z.; Zhigadlo, N. D.; Ryzhkovskii, V. M., Diamagnetism and Some Peculiarities of Interatomic Interactions in Cu_2Sb. *Cryst. Res. Technol.* **1988,** *23* (7), 945-948.

8. Kulifay, S. M., A Low Temperature Synthesis for Powder-form Intermetallics and Other Compounds. **1961,** *83*, 4916.

9. Morcrette, M.; Larcher, D.; Tarascon, J. M.; Edström, K.; Vaughey, J. T.; Thackeray, M. M., Influence of electrode microstructure on the reactivity of Cu_2Sb with lithium. *Electrochimica Acta* **2007,** *52* (17), 5339-5345.

10. Chazova, L., Cathodic Reduction of Antimony(III) in tartrate solutions on a platinum electrode. *Izvestia vyssih ucebnyh zavedenij. Himia i himiceskaa tehnologia* **1978,** *21* (8), 1163-.

11. Ren, J.; He, X.; Pu, W.; Jiang, C.; Wan, C., Chemical reduction of nano-scale Cu_2Sb powders as anode materials for Li-ion batteries. *Electrochimica Acta* **2006,** *52* (4), 1538-1541.

12. DiBari, G. A., Decorative electrodeposited nickel-chromium coatings. Part II. Performance on steel, zinc, plastics and aluminum. *Met. Finish. FIELD Full Journal Title:Metal Finishing* **1977,** *75* (7), 17-24.

13. Kanani, N., *Electroplating - Basic principles, Processes and Practice*. Elsevier: New York, 2004; p 353.

14. (ISO), I. S., Geometrical Product Specifications (GPS) - Surface Texture : Profile method - Terms, Definitions and Surface Texture Parameters. Global Engineering Documents: 1997; Vol. ISO 4287:1997.

15. (ASME), A. S. O. M. E., Surface texture: surface roughness, waviness and lay. 2002; Vol. ASME B46.1

16. Schlesinger, M.; Paunovic, M., Modern Electroplating - Fundamental Considerations. In *Modern Electroplating*, Fourth Edition ed.; Schlesinger, M.; Paunovic, M., Eds. John Wiley & Sons, Inc: New York, 2000; pp 1-60.

17. Bard, A. J.; Faulkner, L. R., *Electrochemical Methods: Fundamentals and Applications*. John Wiley & Sons, Inc: 2001.

18. Zeng, D. W.; Xie, C. S.; Zhu, B. L.; Song, W. L., Characteristics of Sb_2O_3 nanoparticles synthesized from antimony by vapor condensation method. *Mater. Lett.* **2004,** *58* (3-4), 312-315.

19. Deng, Z. T.; Tang, F. Q.; Chen, D.; Meng, X. W.; Cao, L.; Zou, B. S., A simple solution route to single-crystalline Sb2O3 nanowires with rectangular cross sections. *J. Phys. Chem. B* **2006,** *110* (37), 18225-18230.

20. Thomas, T. R., *Rough Surfaces*. Second ed.; Imperial College Press: London, 1999; p 278.

21. Eliaz, N.; Gileadi, E., Induced Codeposition of Alloys of Tungsten, Molybdenum and Rhenium with Transition Metals In *Modern Aspects of Electrochemistry*, Vayenas, C. G.; White, R. E.; Gamboa-Aldeco, M. E., Eds. Springer: New York, 2008; Vol. 42, pp 191-301.

22. Mosby, J. M.; Kershman, J. R.; Prieto, A. L., Effect of Thickness of Cu_2Sb on Battery Cycling Performance. to be submitted for publication, 2010.

2. Chapter 2 – Formation of Anodized Aluminum Oxide Templates and the Penetration of Barrier Layer Oxide.

2.1. Introduction

Nanostructured materials have become increasingly popular since many properties of bulk materials have been shown to change by making the materials nano sized. An additional advantage is that nanostructured materials have increased surface area. Anodic aluminum oxide (AAO) templates also known as anodized alumina membranes (AAM) or porous anodic alumina (PAA), have become increasingly important for the fabrication of nanoscale structures. The popularity of these AAO templates is due in part to their high pore density, up to 10^{11} pores/cm^2.[1] The pores are arranged in a hexagonal array and the diameters can be experimentally varied from 10 nm to over 250 nm.[2] The interpore distances can be varied from 50-420 nm.[3] The thickness of the template is a function of the anodization time and can be grown quite thick to over 200 μm.[4] Another advantage is: they are rigid and resistant to high temperature. However, the template is difficult to remove after using it and is only achieved by chemical solution methods using a strong base or acid.[5]

Templates are prepared through an anodization process in which polished aluminum is oxidized in an acidic solution. The type, concentration, and pH of the acid used, as well as the anodization voltage, and bath temperature all determine pore parameters. Popular electrolytes include phosphoric acid, sulfuric acid, or oxalic acid.[6] The anodization process creates the ordered hexagonal array of pores. At the bottom of

the pore there is an oxide layer over the aluminum, which is called the barrier layer. This is shown in the cartoon adapted from Furneaux *et al.* in Figure 2.1. [2]

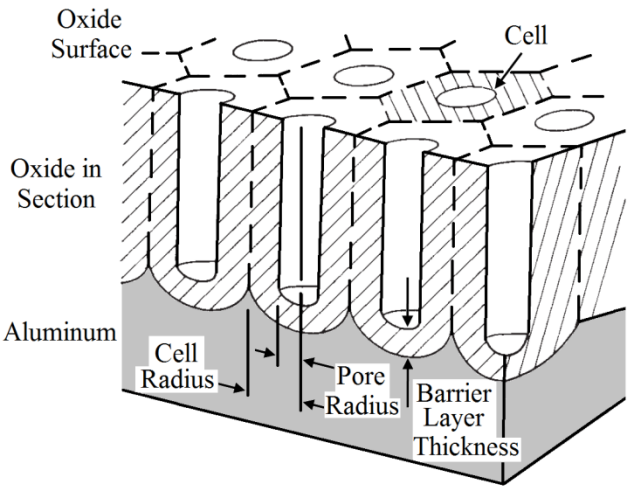

Figure 2.1. Cartoon adapted from Furneaux *et al.* depicting important parts of the alumina template still attached to the aluminum substrate. [2]

The parameters described above all have an effect on the pore structure, however, the electric field caused by the voltage is the parameter that controls the oxide growth and directs the optimum voltage window for a particular acid. The anodization process is described in brief below and can be followed in Figure 2.2 adapted from Hassan *et al.*[7] Initially, Figure 2.2A, there is a small layer of Al_2O_3 between the aluminum and electrolyte. When the electric field is applied, pores will nucleate at the surface of the aluminum in a random fashion from small topographic differences in the aluminum surface. These inhomogenities affect the applied electric field as shown by the arrows in Figure 2.2B. The electric field is strongest where the arrows are closest together and increase the rate of oxidation at these sites, which results in the growth of the oxide deeper into the aluminum as shown in Figures 2.2 C and D.

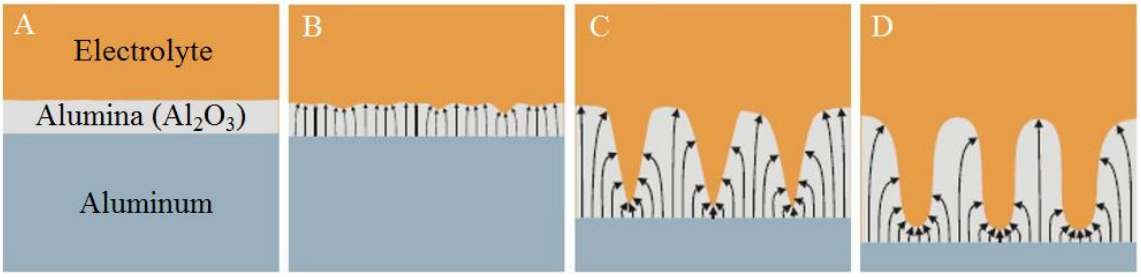

Figure 2.2. Stages in the development of porous alumina during anodization (reproduced from Hassan *et al.*[7]

The exact mechanism of the anodization process is not fully agreed upon in the literature, due to two different ideas about how the oxygen enters the electrolyte, but it is known there is a competition between the oxidation of the aluminum to the aluminum oxide and the dissolution of the oxide by the acid.[8] These two processes can be thought of as the equilibrium of formation and dissolution. At the metal-oxide interface aluminum ions are produced by anodic aluminum oxidation:

$$Al(s) \rightarrow Al^{3+}(aq) + 3e^{-} \qquad \text{Eq. 2.1}$$

At the electrolyte-oxide interface oxygen, O^{2-}, ions are generated through the dissociation of water:

$$H_2O \rightarrow O^{2-}(oxide) + 2H^{+} \qquad \text{Eq. 2.2}$$

The Al^{3+} and O^{2-} ions migrate in the direction of the electric field in opposite directions. They can combine to form Al_2O_3, which occurs near the surface of the aluminum, or the Al^{3+} can go into solution by a simple ion transfer and the oxygen by simple dissolution.[8-9] However, oxygen may go through some kind of oxide decomposition caused by the Al^{3+} ejection into solution since it has been shown that there is no significant loss of O^{2-} by dissolution in some studies.[10-11]

Pores will nucleate at the surface in a random fashion, but at the bottom of the pores they order in a hexagonal arrangement. This ordering is caused by the anodization

voltage and oxide expansion. The anodization voltage influences the rate of oxidation and the rate of expansion, which is due to the fact the oxidation occurs at the bottom of the pore forcing the oxide upwards.[4] Mechanical stress is the cause of the repulsive forces between neighboring pores during the oxidation process and the volume expansion (shown to be 140% of the aluminum[10]). Furthermore, this stress causes viscous flow of the oxide and has been shown to influence the formation of hexagonal pores.[10, 12] Even though much is known about the process, there is still a great deal to fully understand on the self-ordering of the AAO template in order to apply the anodization process to other materials.[10]

With AAO templates it is possible to manufacture large arrays of nanomaterials such as nanowires or nanotubes. The problem with these templates and using them for electrochemical deposition is that the barrier layer (shown Figure 2.2 above) is insulating and too thick (between 10-100nm) for electrons to penetrate to the solution.[6] In the past it has been necessary to remove the aluminum to get to the barrier layer by using a saturated $HgCl_2$ solution[13] , $CuCl_2$ solution[14] , or even $SnCl_4$[15] after which carefully etching the back of the template to remove the barrier layer with a concentrated basic ethylene glycol solution.[13] After the barrier layer is removed a contact such as gold or platinum is thermally evaporated.[13] This process is highly time-consuming and expensive. Recently, it has been proven possible to penetrate the barrier layer *in situ* so that the aluminum metal, that is already present, can be used for the electrochemical deposition of the material.[6, 16-25] Methods vary widely in the literature from completely changing the solution to just applying a different voltage. It is the goal of this work to

find the technique that can punch through the barrier layer for the templates that have been previously made with the double anodization process outlined by Prieto *et al.*[13]

2.2. Experimental

Cyclic Voltammograms (CVs) of copper sulfate solutions were performed on a CH Instruments Model 660C Potentiostat/Galvanostat. CVs were taken in a three electrode cell consisting of the following electrodes: (1) a saturated sodium calomel electrode (SSCE) reference electrode (+0.236 V versus standard hydrogen electrode), (2) platinum disk electrode (2.01 mm^2), and (3) platinum wire (diameter 0.5 mm) counter electrode.

For nanowire deposition gold was evaporated onto alumina templates (Whatman Anodisc membrane filters 13 mm diameter, 0.2 and 0.02 µm pore size). Gold was evaporated onto the back of the electrodes by first evaporating a 5 nm layer of chromium adhesion layer and then 200 nm gold layer using Denton vacuum evaporator with a Maxtek MDC-260 deposition controller. A pulsed electrodeposition technique was used to deposit nanowires using Gamry Instruments Potentiostat/Galvanostat, Reference 3000, controlled by Gamry Framework version 5.60 software.

The anodization process was done using the experimental procedures described in Amy L. Prieto's Dissertation, pages 34-36.[13] Aluminum foil (Alfa Aesar, 0.13mm thick, 99.9995% metals basis) was cut into strips and attached to a brass slug with Crystalbond™ adhesive (509 Amber, Aremco Products). Upon cooling, the copper was mechanically polished (Buehler) with 3 µm followed by 1 µm diamond paste (MetaDi Supreme, Buehler USA) on 8" Microcloth with pressure sensitive adhesive (PSA) (Buehler). The paste was kept wet during the process using MetaDi fluid (extender for

diamond abrasive, Buehler). The film had a mirror finish after mechanically polishing. The pieces of aluminum were placed on a hot plate between 100-200 °C for several hours to form an oxide to protect the aluminum from the electrochemical polishing step. After cooling, the aluminum was punched out with a 5/8" punch and they were placed into a modified perfluoroalkoxy (PFA) Swagelok tube fitting (union, 1/2 in. tube fitting, PFA-820-6) for the remainder of the process. See Figure 2.3 for a diagram of the experimental set up.

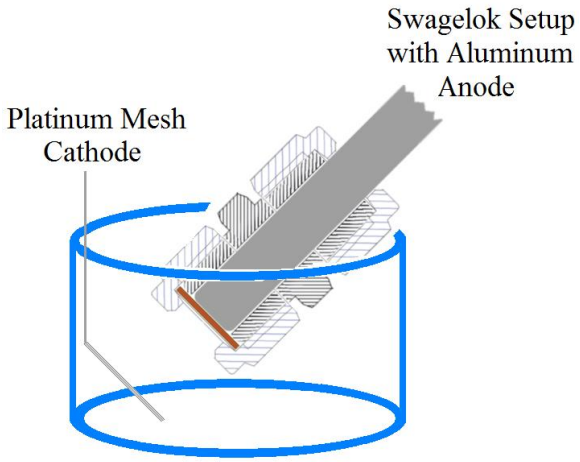

Figure 2.3. Experimental set up of bath used to make the alumina templates.

Electrochemical polishing solution was prepared with 95% phosphoric acid (J.T Baker, 85% H_3PO_4, Baker Analyzed), 5% sulfuric acid (Mallinckrodt, 96% H_2SO_4, ACS) and 20 g/L chromium (VI) oxide, (Sigma Aldrich, 98+% ACS Reagent). The aluminum was electrochemically polished (Topward DC power supply 3603D from SpenceTek Inc.) at 20 V in the polishing solution heated to 85°C for a few seconds. The counter electrode was a 25 x 25 mm platinum gauze (Aldrich, 52 mesh, 99.9% trace metals basis). The current will spike immediately when the power supply is turned on and then will decay rapidly. When the current starts to slow the power supply is switched off.

Afterwards, the electropolished surfaces were much shinier and they could be stored until the samples were ready to be anodized.

Immediately before anodization electropolished alumina were immersed into the cleaning solution prepared by 3.5% phosphoric acid 45 g/L chromium (VI) oxide heated to ~90°C for 2 minutes. This step is done to remove any native oxide that has grown since the electropolish step. Electrodes were rinsed and placed into a 4% w/w (0.444 M) solution of oxalic acid (Alfa Aesar, Oxalic acid dehydrate, ACS 99.5-102.5%), pre-cooled to 2 °C with a water cooler (Brinkmann RM 20 Lauda). The solution containing the platinum gauze electrode was stirred constantly. Aluminum was anodized at 30 V Topward DC power supply 3603D from SpenceTek Inc.) for 2 hours to pre-pattern the aluminum substrate in the hexagonal arrangement. After two hours it was removed from the anodization bath, rinsed, and then the oxide was removed with hot cleaning solution (same composition as above) for 15-20 minutes. The aluminum was rinsed and anodized again for the desired time. This removal of the oxide followed by a second anodization has become known as the double anodization method and is shown in the cartoon in Figure 2.4, adapted from Lee *et al.*[8]

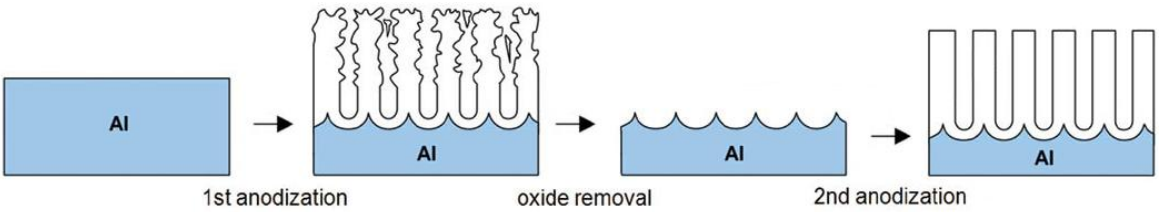

Figure 2.4. Cartoon depicting the double anodization process. Adapted from Lee *et al.*[8]

AAO template samples were coated with a thin coat of carbon from carbon coater (Kinney Vacuum division, Model KDTG-3P, New York Air Brake Co., equipped with a diffusion pump) before imaging. Carbon coating is done to avoid extensive charging

when scanning electron microscope (SEM) images were taken with a JEOL JSM-6500F equipped with an energy dispersive X-ray spectroscopy (EDS) detector from Thermo Electron. Images were taken at 15 kV.

2.3. Results

2.3.1. Analysis of Commercial AAO Templates and the Electrodeposition of Cu_2Sb Nanowires.

Electrodeposition has many advantages including the ability to deposit onto a wide range of surfaces and into many different types of templates. The process of making AAO templates is time consuming. For the initial studies on the electrodeposition of Cu_2Sb wires the templates were purchased from commercially available sources. These templates are not of the finest quality because they contain manufacturing defects, machining marks, and are not well ordered, but they still serve the purpose of initially electrodepositing material into the pores. The empty pores are shown in Figure 2.5A and B. The commercially available templates were used with the goal to deposit Cu_2Sb into the pores and then dissolve away the template leaving only the free standing Cu_2Sb nanowires. Once a good procedure is found to electrodeposit Cu_2Sb into the Whatman filters, then we can make better templates that have more control over size, orientation, and defects for higher quality nanowires of different sizes. The different diameter wires can be studied to find any correlation between size and properties of the wires.

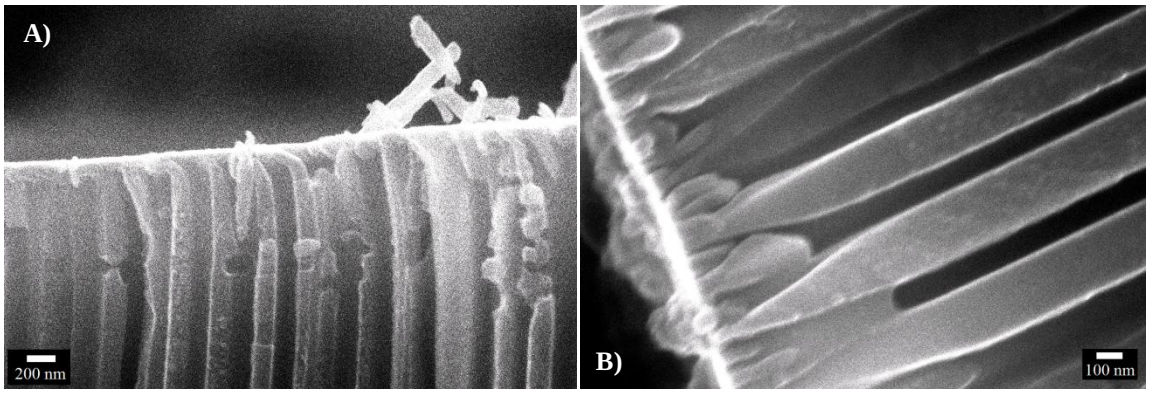

Figure 2.5. SEM images of commercial AAO templates (Whatman Anodisc membrane filters) A) 200 nm diameter pore size. B) 20 nm diameter pore size. No matter the filter diameter, the majority of pores have diameters of 200 nm, due to the commercial manufacturing process.

It is interesting to note that no matter what filter size purchased, the majority of the pores have diameters of 200 nm. The process the manufacturer uses to produce the alumina templates, whether they are the 200, 100, or 20 nm size, is to anodize at a constant voltage and then, towards the end of the process, step down the voltage quickly. Since the anodization voltage influences the rate of oxidation and the rate of expansion, the pore diameter changes with the drop in anodization voltage to around 100 nm. Then the voltage is further dropped to obtain the final 20 nm pore size. To produce the different pore sizes the manufacturer physically removes the part of the filter that is too small. For example, the 200 nm pores are made by just grinding off the 20 and 100 nm portion of the filter. The 200 nm pore diameter is shown in Figure 2.5A and it is apparent where the grinding has occurred from the rough curled top of the template. Furthermore, Figure 2.5B shows the gradual step down of the pore size from the 200 nm to the 20 nm. The importance of understanding this manufacturing process was realized when electrodepositing into the templates.

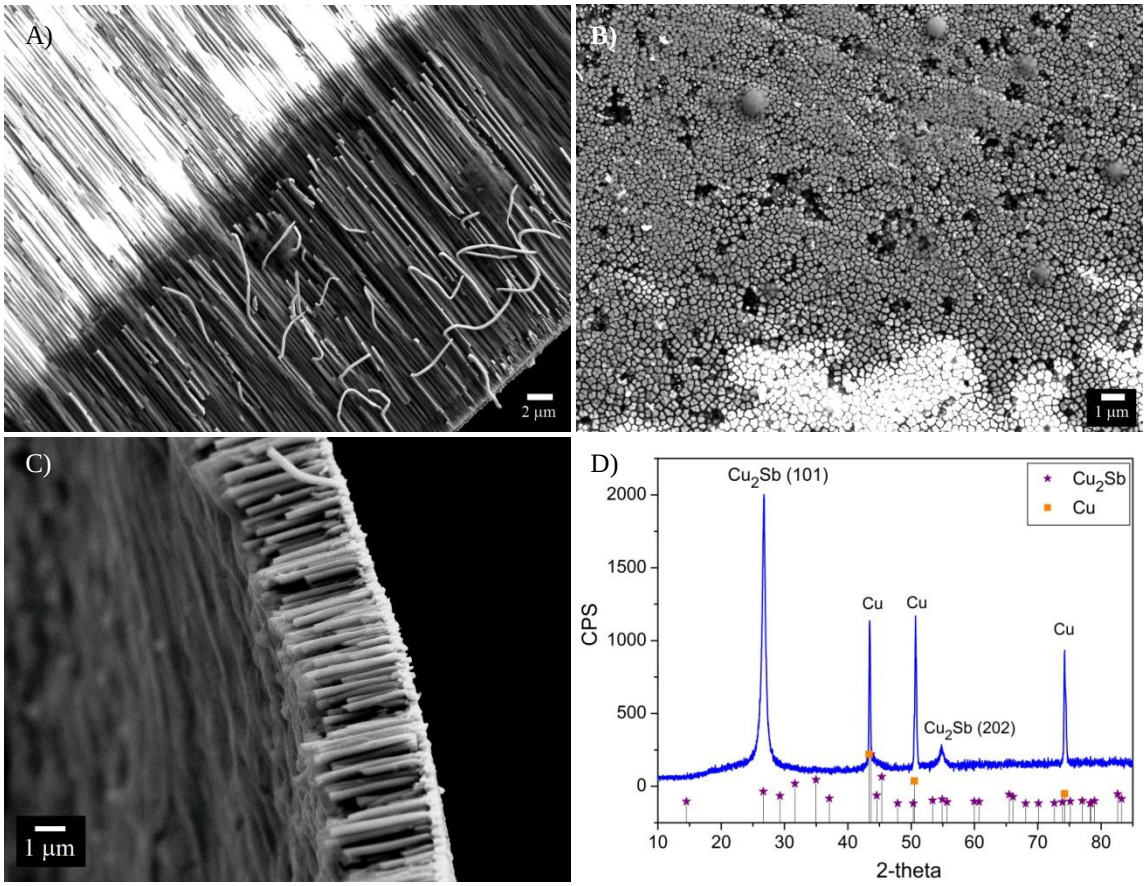

Figure 2.6. SEM images of Cu_2Sb nanowires at different views in AAO template with corresponding XRD powder pattern for Cu_2Sb wires deposited. A) Side view alumina template still present. B) backside with gold polished off back. C) Cross-sectional SEM image of Cu_2Sb nanowires electrodeposited in an AAO template. The AAO template was chemically removed. D) X-ray powder pattern of crystalline Cu_2Sb wires. Cu_2Sb is ordered in the [101] direction. Copper peaks are from placing the template on top of a copper substrate. The Cu_2Sb wires deposited at -1.05 V versus SSCE in 0.025 m Sb_2O_3, 0.075 m $Cu(NO_3)_2 \cdot 3H_2O$ and 0.4 m citric acid brought to pH 6.0 with KOH.

For the electrodeposition of material into nanopores it is essential to employ a pulsed electrodeposition technique to achieve uniform filling of the template and wires that are continuous. The pulse deposition technique involves turning on the voltage at the desired deposition potential for a specific amount of time (T_{on}) and then turning off the potential (T_{off}) and measuring the open circuit potential (OCP) so that the concentration profile can equilibrate with the bulk concentration. This technique has the following benefits: uniform wire growth, less composition changes over the length and diameter of the wires, and greater crystallinity. There are many examples in the literature

where pulse deposition improved the properties of materials.[15, 24, 26] In addition to the pulse technique, the length of T_{on} and T_{off} affects the morphology and density of films and wires. Ibl *et al.* showed that short T_{on} produces large grain sizes and long T_{off} decreases grain size.[27] The benefits and the mathematics of the electrochemistry of pulse deposition is described in greater detail in the dissertation by James M. Mosby.[28]

As mentioned in Chapter 1 it is important not to stir the solution during the electrodeposition of Cu_2Sb or copper rich products form. During the pulsed electrodeposition into templates the solution is stirred since the bottom of the pore does not experience the effects of the stirring, due to the length and diameter of the pores. More importantly, the pulse length in the Cu_2Sb electrodeposition will determine what product forms. It was found through transmission electron microscopy (TEM) studies that longer pulses were necessary to obtain the Cu_2Sb product.[29] Using the correct pulse length of T_{on} = 2.0 seconds the product Cu_2Sb is obtained. The uniform filling can be seen in Figure 2.6A where the cross-section of alumina template shows that the wires fill to about half the depth of the alumina pores. Figure 2.6B is the back side of the template, where the gold has been mechanically polished off, showing how the pores have filled the template uniformly. It appears that approximately 90% of the pores are filled. Figure 2.6C shows the Cu_2Sb wires still attached to the gold backing and the alumina template removed (T_{on} = 2.0 sec , T_{off} = 2.0 sec, total deposition time = 20 min). The corresponding powder pattern of the crystalline Cu_2Sb nanowires is shown in Figure 2.5D. The copper peaks in the XRD powder pattern are from placing the template on a copper substrate. It is very interesting that the crystal pattern is ordered in a different plane then deposited in the bulk. The wires orient in the (101) plane rather than the (001)

plane common during the electrodeposition onto polished substrates. The reason for the change in ordering may be due to the matching of the Cu_2Sb crystal lattice to the lattice of the Al_2O_3 template. This change in the ordering of the crystal compared to the planar deposition may affect the properties of the Cu_2Sb as an anode material since the lithium ions cause expansion of the crystal lattice upon intercalation.

2.3.2. Fabrication of Custom AAO Templates.

After the using the commercial templates to make wires it was time to move onto making custom templates with smaller diameter wires. The method to make the templates was taken from the dissertation by Amy L Prieto.[13] The double anodization technique is important to order the pores. After the first anodization, the oxide layer is removed. The aluminum that is left has indentations in the metal that are in an ordered hexagonal pattern. This is important because these indentations are where the second anodization of the aluminum takes place and a well ordered oxide layer is formed. The growth rate of the AAO template, (at the anodization voltage of 30 V in the 2 °C, 0.444 M oxalic acid solution), is approximately 1.8 μm/hour. This growth rate is considerably slower than the electrodeposition of Cu_2Sb on polished copper described in Chapter 1, where the thickness of a 10 minute deposition was 3.0 μm. A representative sample of an AAO template is shown in Figure 2.7A. The inset is the side view of the template with the barrier layer broken through (more on this in section 2.3.3. below). Figure 2.7B is using the same anodization process, but without the long mechanical and electrochemical polishing steps, which has precedence in the literature.[30] Both show pore diameter between 30 and 40 nm, after carbon coating for imaging with SEM.

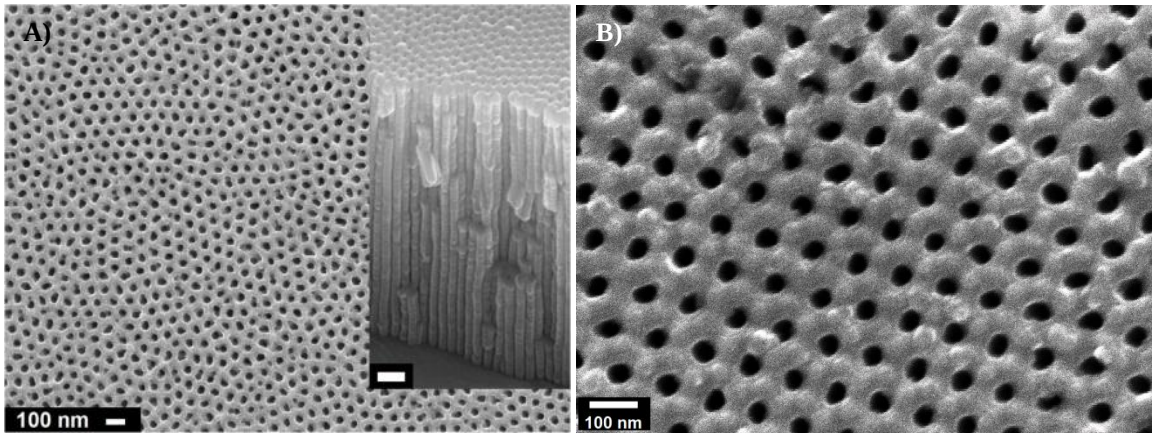

Figure 2.7. SEM images of double anodization of alumina at 30 V in 0.444 M oxalic acid with and without polishing. A) Top view showing ordered structure. Inset is side view of template; scale bar = 200 nm. Mechanically and electrochemically polished prior to anodization. B) No polishing step prior to anodization shows same ordering.[30] AAO templates made through the double anodization technique. Anodized at 30 V in 0.444 M oxalic acid at 2 °C. Growth rate is 1.8 μm/hour.

2.3.3. Barrier Layer Breakthrough.

There are many different methods, in the literature, that describe how to break through the barrier layer of the alumina to electrodeposit straight onto the conducting aluminum.[6, 16-25] However, many of the papers that *have* shown the removal of the barrier layer, still apply extreme overpotentials than necessary to electrodeposit the metal. For instance: nickel is electrodeposited at -3 V[16] , nickel and cobalt are electrodeposited at -5 V and -3 V respectively[23] , and silver is electrodeposited at about -2.5 V, which the authors admitted was significantly larger than the breakdown potential of the remaining barrier layer.[31] Huang *et al.* was even able to deposit TiO_2 nanowires in AAO templates without completely removing barrier layer by implementing a pulsed current technique.[32] Based on these results in the literature, we may have to increase the potential in order to electrodeposit into the pore after removing the barrier layer. This would be difficult with Cu_2Sb since the potential determines the ratio of Cu:Sb. With this in mind, we could electrodeposit copper metal first followed by a separate deposition of Cu_2Sb once a

uniform layer of copper is deposited. Another option is to implement a chronopotentiometric or AC voltammetry technique.

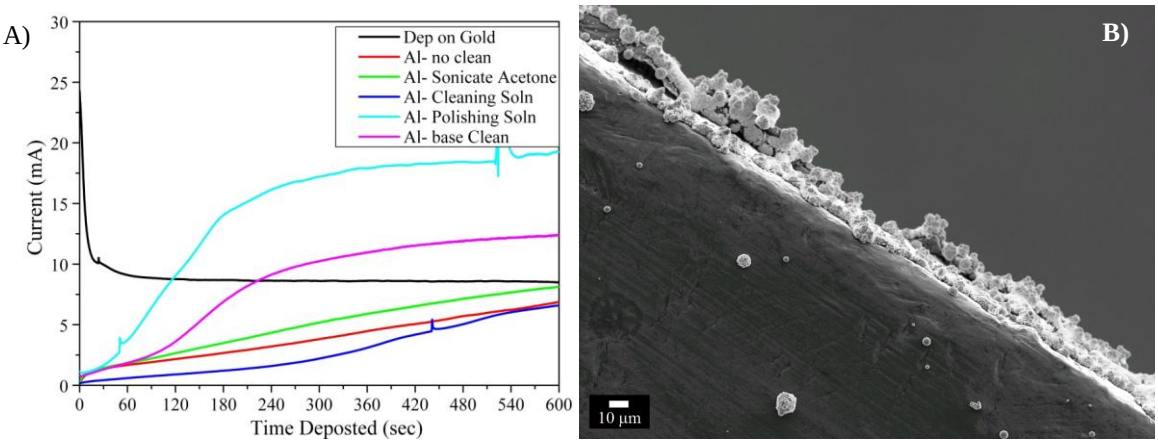

Figure 2.8. Electrodeposition of copper onto an aluminum substrate A) Current transients of a deposition in 0.1 M $CuSO_4$ with 1% H_2SO_4 at -0.3 V on bare aluminum cleaned in different ways. B) Low magnification of surface of aluminum near edge. The electric field is strongest at the edge so a small amount of material was deposited.

To determine how difficult it would be to deposit on aluminum metal, copper was electrodeposited directly onto aluminum. Aluminum has a thin layer of native oxide that forms quite readily and quickly in air, between 2-3 nm thick.[33] Different cleaning steps were performed and the current profiles were monitored. The deposition potential was chosen based off of the CV of the copper sulfate solution (see Appendix 2.1 for CV). Figure 2.8A shows current transients for a deposition in the 0.1 M $CuSO_4$ with 1% H_2SO_4 at -0.3 V after different cleaning steps. None of the cleaning steps used to clean off the aluminum were able to electrodeposit uniform films of copper. Unfortunately, these current profiles look completely different from the deposition on gold, which uniform films of copper were easily electrodeposited. There is no immediate increase in current at the start to establish the double layer, which means that the electrons were not able to reach the solution as easily as with the gold, so the current increases much more slowly with the aluminum substrate. Even after cleaning with different steps, the aluminum

oxidized quickly. This oxide is an excellent electrical insulator and does not allow the electrons to penetrate to the solution at the same voltages when compared to a metal that does not have this oxide present. Figure 2.8B shows how the electric field is much stronger at the edges of the aluminum, so more material is deposited there than on the surface. Keeping the fast surface oxidation of aluminum in mind for future experiments, it will be important to keep the solution degassed or air free in order to slow the re-oxidation of the aluminum after the barrier layer is removed, before copper can be electrodeposited. As a note: the addition of fluoride ion dissolves the native oxide layer, which allows much more copper to be electrodeposited on aluminum. Copper can be seen electrodeposited on the surface of the aluminum in Appendix 2.2, but unfortunately this was completed using a piece of aluminum that had a 2 μm AAO template formed on the surface, which dissolved in a matter of minutes in the presence of acid solutions containing fluoride.

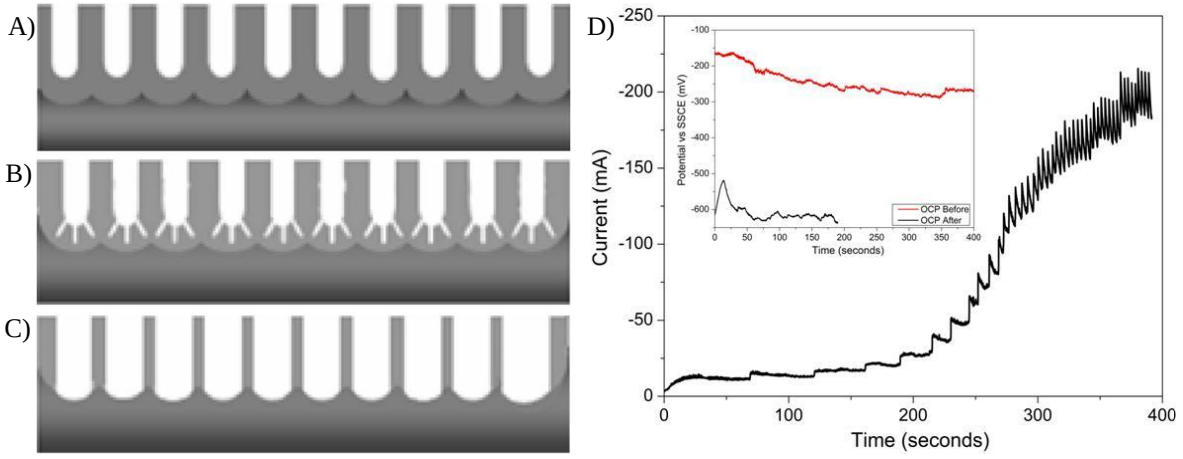

Figure 2.9. Cartoon depicting the barrier layer breakthrough process and corresponding current transient of breakthrough process. (A) after anodization (B) voltage drop forms small branched structures (C) after cathodic polarization in neutral KCl solution.[18] (D) Current transient from a representative barrier layer breakthrough trial. Inset is the OCP before and after barrier layer breakthrough. AAO template made through the double anodization technique. Anodized at 30 V in 0.444 M oxalic acid at 2 °C.

With so many choices for barrier layer breakthrough we were limited with our capabilities of instrumentation. One of the best ways to monitor the barrier layer

breakthrough and thinning process is by monitoring the current. Many different experiments were done to break through the barrier layer following literature methods.[16-22] The best method used was that done by Zhao *et al.*[18] The double anodization was completed the same way as free standing templates (a 30 V anodization in 0.444 M oxalic acid at 2 °C). While the electrode was still in the anodization solution at 30 V the voltage was decreased to 15 V at a rate of 1 V per 9 seconds followed by holding the voltage at 15 V for 15 minutes. By decreasing the voltage, the barrier layer is thinned, since the barrier layer is proportional to the applied voltage (about 1 nm per V).[34] Following this step, the electrode is immediately placed in neutral 0.5 M KCl (Fisher, ACS grade) at an applied potential of -5 V where the current is monitored with the potentiostat. Once the current rapidly increases due to hydrogen evolution, it means that the dissolution of the barrier layer is complete and less of an overpotential is needed to induce the hydrogen evolution.[18] A cartoon depicting this process is shown in Figure 2.9A-C (adapted from reference[18]). The current transient of a representative barrier layer breakthrough is shown in Figure 2.9D. The inset in Figure 2.9D is the open circuit potentials before and after the barrier layer breakthrough. The change in OCP indicates the surface in contact with the solution is no longer oxide and contains significant amounts of bare aluminum. A problem with the barrier layer breakthrough by Zhao *et al.* is the cathodic polarization does widen the pores and is more significant with thicker templates. Because of this pore widening, this process was limited to a template thickness of less than 10 μm.

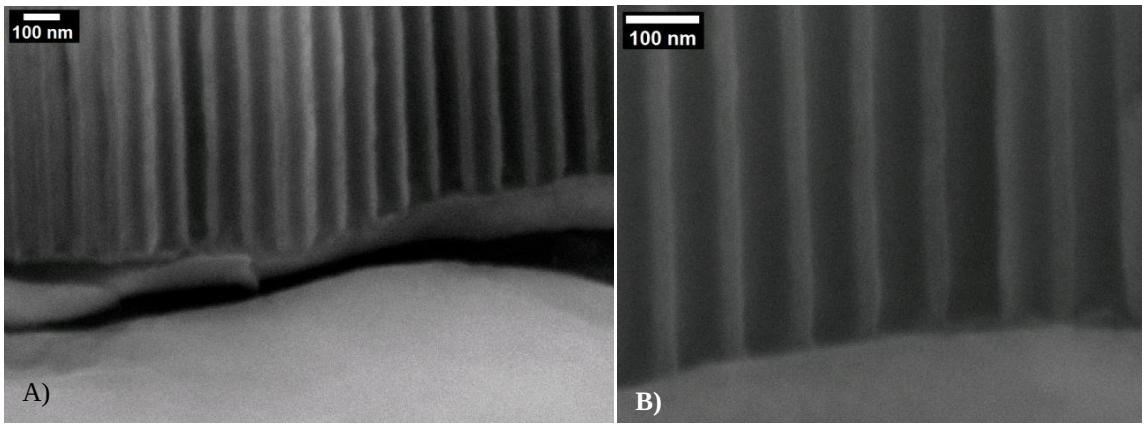

Figure 2.10. Side view of AAO template showing barrier layer breakthrough using method by Zhao *et al.* [18] SEM images of AAO template (A) wide angle view of cross-section showing barrier layer partially broken through and fully broken though. (B) High magnification of area that is completely broken through. AAO templates made through the double anodization technique. Template anodized at 30 V in 0.444 M oxalic acid at 2 °C.

As shown previously in Figure 2.7A inset, the barrier layer is gone at the bottom of the image. A higher magnification of an area of a film where the barrier layer is gone is shown in Figure 2.10A and further magnified in Figure 2.10B. Even though the barrier layer is broken through in this one area shown in Figure 2.10B, it is not an indication of the entire surface of the AAO template. Furthermore, once a small area of the barrier layer is broken through, there is a lower potential barrier for electrons to reach the solution at this point. Electrons will cross to the solution at this local area due to the lower energy barrier, and the current density is highest locally at this point, which will lead to spotty barrier layer breakthrough and subsequent electrodeposition of copper. An example of this is shown in Figure 2.11A, where there are spots of copper, but not a smooth deposition. At higher magnification in Figure 2.11B there are holes in the template, as well as craters where it looks like the copper spots are originating from.

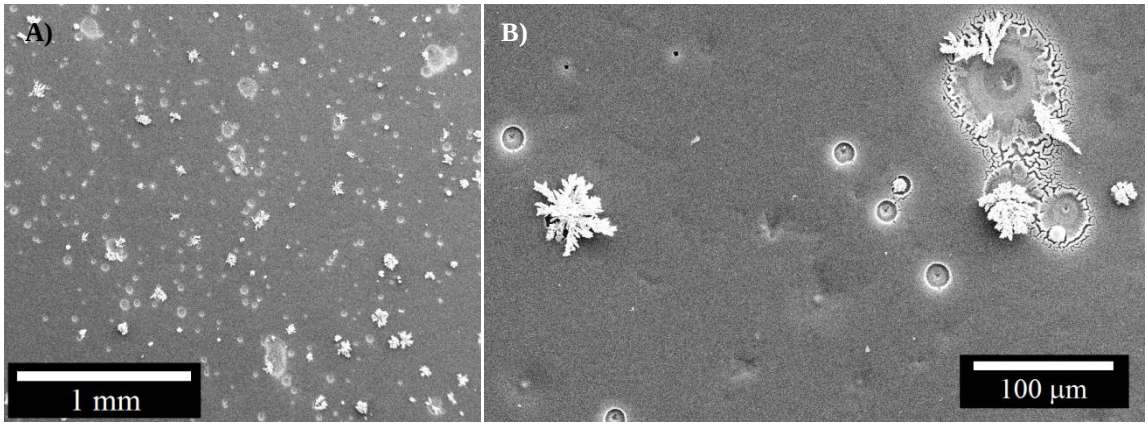

Figure 2.11. SEM image of copper deposited after barrier layer breakthrough using method adapted from Zhao *et al.*[18] and subsequent electrodeposition of copper in 0.1 M $CuSO_4$ with 1% H_2SO_4 at -0.3 V showing only local deposition of copper in specific areas of template. A) Wide angle low magnification image of surface. B) Higher magnification that shows multiple deformities in the film including: holes, craters, and electrodeposited copper dendrites. AAO templates made through the double anodization technique. Anodized at 30 V in 0.444 M oxalic acid at 2 °C.

To help reduce spotty electrodeposition of copper it is important that all of the areas of the template have the barrier layer punched through. In order to check this, it is important to look at a much wider view of the surface to see how many pores are open. The templates were immersed in a saturated solution of $HgCl_2$ (EM Science, ACS grade) to remove the aluminum in order to look at the backside of the template. CAUTION! SOLUTIONS OF MURCURY ARE TOXIX AND SHOULD BE HANDLED WITH CARE! An SEM image of the back side of a template broken through with the method reported by Zhao *et al.* is shown in Figure 2.12. Note how only certain areas of the template are broken through, and the places that are broken through are localized to specific areas of the template.

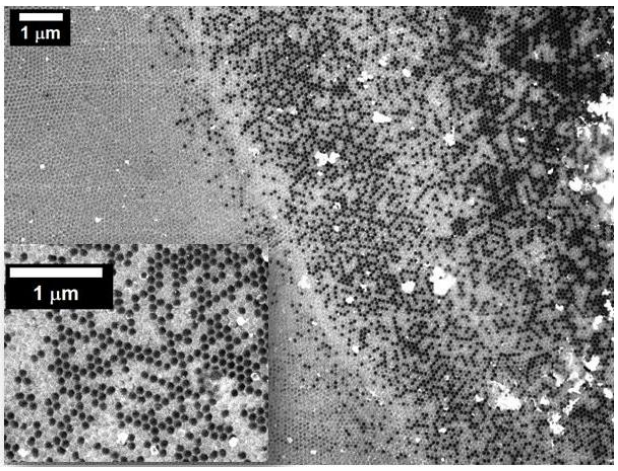

Figure 2.12. Back side of barrier layer from method by Zhao *et al.* showing open pores where the barrier layer was broken through only in selected areas. Inset is magnification of area broken through. AAO templates made through the double anodization technique. Anodized at 30 V in 0.444 M oxalic acid at 2 °C.

2.4. Conclusion

Cu_2Sb was successfully electrodeposited into commercial alumina filters using a pulse electrodeposition technique. It was shown that the diameter listed on the template does not dictate the diameter of the actual wires deposited, due to the manufactures' progressive reduction in pore size used to make all diameter filters. The Cu_2Sb wires were ordered in a different direction compared to the electrodeposition on planar substrates ([101] versus [001] direction), likely due to a better match on the Al_2O_3 template walls. A two step anodization process was shown to produce self-ordered AAO templates with pore sizes between 30 and 40 nm and growth rate of 1.8 μm per hour. It was shown that the mechanical and electrochemical polishing steps are not necessary to obtain the self-ordered templates using a double anodization process.

Promising results have been gathered with multiple methods to break through the barrier layer of these alumina templates. The technique that has shown the best results is the method used by Zhao *et al.*[18] Although, the template is widened by the process and becomes more significant with thicker templates. Even when the barrier layer is removed

a native oxide is formed in a few seconds on the surface of the alumina, which blocks the electrodeposition of copper. Other deposition techniques could be explored to deposit copper, even if a small oxide layer is present, such as: AC voltammetry or a chronopotentiometry technique. Because the backside of the template indicated that the breakthrough was only in localized spots a better barrier layer breakthrough technique should be investigated that has better control over the current during the drop down process. New instrumentation is needed to complete this step.

2.5. References

1. Al mawlawi, D.; Coombs, N.; Moskovits, M., Magnetic-Properties of Fe Deposited into Anodic Aluminum-Oxide Pores as a Function of Particle-Size. *Journal of Applied Physics* **1991,** *70* (8), 4421-4425.

2. Furneaux, R. C.; Rigby, W. R.; Davidson, A. P., The Formation of Controlled-Porosity Membranes from Anodically Oxidized Aluminum. *Nature* **1989,** *337* (6203), 147-149.

3. Li, A. P.; Muller, F.; Birner, A.; Nielsch, K.; Gosele, U., Hexagonal pore arrays with a 50-420 nm interpore distance formed by self-organization in anodic alumina. *Journal of Applied Physics* **1998,** *84* (11), 6023-6026.

4. Jessensky, O.; Muller, F.; Gosele, U., Self-organized formation of hexagonal pore arrays in anodic alumina. *Appl. Phys. Lett.* **1998,** *72* (10), 1173-1175.

5. Shang, H. M.; Cao, G., Template-Based Synthesis of Nanorod or Nanowire Arrays. In *Springer Handbook of Nanotechnology*, 2nd ed.; Bhushan, B., Ed. Springer: New York, 2007; pp 161-178.

6. Tian, M.; Xu, S.; Wang, J.; Kumar, N.; Wertz, E.; Li, Q.; Campbell, P. M.; Chan, M. H. W.; Mallouk, T. E., Penetrating the Oxide Barrier in Situ and Separating Freestanding Porous Anodic Alumina Films in One Step. *Nano Letters* **2005,** *5* (4), 697-703.

7. Hassan, P. N. A. Influence of $H_2C_2O_4$ solution on formation of Porous AAO thin film. http://hdl.handle.net/123456789/3309.

8. Lee, W., The Anodization of Aluminum for Nanotechnology Applications. *Jom* **2010,** *62* (6), 57-63.

9. O'Sullivan, J. P.; Wood, G. C., The Morphology and Mechanism of Formation of Porous Anodic Films on Aluminium. *Proceedings of the Royal Society of London. Series A, Mathematical and Physical Sciences* **1970,** *317* (1531), 511-543.

10. Houser, J. E.; Hebert, K. R., The role of viscous flow of oxide in the growth of self-ordered porous anodic alumina films. *Nat Mater* **2009,** *8* (5), 415-420.

11. Siejka, J.; Ortega, C., An O^{18} Study of Field-Assisted Pore Formation in Compact Anodic Oxide Films on Aluminum. *Journal of the Electrochemical Society* **1977,** *124* (6), 883-891.

12. Houser, J. E.; Hebert, K. R., Stress-driven transport in ordered porous anodic films. *Phys. Status Solidi A-Appl. Mat.* **2008,** *205* (10), 2396-2399.

13. Prieto, A. L. Electrodeposition of Nanostructured Thermoelectric Materials. University of California, Berkeley, 2001.

14. Gao, L. M.; Wang, P. P.; Wu, X. Q.; Yang, S.; Song, X. P., A new method detaching porous anodic alumina films from aluminum substrates. *J. Electroceram.* **2008,** *21* (1-4), 791-794.

15. Zhang, Y.; Li, G. H.; Wu, Y. C.; Zhang, B.; Song, W. H.; Zhang, L., Antimony nanowire arrays fabricated by pulsed electrodeposition in anodic alumina membranes. *Advanced Materials* **2002,** *14* (17), 1227-+.

16. Montero-Moreno, J. M.; Belenguer, M.; Sarret, M.; Müller, C. M., Production of alumina templates suitable for electrodeposition of nanostructures using stepped techniques. *Electrochimica Acta* **2009,** *54* (9), 2529-2535.

17. Stefan, M.-T.; Mária, M.-T., Vertically Aligned Nanowires on Flexible Silicone using a Supported Alumina Template prepared by Pulsed Anodization. *Advanced Materials* **2009,** *21* (40), 4005-4010.

18. Zhao, X.; Seo, S.-K.; Lee, U.-J.; Lee, K.-H., Controlled Electrochemical Dissolution of Anodic Aluminum Oxide for Preparation of Open-Through Pore Structures. *Journal of The Electrochemical Society* **2007,** *154* (10), C553-C557.

19. Zhu, R.; Zhang, H. G.; Chen, Z.; Kryukov, S.; DeLong, L., Horizontally aligned single array of Co nanowires fabricated in one-dimensional nanopore array template. *Electrochem. Solid State Lett.* **2008,** *11* (6), K57-K60.

20. Zhang, J. P.; Kielbasa, J. E.; Carroll, D. L., Nanostructure of the nanopores in anodic aluminum oxide films used as template to fabricate Ag nanowires. *J. Mater. Res.* **2009,** *24* (5), 1735-1740.

21. Shaban, M.; Hamdy, H.; Shahin, F.; Park, J.; Ryu, S. W., Uniform and Reproducible Barrier Layer Removal of Porous Anodic Alumina Membrane. *J. Nanosci. Nanotechnol.* **2010,** *10* (5), 3380-3384.

22. Xu, G. R.; Ren, F. L.; Si, S. H.; Yi, Q. F., Study on removal of the barrier between al substrate and porous anodic alumina by electrochemical approach. *Acta Phys.-Chim. Sin.* **2006,** *22* (3), 341-344.

23. Santos, A.; Vojkuvka, L.; Pallares, J.; Ferre-Borrull, J.; Marsal, L. F., Cobalt and Nickel Nanopillars on Aluminium Substrates by Direct Current Electrodeposition Process. *Nanoscale Res. Lett.* **2009,** *4* (9), 1021-1028.

24. Nielsch, K.; Muller, F.; Li, A. P.; Gosele, U., Uniform nickel deposition into ordered alumina pores by pulsed electrodeposition. *Advanced Materials* **2000,** *12* (8), 582-586.

25. Santos, A.; Vojkuvka, L.; Pallarés, J.; Ferré-Borrull, J.; Marsal, L. F., In situ electrochemical dissolution of the oxide barrier layer of porous anodic alumina fabricated by hard anodization. *Journal of Electroanalytical Chemistry* **2009,** *632* (1-2), 139-142.

26. Trahey, L.; Becker, C. R.; Stacy, A. M., Electrodeposited Bismuth Telluride Nanowire Arrays with Uniform Growth Fronts. *Nano Lett.* **2007**.

27. Ibl, N.; Puippe, J. C.; Angerer, H., Electrocrystallization in Pulse Electrolysis. *Surface Technology* **1978,** *6* (4), 287-300.

28. Mosby, J. M. Colorado State University, Fort Collins, 2010.

29. Mosby, J. M.; Johnson, D. C.; Prieto, A. L., Evidence of Induced Underpotential Deposition of Crystalline Copper Antimonide via Instantaneous Nucleation. *Journal of the Electrochemical Society* **2010,** *157* (6), E99-E105.

30. Zhao, Y. C.; Chen, M.; Zhang, Y. N.; Xu, T.; Liu, W. M., A facile approach to formation of through-hole porous anodic aluminum oxide film. *Mater. Lett.* **2005,** *59* (1), 40-43.

31. Choi, J.; Sauer, G.; Nielsch, K.; Wehrspohn, R. B.; Gosele, U., Hexagonally arranged monodisperse silver nanowires with adjustable diameter and high aspect ratio. *Chem. Mat.* **2003,** *15* (3), 776-779.

32. Liu, S. Q.; Huang, K. L., Straightforward fabrication of highly ordered TiO_2 nanowire arrays in AAM on aluminum substrate. *Sol. Energy Mater. Sol. Cells* **2005,** *85* (1), 125-131.

33. Alwitt, R. S. Electrochemistry Encyclopedia. http://electrochem.cwru.edu/encycl/art-a02-anodizing.htm.

34. Ghaddar, A.; Gieraltowski, J.; Gloaguen, F., Effects of anodization and electrodeposition conditions on the growth of copper and cobalt nanostructures in aluminum oxide films. *Journal of Applied Electrochemistry* **2009,** *39* (5), 719-725.

3. Chapter 3 – Initial Study of the Speciation of Antimony Citrate and Copper Antimony Citrate Solutions Using ESI-MS for the Discovery of New Species in the Solution Used to Electrodeposit Cu_2Sb

3.1. Introduction

Cu_2Sb is a very promising anode material with which to improve the current lithium ion battery technology. This is due to its low volume expansion upon lithium intercalation compared to other anode materials, which leads to less pulverization of the anode after many charge and discharges.[1] It also has a higher lithiation potential so the risk of plating metallic lithium and subsequent safety concerns is significantly reduced.[2] Recently, we presented a method to produce crystalline films of Cu_2Sb in room temperature aqueous solutions, by direct electrodeposition. Complexation of the individual metals with citric acid was necessary in order for the Cu_2Sb to be deposited.[3] Citric acid is a triprotic α-hydroxy carboxylic acid, meaning that three protons can be removed from carboxyl groups to give the anion denoted: Cit^{3-}, while $H_{-1}Cit^{4-}$ will be used to refer to the removal of a fourth proton from the α-hydroxy group.[4-5] The system used to electrodeposit Cu_2Sb is interesting because the deposition occurs if the pH is at 6 and the complexing agent is citric acid, even when the ratio of copper to antimony concentrations are varied from a 0.5:1 to a 2:1 ratio. The degree of crystallinity of the material may change with different reaction conditions, but the peaks of the X-ray diffraction pattern (XRD) of the deposited films consistently match Cu_2Sb. During the electrodeposition, there must be very specific control over the species being deposited from solution, which pushes the equilibrium towards crystalline Cu_2Sb rather than an

alloy. The reaction scheme is postulated to be based on the $[Cu_2Cit_2H_{-1}]^{3-}$ and $[SbCitH_{-1}]^{-}$ species depositing through a co-reduction (Equation 3.1).[3]

$$2[Cu_2Cit_2H_{-1}]^{3-} + 2[SbCitH_{-1}]^{-} + 4H_3O^{+} + 14e^{-} \rightarrow 2Cu_2Sb + 6Cit^{3-} + 4H_2O \qquad \text{Eq. 3.1}$$

This reaction scheme agrees with the energy dispersive x-ray spectroscopy (EDS) and x-ray photoelectron spectroscopy (XPS) data given in the publication, where it is shown that a higher percentage of antimony occurred in films deposited at more negative potentials, while the films contained increased amounts of copper when deposited at more positive potentials.[3] The species considered in the reaction were based on literature results for the individual solutions of copper citrate and antimony citrate. It was hinted that there may be a heterometallic Cu-Sb-citrate species present in the system, but no evidence was presented to confirm this suggestion. Many other complexes may be present in the solution, and these complexes may play an important role in the way Cu_2Sb deposits. In particular, any heterometallic Cu-Sb-citrate species that have yet to be confirmed may be the species contributing to the deposition.

In the literature, there is prevalent evidence that heterometallic citrate species exist in many different types of solutions. A comprehensive review of other heterometallic copper species can be found in the book by Melnik *et al.*[6] More specifically, Daniele *et al.* completed a thorough thermodynamic and spectrophotometric study on previously identified heterometallic Cu-Ni-citrate, Cu-Zn-citrate, and Cu-Cd-citrate species.[7] A follow-up study with speciation diagrams by Rode *et al.* confirmed the presence of the heterometallic Cu-Ni-citrate species.[8] In addition to these, the crystal structure of a Cu-Sb-citrate complex was reported by Smith *et al.* with the composition $[CuSb(HCit)(Cit)(H_2O)_2]\bullet 2.5H_2O$.[9] Rather than looking at a solid structure that has been

crystallized out of solution or analyzing the effects of applying a potential in a cyclic voltammogram (CV), it would be beneficial to be able to directly study the solution and the complexes therein. One way to study the solution chemistry is by using electrospray ionization mass spectrometry (ESI-MS). ESI-MS has emerged as a premiere technique due to its soft ionization. This soft ionization has led to an increased use of ESI-MS in equilibrium studies of metal-ligand complexes (M-L). [10-16] Specifically, the review article by Di Marco *et al.* describes many M-L equilibrium studies where ESI-MS was used for qualitative and quantitative detection of species.[14] Mass spectrometry utilizes the separation of species based on their mass-to-charge ratio. In addition, one can confidently assign peaks in the spectra based on the nominal isotopic ratio.

We investigated the solution chemistry of this Cu_2Sb deposition solution system through ESI-MS by first analyzing citric acid and copper citrate solutions, since their speciation has been well studied and characterized. ESI-MS of these solutions show that the main species in solution qualitatively follow the predicted speciation diagrams. Through studying these simple systems, which have well known solution chemistry, we can be confident that our ESI-MS method is valid for studying the less clearly understood solution chemistry of antimony citrate and copper antimony citrate. Evidence for two new antimony citrate species in solution in addition to the heterometallic species [CuSb(HCit)(Cit)], previously only reported in solids that had been crystallized out of solution, was discovered in solution through ESI-MS. The final goal is to combine the knowledge gained from this solution speciation through ESI-MS with speciation diagrams, titrations, UV-Vis, and cyclic voltammetry in order to understand the single

potential deposition of Cu_2Sb. Two new reaction schemes are presented that are directly related to the complexes in solution responsible for the electrodeposition of Cu_2Sb.

3.2. Experimental

The electrodeposition solution was prepared using units of molality (m) rather than molarity (M), (added a specified amount of solvent before the addition of the solutes). The following were combined and dissolved with the aid of mechanical stirring for 48 hours: doubly deionized 18Ω water (Milli-Q Plus System, 4-bowl, Millipore) 0.025 m antimony (III) oxide (Sb_2O_3 nanopowder, <250 nm particle size (BET), ≥99.9% trace metals basis, Sigma Aldrich) and 0.4 m anhydrous citric acid (denoted H_3Cit, puriss. p.a., 99.5+%, ACS reagent, Sigma Aldrich). After the Sb_2O_3 was dissolved, 0.075 m copper (II) nitrate trihydrate ($Cu(NO_3)_2 \cdot 3H_2O$, purum. p.a., 98.0-103% RT, Sigma Aldrich) was added. Solutions changed from clear to light blue following the addition of Cu. This solution can be stored indefinitely with no noticeable degradation in performance. The pH probe (Thermo Orion 9157 BNMD Orion triode 3-in-1 pH electrode equipped with auto temperature compensation) was calibrated with buffers of pH 1.68 (Orion potassium tetraoxalate dehydrate buffer), 4.00 (Fisher potassium biphthalate buffer), 7.00 (potassium phosphate monobasic-sodium hydroxide buffer), and 10.00 (potassium carbonate-potassium borate-potassium hydroxide buffer) using a Thermo Orion 3 star series pH meter. The solution was brought to pH 6.0 with saturated KOH, at which time the solution became much darker blue.

Solutions used for mass spectrometer measurements were prepared using the same reagents as in the deposition solution, however, they were brought to pH with 2 M NH_4OH (Mallinckrodt ACS grade) and must be diluted in order to avoid clogging the

instrument. Since, the ESI-MS solutions are more dilute than the deposition solution and are brought to the desired pH with ammonia rather than potassium hydroxide, a deposition was done in this solution to make sure these changes did not affect the deposition of Cu_2Sb. The XRD pattern matched the standard (PDF 85-0492) of Cu_2Sb in each case. Powder X-ray Diffraction (XRD) data was collected using Cu Kα radiation from a Scintag X-2 Advanced Diffraction X-Ray cabinet system, equipped with a Peltier detector.

ESI-MS experiments were completed on a Finnigan LCQ Duo Mass Spectrometer with standard components. The analytes were injected using a syringe pump with a flow rate of 25 µL/min through a fused silica 100 µm inner diameter capillary. The ion source was electrospray ionization with an off axis ESI probe. Spray voltage was set at 4.5 kV. Capillary temperature was set to 140 °C except for the temperature modification experiment. Sheath gas was nitrogen with a flow rate of 19 arbitrary units. The mass analyzer was an ion trap and detection was accomplished via an electron multiplier tube. All spectra were collected in both positive and negative ion mode and were compiled from an average of 50 individual scans.

Titrations were done using an auto titration setup equipped with a drop counter using LabVIEW version 7.1. The controller was a National Instruments box made up of two modules of Model FP-TB-1. One of these modules controlled the drop counter and the other controlled the pH probe (same as above). Communication was accomplished through a laptop computer connected to the box through Ethernet port (model FP-2000). The pH probe was calibrated with a two point calibration using pH 4 (same as above) and pH 10 (same as above). This auto-titrator setup was used to obtain a qualitative picture

of the titration curve. UV-Vis measurements were completed on an Agilent 8543 UV-Visible spectrophotometer equipped with UV-Vis ChemStation software. Quartz cuvettes were used with 1.0 cm path length. Blank spectra were completed with Millipore water.

Cyclic Voltammograms (CVs) and depositions were performed on a CH Instruments Model 660C Potentiostat/Galvanostat or 1232A Potentiostat. CVs were taken in a three electrode set up consisting of the following electrodes: (1) a saturated sodium calomel electrode (SSCE) reference electrode (+0.236 V versus standard hydrogen electrode), (2) a platinum disk electrode (2.01 mm^2) working electrode (WE), and (3) platinum wire (diameter 0.5 mm, Aldrich, 99.9% trace metals basis) counter electrode. CVs were consistently started near the open circuit potential of -0.3V and scanned in the positive direction up to the maximum +1.2V, followed by a scan in the negative direction to a minimum of -1.6 V and returning to +1.2V.

3.3. Results

3.3.1. Processing ESI-MS Data and Optimization of Parameters

Electrospray ionization mass spectrometry (ESI-MS) is a technique that has powerful capabilities for the analysis of species in solution. However, as with any technique it has its limitations and special experimental considerations that need to be addressed. The first issue is that only volatile salts can be used in solution. This means that only volatile acids and bases may be used for changing the pH, and it is difficult to use a high ionic strength solution. In our case, dilute solutions that were brought to the desired pH with ammonia had no effect on the electrodeposition of Cu_2Sb. A second, more minor, issue is organic solvents may need to be added to the solution because pure

water may cause discharges within the spray chamber, leading to both signal instability and a decrease in the signal to noise ratio.[14] To understand these issues and the overall process of going from solution to the gas phase it is important to understand the ionization process.

The mechanism by which compounds are ionized in ESI-MS is still a debated subject. There are two proposed possibilities. The first is the Charged Residue Model (CRM), first researched by Dole and co-workers[17] and then explained in more detail by Röllgen.[18] The second proposed mechanism is called the Ion Evaporation Model (IEM), first proposed by Iribarne and Thomson.[19-20] The differences between these mechanisms are in the final stages of the ionization process when the droplets are less than 10 nm in size.[21] Since there is no distinction between the two mechanisms until these final stages, the following discussion will not discriminate between the two mechanisms.

Figure 3.1 shows a schematic of the electrospray mechanism as a special kind of electrolytic cell.[22-23] An electric field is applied between the tip of a capillary and a large plate. Depending on the configuration of the instrument, the plate might have a hole in it that leads directly into the mass spectrometer, or it could be off axis in some way. As an example of the ionization process, consider an ESI-MS in positive ion mode (when positively charged ions are collected in the spectrometer). There are both positive and negative ions in the solution. When a negative potential is applied to the counter electrode plate, positive ions will migrate towards the negative electrode and begin pushing on the meniscus of the liquid. If the applied field is sufficiently high, the force exerted by the positive ions on the meniscus of the liquid will lead to the formation of a liquid cone as the surface tension of the liquid holds back the ions. This cone is called a

Taylor cone. Eventually, the force from the ions on the liquid will overcome the force of the surface tension and a fine jet of droplets will break away from the cone. The solvent in the droplets evaporates and free ions are formed.

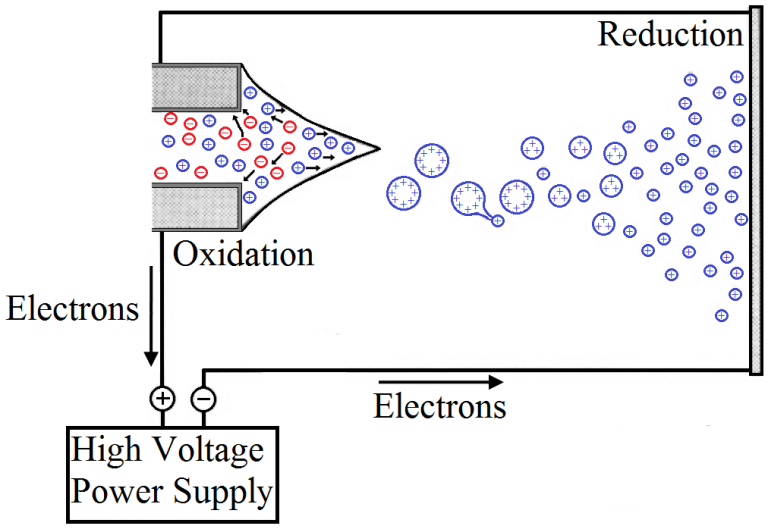

Figure 3.1. Cartoon showing the electrospray process inside ESI-MS as a special kind of electrolytic cell. In positive ion mode the capillary is positively charged so positive ions in solution migrate away from the capillary to the plate leading to the mass spectrometer; reproduced from Blades *et al.*[22-23]

For the ions to form, the applied electric field must be sufficiently high. However, if the voltage is too high, the Taylor cone will move into a multi jet mode and may cause unneeded fragmentation that does not represent actual species present in the solution. If the applied voltage is lower than the onset voltage for a given solvent, electrical discharges could occur (particularly when using water as the solvent, due to its high surface tension). The voltage needs to be set several hundred volts above the onset voltage in order to prevent electrical discharges.[21] In our study, water is the solvent and an onset voltage of at least 4.0 kV is required. The voltage in our experiments was set to 4.5 kV so that electrical discharges were not an issue, and so that the voltage was not high enough to significantly decrease signal strength.

Since ESI-MS uses a soft ionization method, species that are at equilibrium in solution can be extracted into the gas phase. Because of this capability, it is possible to

determine the number of species in solution and the stoichiometry of those species. This determination cannot be duplicated through more traditional techniques such as potentiometry or UV-Vis spectroscopy. However, there are disadvantages to using ESI-MS.

ESI-MS causes perturbation of the solution away from equilibrium during the ionization process, and gas phase reactions can occur during the ionization process, as well.[14, 24] A common example of these gas phase reactions is the formation of adducts with other ions present in the solution, so that multiply-charged species present in solution are detected *only* as singly-charged species by the instrument. Protons are particularly labile and can attach to or detach from a species much faster than the time scale of the ionization.[15] Multiply-charged negative ions often adduct with protons, thus decreasing the negative charge of these species so that the ions detected in ESI-MS are nearly all singly charged.[14] For example deprotonated citrate (Cit^{3-}) would be detected as $[H_2Cit]^-$ or $[H_3Cit{\bullet}H]^+$ due to its formation of adducts with protons. Gas phase reactions are more difficult to elucidate, but changing instrumental parameters can help. Nevertheless, ESI-MS is another tool to probe a given solution to determine what species are present. To obtain actual equilibrium constants, potentiometry and UV-Vis spectra will be obtained. Table 3.1 summarizes the utility of common techniques for studying the speciation of solutions. UV-Vis and potentiometry work well for calculating equilibrium constants, but ESI-MS is clearly the better choice for identifying species and stoichiometry. Though it may be possible to identify species in solution using NMR, ESI-MS provides less convoluted and easier to interpret data.

Table 3.1. Advantages and disadvantages of techniques used to study the speciation of a solution. Table reproduced from Di Marco *et al*.[14]

Technique	Number of Species Recognition	Stoichiometry Recognition	Equilibrium Constants Calculation	Detection
Potentiometry	Not Ideal	Not Ideal	Excellent	10^{-4} M
UV-Vis	Not Ideal	Fair	Good	10^{-5} M
NMR	Fair	Fair	Not Ideal	10^{-3} M
ESI-MS	Good	Excellent	No(?)	10^{-6} M

As mentioned above, side reactions that can occur within the ionization chamber (such as gas phase reactions) cause problems when using ESI-MS for the determination of ions in solution. Two examples of these reactions are: the formation of adduct ions (as mentioned above) and the formation of dimers/clusters:

> Adduct ion - An ion formed by the interaction of two species, usually an ion and a molecule, and often within the ion source, to form an ion containing all the constituent atoms of one species, as well as an additional atom or atoms.[25]
>
> Dimeric Ion - An ion formed either when a chemical species exists in the vapor as a dimer and can be detected as such, or when a molecular ion can attach to a neutral molecule within the ion source to form an ion such as $[M_2]^{+\bullet}$ where M represents the molecule.[25]
>
> Clusters – Will be referred to as more than two multiple chemical species coming together as an ion of interest detected in the MS.

The presence of these ions makes fully identifying what species are present in a given solution difficult. For example, no dimeric species of citric acid exist in solution, but a dimer peak of significant abundance appears in negative ion mode ESI-MS. Upon the addition of antimony and copper to the citric acid solution, it becomes increasingly difficult to determine what species are present.

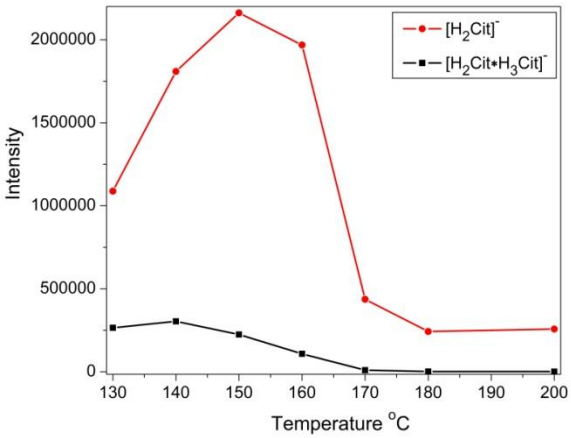

Figure 3.2. Effect of temperature on abundance of $[H_2Cit]^-$ versus the dimer $[H_2Cit{\bullet}H_3Cit]^-$. Intensity of dimer produced in the gas phase decreases linearly with increasing temperature, while increasing intensity of $[H_2Cit]^-$ ion present in solution, until reaching the citric acid decomposition temperature. Solution was 10 mM citric acid at the initial pH of 2.7. Individual points were the extracted average intensity of the ion of interest (191 ± 0.5 and 387 ± 0.5 m/z units).

One way of narrowing down what species are present in solution and what species are present only due to gas phase reactions is to change some of the instrument conditions.[16] Some common ways of performing this are to change the temperature, add collision induced dissociation (CID) by addition of a gas to the system to cause collisions of the molecules, or to add source fragmentation (a voltage stress) called collision energy (CE).[30] All of these techniques add energy to the system to cause ions to break up. Usually, ions that are already formed in solution have higher bond strength than the ions that are formed in the gas phase. In theory, the ions will either break apart or remain intact based on how strongly they are bonded. The ions that decrease the least in abundance as a result of this added energy will be the ions that are already present in the solution. Figure 3.2 is an ESI-MS plot of citric acid and the citric acid dimer in negative ion mode. The solution was run at a constant flow rate and temperature was systematically increased for each set of data points. After a set equilibration time, the scan was completed. As shown below, the dimer concentration decreases linearly with increased temperature while the concentration of the species present in solution (citric

acid) increases to an optimum value and then decreases after reaching its thermal decomposition temperature of 175 °C.[26] This demonstrates the viability of using temperature variation to compare the strength of clusters formed.

As with most instruments, the ESI-MS must be optimized in order to obtain the best data possible. The first step is to optimize the instrument so that the highest number of counts is obtained. Second, the data must be extracted and normalized through a specific set of procedures to obtain data that qualitatively reflects the relative abundances of species in solution. After these adjustments, the data can be confidently examined and used in conjunction with data from the previously mentioned techniques to understand our system.

Tuning the instrument increases counts by going through an automatic procedure that optimizes parameters of the instrument including the capillary voltage and tube lens offset voltage. Automatic gain control (AGC) is a feature that increases the flow of ions into the ion trap chamber to the full ion target value ($5x10^7$) by controlling the time that the injection control "valve" is open (technically called the entrance end cap electrode or "gate lens").[27] The time that the gate lens is open is referred to as the injection time (IT). This IT is important because if there are too few ions, then the detection limits suffer, but if there are too many ions in the trap, they will begin to interact with one another. This interaction is referred to as space charging and is a result of neighboring ions with like charges getting too close to each other and repelling one another, leading to a decrease in resolution and mass accuracy.[27] The capability to control the injection time is important for more quantitative measurements. If the instrument is automatically controlling how many ions are entering the ion trap chamber during each scan, then the

actual number of ions detected goes up and down, which is not representative of the solution. For two different samples at two different pH levels, the number of total ions will be different. If the AGC is turned on, the instrument will try to match the number of ions to the target value. Because of this, the relative abundance of specific species in the two different solutions will be skewed. To alleviate this problem, it is best to initially run the sample with the AGC on. After the instrument optimizes IT, then the AGC can be turned off and the IT can be manually set to the value obtained using the AGC function. Figures 3.3A and B show this effect of the AGC for the binuclear copper dicitrate species. With the AGC on, there is significantly more error in the measurement, but with the AGC off the data matches what is expected from the literature results, where the total abundance of the binuclear copper dicitrate species increase with increased pH.[28] Figure 3.3B will be referred to as a pseudo-speciation plot, since the data is the qualitative abundance of a combination of species versus pH. The data has been normalized using equation 3.2 (discussion below).

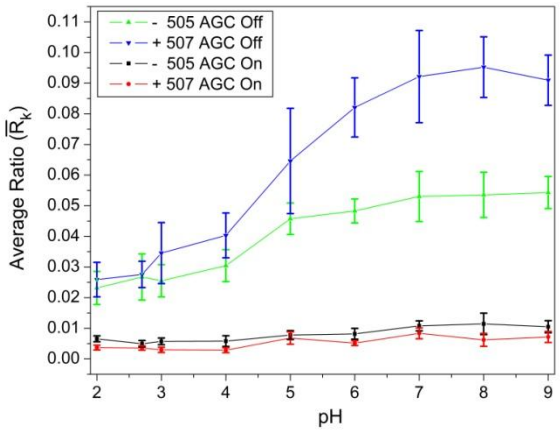

Figure 3.3. Effect of auto gain control (AGC) on the abundance of species versus pH. When AGC is ON abundance is essentially flat across pH. When AGC is off the abundance increases with pH as expected for the binuclear copper dicitrate species based off literature results.[28] Each data point is from the average ($\overline{R}_k$) of 50 ion scans +/- the standard deviation of a 98 µM $Cu(NO_3)_2$ in 500 µM citric acid solution brought to pH with ammonium hydroxide.

Once the instrument is set up properly, including a recent tune method of the instrument and manually controlling the IT, the solutions can be analyzed and the data processed. The following discussion covers how the data is processed from the raw data given by the instrument to the pseudo-speciation plots used in this paper. Each sample is equilibrated in the ESI-MS for two minutes and then 50 scans are completed on the sample. The syringe pump runs at a constant flow rate and the instrument runs one scan (full range of the m/z values) and records the intensity of each m/z, then runs the second scan and records the intensity of each m/z, and so forth all the way through the 50 scans. All this data is recorded in the instrument, including the total ion count (TIC), which is the sum of all the ions present. Each peak in the average spectra is the isotopic sum of all the atoms in the ion from each scan and then averaged together for each scan. The instrument software then fits the data with a smoothing function called 7M boxcar, which is a moving average of the data that makes the curve appear smoother. Ideally, each peak would be a single line, but due to the slight variability in measuring the mass-to-charge ratio, the data will be distributed over a small range. The intensity of the ion of interest is equal to the integration of the entire peak. The software used by the ESI-MS system does not have an integration function, so the data is extracted by selecting the peak max ± 0.5 m/z units. A plot that depicts this graphically is shown in Figure 3.4A. The extraction of the data was kept uniform at ± 0.5 m/z of the peak max for all peaks measured. With ESI-MS data, it has been shown that peak height is also a valid parameter to use for quantifying peaks.[29] For the data in the current study, results did not differ regardless of whether peak height or the peak max ± 0.5 m/z units was used, so the extraction of data using peak max ± 0.5 m/z units was our method of choice.

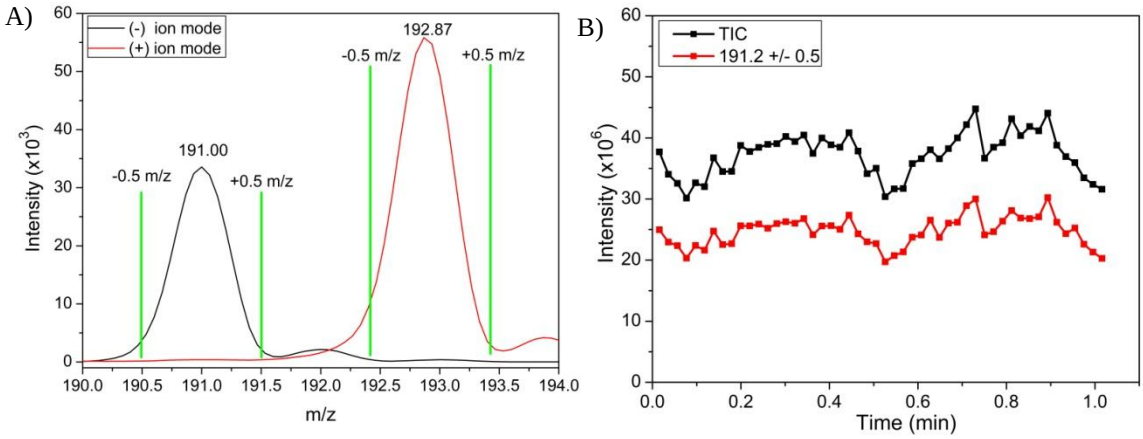

Figure 3.4. ESI-MS spectra showing the procedure for extracting the data from the ESI-MS spectra. A) ESI-MS spectra from the average of 50 ion scans from a 500 µM citric acid solution at initial pH showing peaks of citrate in positive ion mode and negative ion mode. Green lines indicate where the integration was taken. B) Corresponding intensity versus each individual extracted scan (i_k) and total ion count (TIC), which shows the systematic error of the syringe pump.

Figure 3.4B shows a plot of 50 individual scans of the extracted 191.2 ± 0.5 m/z peak and TIC of a citric acid sample in negative ion mode. It is apparent that over the 50 scans the intensity changes. This intensity change is due to the systematic error in ionization that is caused by the pumping action of the syringe pump. To verify that the change in intensity is caused by the syringe pump, an experiment was completed in which the flow rate was varied. The instrument has two flow rate settings: Purge on (25 µL/min) and purge off (5 µL/min). Figure 3.5A is a plot of the intensity of the 191 peak over the course of 1000 scans. The periodic nature of the pumping action is apparent both at fast pump speeds and slow pump speeds. This error is present in plots for both the TIC and for each sample. It is important to remove this variation since it is systematic and has been assigned to a specific cause outside of the system being investigated. By dividing the intensity by the corresponding TIC of each the scan, this systematic error is accounted for and the resulting ratio is a more accurate representation of the data, without this systematic error. This is shown in equation 3.2:

$$\text{Average Ratio } (\overline{R}_k) = \frac{\left(\frac{i_1}{TIC_1}\right)+\left(\frac{i_2}{TIC_2}\right)+\left(\frac{i_3}{TIC_3}\right)+\cdots+\left(\frac{i_{50}}{TIC_{50}}\right)}{50} = \frac{\sum_{k=1}^{50}\left(\frac{i_k}{TIC_k}\right)}{50} \qquad \text{Eq. 3.2}$$

where i_k is the individual ion of interest for a particular scan and TIC_k is the total ion count of the corresponding scan.

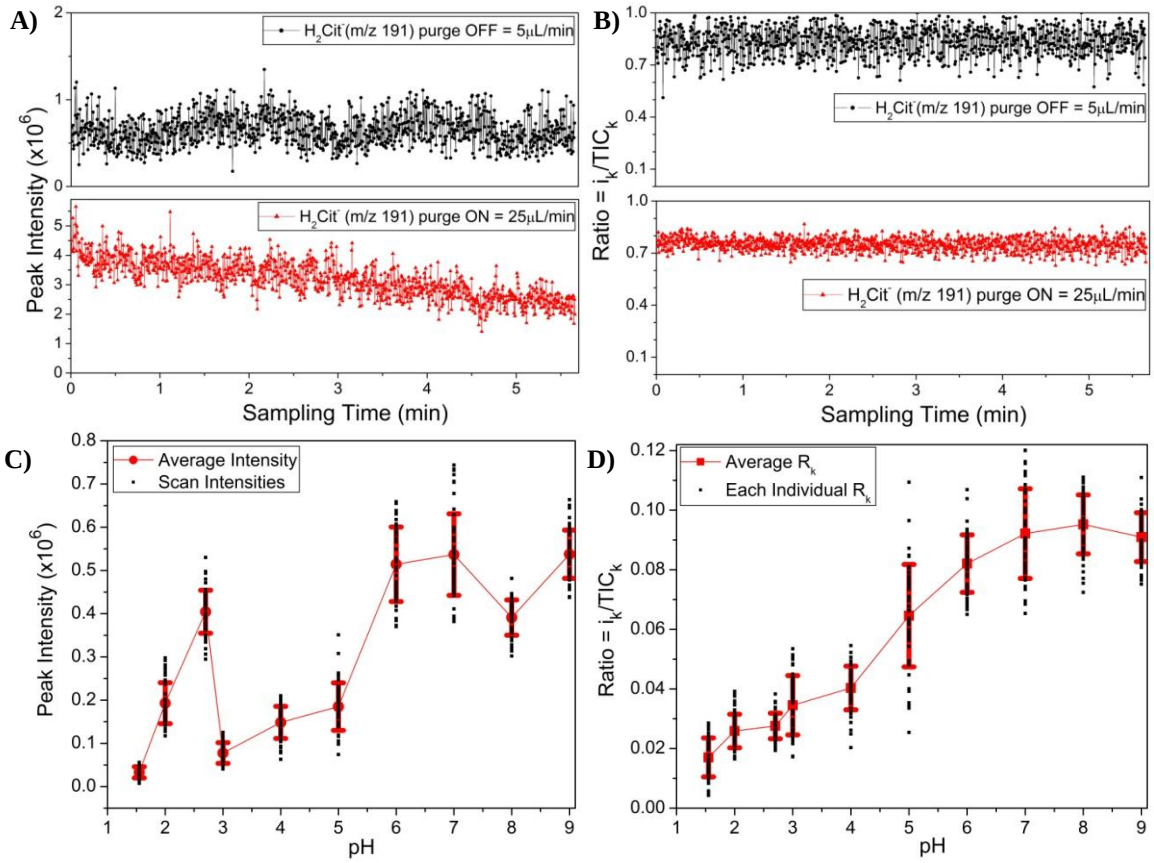

Figure 3.5. Data from ESI-MS abundance plot showing how the data is processed to obtain final $\overline{R}_k$. (A) Effect of intensity with different flow rate, showing the systematic error of the syringe pump. (B) The importance of normalizing the intensity with the total ion count to remove the systematic error of the syringe pump. A) and B done out of a solution of 500 μM citric acid at the initial pH value where 1000 scans were taken. (C) Plot of the intensity versus pH, shows data that is very irregular at different pH values due to the systematic error of the syringe pump. (D) Normalized intensity $\overline{R}_k$ versus pH reduces scatter of data and matches literature results.[28] Each large point in C and D is from the average ($\overline{R}_k$) of 50 ion scans +/- the standard deviation of binuclear copper dicitrate (m/z = 507) from a 98 μM $Cu(NO_3)_2$ in 500 μM citric acid solution brought to pH with ammonium hydroxide.

When the normalization correction is applied the error is significantly reduced, as shown in Figure 3.5B. The decrease in intensity when the purge is on is completely accounted for by normalizing species of interest to the total ion count. A follow up experiment was done, in which the pump was turned on and off every 100 scans for 500

total scans, then the flow was turned off completely, and finally the injection syringe was pushed manually. The data was normalized (as above), and the plot of ratio versus time is flat compared to the intensity versus time plot. This plot can be found in the Appendix 3.1. This normalization procedure was applied to the binuclear copper dicitrate species being run over a pH range of 1.5 to 9, and is shown in Figure 3.5D compared to the non-normalized data in 3.5C. All 50 scans at each pH are plotted for clarity along with the average ($\overline{R}_k$) ± standard deviation (± one sigma (σ)). More information about the binuclear copper dicitrate species can be found in Section 3.3.2.

3.3.2. Qualitative Speciation Studies with Citric Acid and Copper Citrate

We have used ESI-MS to study the species in the citric acid and copper nitrate solutions, since the speciation of this system is well established. After mastering ESI-MS techniques sufficiently on simple systems, they are then applied to the more complex copper-antimony-citrate solution. The ESI-MS data will be reinforced with other techniques, such as UV-Vis and potentiometry, to better understand the Cu-Sb-Cit solution used to deposit Cu_2Sb.

Speciation calculations involve the computation of the concentration of each individual chemical species in a multifaceted chemical system.[30] They are used most often in complex systems to model the conditions for many different species. In addition, speciation diagrams are helpful for graphically visualizing the concentration of different species at different pH levels. For simple systems like citric acid this can be done with a spreadsheet using the equilibrium constant values, but for more complex systems a speciation software program is used to expedite the process. The speciation diagram of citric acid was calculated using Microsoft Excel as described in the book *Water*

Chemistry, by Mark Benjamin,[31] using the following equilibrium and pk_a values in Equations 3.3 through 3.5.[7]

$$H_3Cit \leftrightarrow H_2Cit^- \qquad pk_{a1} = 2.92 \qquad \text{Eq. 3.3}$$

$$H_2Cit^- \leftrightarrow HCit^{2-} \qquad pk_{a2} = 4.34 \qquad \text{Eq. 3.4}$$

$$HCit^{2-} \leftrightarrow Cit^{3-} \qquad pk_{a3} = 5.69 \qquad \text{Eq. 3.5}$$

The result is shown in Figure 3.6 for an ideal solution (without correction for activity) at a concentration of 10 mM. This result compared well to the speciation diagram of this system given by Rode *et al.*[28]

Citric acid was analyzed at pH values ranging from 1 to 9 on the ESI-MS. A representative spectrum at pH 6 is shown in Figure 3.7A. Peaks were identified based on calculating their individual mass to charge ratios (m/z). Citric acid has a mass of 192 g/mol, and is neutral (as in non-charged). In order to ionize, it has to gain (m/z = 193 in positive ion mode) or lose (m/z = 191 in negative ion mode) a proton. In addition, it can adduct with other ions in solution to form a charged ion that has the ability to "fly" through the MS. In both positive and negative ion mode, adducts are formed with water, potassium, and sodium as the ions try to minimize their surface energy (similar to a solvation sphere in liquid). Neither of these salts were added to the system, but they were present in their natural state from impurities in the materials or contaminants from the working area. Dimers form in the same way as adducts at higher mass ratios. They are not present in solution, and are postulated to form in the gas phase or at the liquid-gas interface.[15-16] A complete list of species identified in the citric acid solutions can be found in Appendix 3.2.

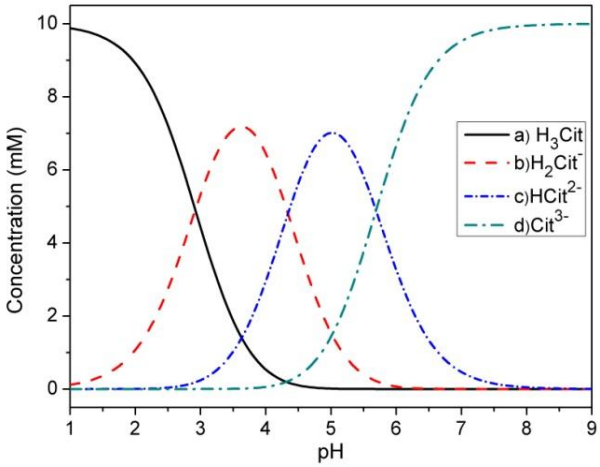

Figure 3.6. Calculated speciation diagram of an ideal solution of 10 mM citric acid. Calculated used Microsoft Excel.

In order to compare the speciation diagram to our ESI-MS data, the ion intensity of the 191 and 193 m/z peaks identified in the citric acid spectrum were evaluated based on their dependence on pH. Figure 3.7B is a plot of the species $[H_2Cit]^-$ and $[H_3Cit•H]^+$ as a function of $\overline{R}_k$ (calculated using equation 3.2) versus pH. In negative ion mode at a pH of 3, the most abundant species was the $[H_2Cit]^-$. Based on the speciation diagram, this species was already present in solution. All that had to happen in order for it to become ionized was for it to "jump" off the surface as described in one of the two mechanisms in the ESI process. As a result, $[H_2Cit]^-$ (m/z = 191) was the most abundant species in the negative ion mode spectra. The species H_3Cit was not ionized in solution and must adduct with something in order to "fly". One of those adducts is with H^+ to give the ionized form: $[H_3Cit•H]^+$ with a m/z equal to 193. Now, comparing the speciation diagram to the results shown in Figure 3.6, both figures show that H_3Cit has a maximum abundance below a pH of 3 and the H_2Cit^- species has a maximum abundance around a pH of 3.

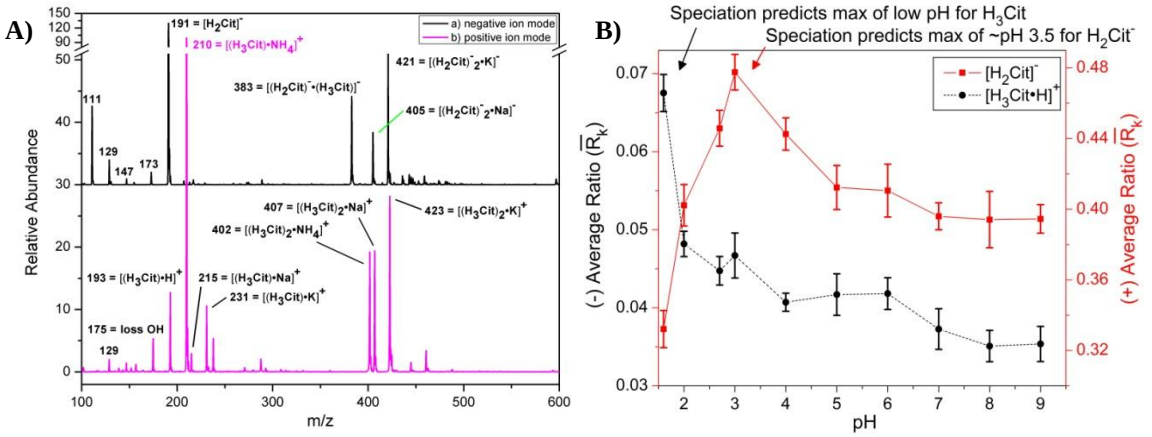

Figure 3.7. ESI-MS of citric acid in both negative and positive ion mode. A) ESI-MS spectra from the average of 50 ion scans in a) negative and b) positive ion mode of a 20 mM citric acid solution. B) Normalized abundance ($\overline{R}_k$) of $[H_2Cit]^-$ and $([H_3Cit•H^+]^+$ as a function of pH. Intensity of the peaks were taken from each individual scan and then normalized to the total ion count (TIC) as described in Equation 3.2. Each data point is from the average of 50 ion scans +/- the standard deviation of a 10 mM citric acid brought to pH with ammonium hydroxide. Maximum amounts match what was predicted by calculated speciation diagram shown in Figure 3.6.

Compared to citric acid, the speciation of copper citrate is more complex. There is a plethora of peaks in the spectrum, and it appears that the complexes in solution were forming larger clusters as they ionized, as can be seen in Figure 3.8A. These clusters consisted of multiple groupings of copper and citric acid that were singly charged. These ions most likely formed in the gas phase as they were trying to minimize their surface charge. A complete list of species identified in the copper citrate solutions can be found in Appendix 3.3. The process of identifying peaks was aided by using the isotope prediction freeware by Matthew Monroe, *Molecular Weight Calculator Version 6.45.* This software simulates spectra based on normal isotopic abundance of the elements. The spectra of the simulated species $[(H_2Cit)(H_3Cit)Cu]^+$ (m/z = 446) was in close agreement to that which was found experimentally as shown in Figure 3.8B.

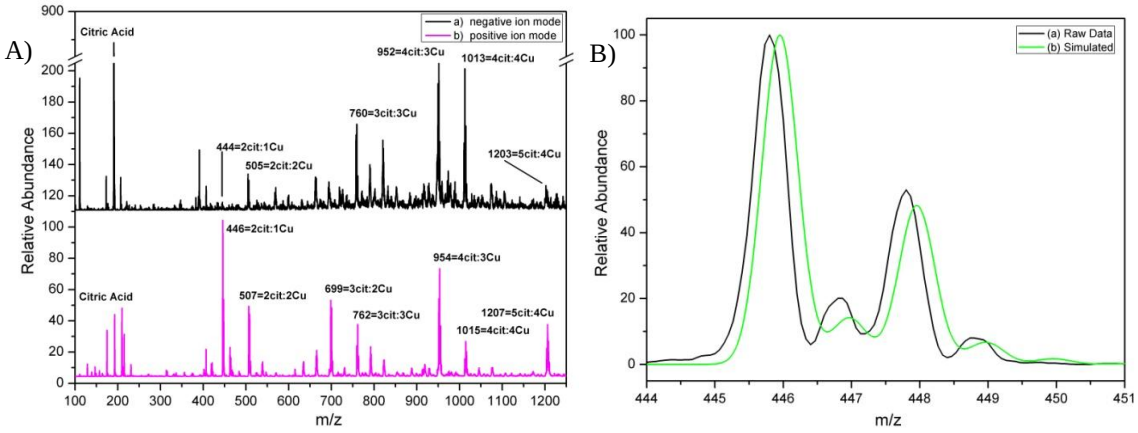

Figure 3.8. ESI-MS of copper citrate in both negative and positive ion mode. A) ESI-MS spectra from the average of 50 ion scans in a) negative and b) positive ion mode of a 4 mM $Cu(NO_3)_2$ in 20 mM citric acid. Loss of functional groups, adducts, and clusters complicate spectra. B) Simulated ($C_{12}H_{15}O_{14}Cu$) versus experimental data of the species $[Cu(H_2Cit)(H_3Cit)]^+$ (m/z 446) found in solution.

Copper citrate has been well studied in the literature and bridges almost five decades of research. Despite this long time-frame, it is difficult to compare the expected species for a given solution because the experimental conditions from which equilibrium constants are calculated vary. Rode *et al.* completed a literature survey outlining the copper citrate species described in the literature. A total of 14 species have been identified by various researchers, for which formation constants have been calculated. A summary of the abundance of the species based on deprotonation of the citrate are shown in Table 3.2. Based on data from this literature survey done by Rode *et al.*, we can expect that the major species present in solution for the 4 mM copper nitrate in 20 mM citrate are 1:2 (446 m/z) and 2:2 (507 m/z) copper to citrate species. Indeed, the most abundant species in our copper citrate ESI-MS spectra are the 1:2 species and the 2:2 species corresponding to a m/z of 446 and 507, respectively. Only minor amounts (<0.1%) of the 1:1 (254 m/z) and 2:1 (315 m/z) species are present. See Figure 3.9A for a representative spectrum of copper citrate in both negative and positive ion mode.

Table 3.2 Summary from a literature survey done by Rode *et al.* of expected copper citrate complexes at different ratios and pH values compared to what would be expected from the conditions of the deposition solution that Cu_2Sb can be electrodeposited from.[28]

Species	Reported Findings	Expected Cu-citrate abundance in deposition solution at pH of 6
1:1 (m/z = 254 +) and 1:2 (charge on $H_3Cit \leq 2$)	Only reported in solutions with pH ≤ 3	• Low
2:1 (m/z = 315 +)	Present only when large excess of copper (Cu/Cit ≥ 1)	• Our ratio = 0.2 → low amount
1:2 (m/z = 446 +)	Present only when large excess of citrate (Cu/Cit ≤ 1)	• Our ratio = 0.2 → present
2:2 (m/z = 507 +)	Main species even in rather dilute solutions	• Present in high amounts

The 1:2 and 2:2 species identified in copper citrate ESI-MS positive and negative ion mode spectra were normalized the same way as described for citric acid species in Equation 3.2, and Figure 3.9B shows the results of this normalization. The negative ion mode ESI-MS data does not show ideal correlation to the positive ion mode data because the counts in negative ion mode are two orders of magnitude lower for these particular species and are nearing the practical limit for recording the qualitative abundance of the species. Due to the ionization process, it is not possible to know exactly what solution species 1:2 and 2:2 peaks correspond to because multiply charged ions are rarely identified in ESI-MS spectra for metal-ligand complexes.[14] Instead, multiply charged species usually end up becoming singly charged (positive or negative) by the addition or subtraction of protons. To use the 2:2 species as an example: $[Cu_2(Cit)(H_{-1}Cit)]^{3-}$ is multiply charged, so two protons can be added to form $[Cu_2(Cit)(H_{-1}Cit)\bullet 2H]^{-}$ (m/z = 505), or four protons can be added to form $[Cu_2(Cit)(H_{-1}Cit)\bullet 4H]^{+}$ (m/z = 507). The possible species identification of the 446 and 507 species are described in Table 3.2 for positive ion mode. Based on this information, the results from Figure 3.9B compare well with what is expected based on Table 3.2. The largest abundance for the 2:2 species peak is obtained at a pH of approximately 7, while the abundance of this species decreases at

lower pH due to the formation of other copper citrate species and at higher pH due to copper oxide and hydroxide formation. Meanwhile, the 1:2 species $[Cu(HCit)(H_2Cit)]^-$ (m/z = 444) or $[Cu(H_3Cit)(H_2Cit)]^+$ (m/z = 446) increase in abundance at low pH, which is exactly what is predicted from the work of Rode *et al.*[28] However, due to the large abundance of the 1:2 species even at pH >5 there is most likely a large contribution from the a 1:2 copper to citrate ratio species with a larger deprotonation value; i.e. $[Cu(Cit)(HCit)]^{2-}$ or $[Cu(Cit)(HCit)]^{3-}$.

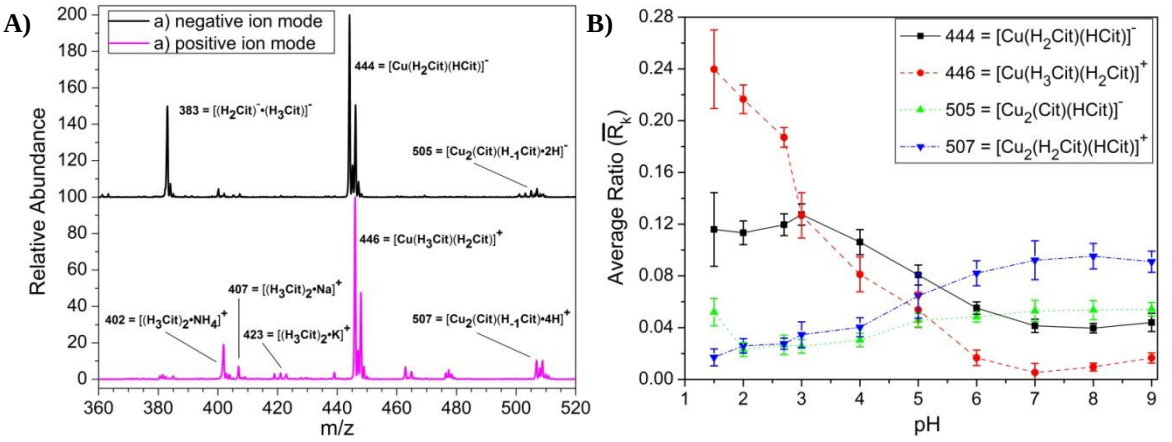

Figure 3.9. ESI-MS of copper citrate in both negative and positive ion mode identifying species present. A) ESI-MS spectra from the average of 50 ion scans in a) negative and b) positive ion mode of a 4 mM $Cu(NO_3)_2$ in 20 mM citric acid. Loss of functional groups, adducts, and clusters can be seen in the spectra. B) Normalized abundance ($\overline{R}_k$) as a function of pH of the main copper citrate species present in ESI-MS spectrum in positive ion mode. Intensity of the peaks were taken from each individual scan and then normalized to the total ion count (TIC), as described in Equation 3.2. Each data point is from the average of 50 ion scans +/- the standard deviation of a 20 mM citric acid 4 mM $Cu(NO_3)_2$ brought to pH with ammonia.

3.3.3. Species Identification of Sb-Citrate and Cu-Sb-Citrate using ESI-MS

By applying the knowledge gained from studies of the well understood solutions of citric acid and copper nitrate, we can be confident that our ESI-MS method is reliable for studying the more complex solution chemistry of antimony citrate and copper antimony citrate. The results in Figure 3.10A show the areas of interest for antimony citrate species in positive and negative ion mode at a pH of 6. According to Das *et al.*, the major species present in this solution is $[SbCitH_{-1}]^-$.[32] $[SbCitH_{-1}]^-$ is similar to the

species H_2Cit^- (m/z = 191), but unlike the citric acid case, $[SbCitH_{-1}]^-$ is not the most abundant species in the spectra. Since the species is already ionized in solution, there should be no issue with adduct formation being necessary to form ions, yet the species is very low in abundance. As shown in Figure 3.10A, a species with the correct m/z for this species (m/z = 309) is lower than 1% in the spectra and cannot be identified with confidence above the noise for this spectra. According to ESI-MS results, the most abundant species are $[Sb(HCit)_2]^-$ followed by $[Sb_2(H_{-1}Cit)(Cit)]^-$. These species will contribute to the electrodeposition of Cu_2Sb, or at least to the solution chemistry, more than the $[SbCitH_{-1}]^-$ species. A complete list of species identified in the antimony citrate ESI-MS spectra is shown in Appendix 3.4.

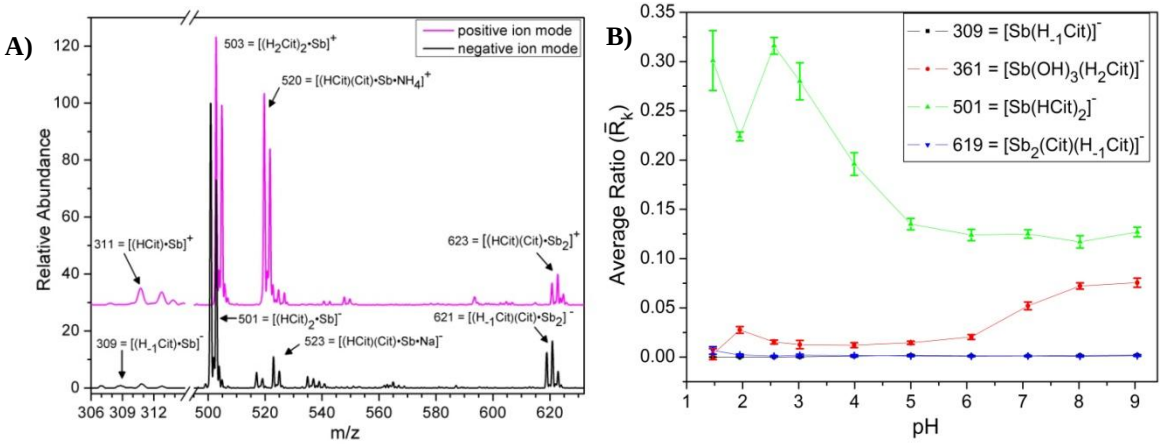

Figure 3.10. ESI-MS of antimony citrate in both negative and positive ion mode identifying species detected. A) ESI-MS spectra from the average of 50 ion scans in a) negative and b) positive ion mode of a 1.25 mM Sb_2O_3 in 20 mM citric acid brought to pH 6 with ammonia. B) Normalized abundance ($\bar{R}_k$) as a function of pH of the main antimony citrate species present in ESI-MS spectrum in positive ion mode. Intensity of the peaks were taken from each individual scan and then normalized to the total ion count (TIC) as described in Equation 3.2. Each data point is from the average of 50 ion scans +/- the standard deviation of a 20 mM citric acid 1.25 mM Sb_2O_3 brought to pH with ammonia.

The major species identified in antimony citrate ESI-MS negative ion mode spectra were normalized as described for citric acid species in Equation 3.2, and Figure 3.9B shows the results of this normalization. In addition to the already identified species mentioned above, there is a significant peak at higher pH with a m/z of 361 that

corresponds to the antimony citrate hydroxide species **[**$Sb(OH)_3(H_2Cit)]^-$, identified in the work by Hansen *et al.* [33-34] The species increases significantly in abundance at pH values greater than 6 due to the higher hydroxide concentration. All other antimony citrate species decrease with increasing pH. The $[Sb(HCit)_2]^-$ (m/z = 501) does not diminish to zero abundance, most likely due to the presence of antimony citrate species of greater deprotonation such as $[Sb(HCit)(Cit)]^{2-}$ and/or $[Sb(Cit)_2]^{3-}$.

Our ESI-MS results for antimony citrate are supported by results from several different authors. Zheng *et al.* studied similar concentrations of antimony citrate (0.9 mM Sb^{3+}/29 mM H_3Cit) with ESI-MS, and found the most abundant species in negative ion mode (besides other free citrate species) was also $[Sb(HCit)_2]^-$ (m/z = 501).[35] The results from crystal structures of complexes crystallized out of solution also showed the presence of complexes other than the $[SbCitH_{-1}]^-$ species. More recently, Tella *et al.* reported through X-ray Absorption Fine Structure Spectroscopy (EXAFS) that the antimony atom is coordinated to four oxygen atoms from two citric acid ligands.[36] Tella *et al.* also indicated many similarities in the citrate case to what has been previously reported for antimony tartrate, in which the major species are $[Sb_2(tartrate)_2]^{2-}$ and $[Sb(tartrate)_2]^-$.[37-38] X-ray diffraction studies of antimony citrate salts also show this type of coordination rather than a one-to-one coordination.[9, 39] Based on literature results and our own results from ESI-MS for the solutions analyzed, the main antimony citrate species seems to be $[Sb(HCit)_2]^-$ rather than the earlier reported $[SbCitH_{-1}]^-$.

Having studied three simple systems related to our main system of interest, and having identified the major species in these systems, all that is necessary is to look for the species in the combined Cu-Sb-Citrate spectrum that are not present in any of the other

systems in order to determine what is present in the solution used to deposit Cu_2Sb. Figures 3.11A and 3.11B show the ESI spectra of this dilute deposition solution overlaid with both the copper citrate and antimony citrate solutions at pH 6. The species highlighted around m/z = 563 in both positive and negative ion mode correspond to the neutral heterometallic Cu-Sb-Citrate species [CuSb(HCit)(Cit)], with a molar mass of 563 g/mol. Since it is neutral, the complex simply gains/loses a single proton, similar to the way citric acid is ionized.

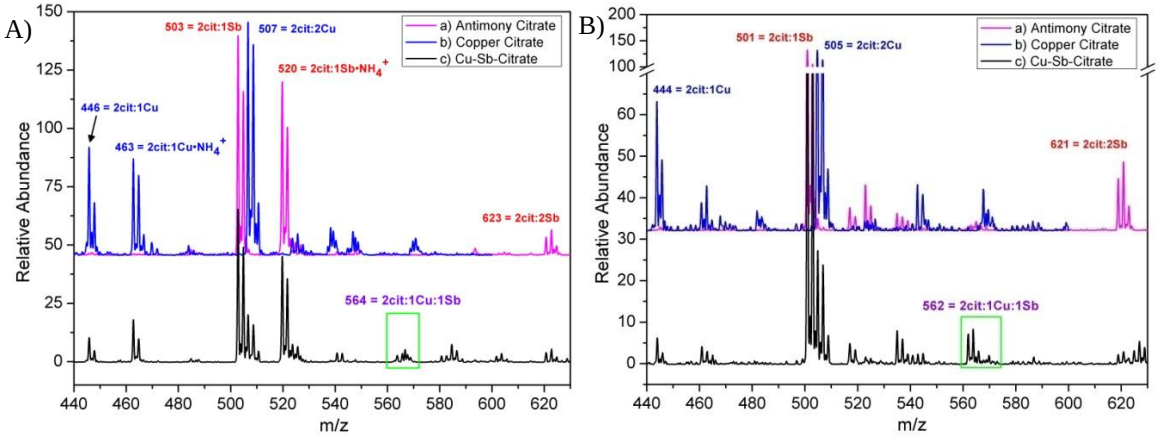

Figure 3.11. ESI-MS spectra from the average of 50 ion scans of both antimony citrate and copper citrate compared to the copper antimony citrate solution: A) positive ion mode and B) negative ion mode. a) 2 mm Sb^{3+} in 10 mM citric acid. b) 2 mM Cu^{2+} in 10 mM citric acid c) Both Sb^{3+} and Cu^{2+} in 10 mM citric acid in Heterometallic citrate species at m/z 564+ and 562- clearly visible. All brought to pH 6 with ammonia.

Further confirmation of the presence of [CuSb(HCit)(Cit)] is shown in Figure 3.12A, where the predicted isotopic ratio spectrum (found using *Molecular Weight Calculator Version 6.45* freeware, by Matthew Monroe) matches well with our raw data. The positive ion mode spectrum contains an additional species at a slightly higher mass, as shown in Figure 3.11A, b). This is likely an unidentified copper citrate cluster. Furthermore, the same plot of the major species in the Cu-Sb-Citrate solution as a function of $\overline{R}_k$ (calculated using equation 3.2) versus pH can be constructed as shown in Figure 3.11B. Though the Cu-Sb-Citrate solution has several additional species, many of

the same species identified in the original copper citrate and antimony citrate solutions can readily be identified in the combined solution. In comparing Figure 3.11B to the previously mentioned pseudo speciation diagrams (Cu-Citrate in Figure 3.10B and Sb-Citrate in Figure 3.10B), the general trends in species abundance versus pH are the same. This is as expected, because while the absolute abundance of the species may change, relative abundance at different pH values should not.

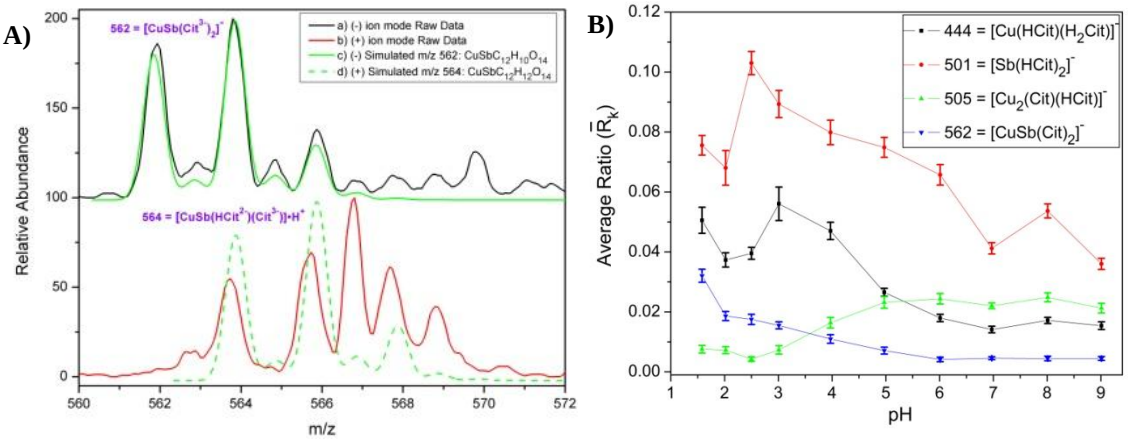

Figure 3.12. A) ESI-MS spectra from the average of 50 ion scans zoomed in on the heterometallic species from a 4 mM $Cu(NO_3)_2$ and 1.25 mM Sb_2O_3 in 20 mM citric acid solution brought to pH 6 with ammonia a) m/z 562 $[CuSb(Cit)_2]^-$ and b) m/z 564 $[CuSb(HCit)(Cit)•H]^+$. The same simulated isotopic abundance data for the species c) $CuSbC_{12}H_{10}O_{14}$ and d) $CuSbC_{12}H_{11}O_{14}H$. B) Normalized abundance ($\bar{R}_k$) as a function of pH of the main copper antimony citrate species present in ESI-MS spectrum in positive ion mode. Intensity of the peaks were taken from each individual scan and then normalized to the total ion count (TIC) as described in Equation 3.2. Each data point is from the average of 50 ion scans +/- the standard deviation of a 4 mM $Cu(NO_3)_2$ and 1.25 mM Sb_2O_3 in 20 mM citric acid solution brought to pH 6with ammonia.

The [CuSb(HCit)(Cit)] species is almost identical to the species mentioned in the introduction, $[CuSb(HCit)(Cit)(H_2O)_2]•2.5H_2O$, reported by Smith *et al.* from the crystal structure analysis of a solid complex obtained from the Cu-Sb-Citrate soluton.[9] Applying the knowledge gained from citric acid and copper citrate studies, the species in Figure 3.13A and 3.13B are most likely different forms of this heterometallic [CuSb(HCit)(Cit)] species, having different adducts present. The complete list of species identified in the copper antimony citrate solutions is given in Appendix 3.5. These

results are the first of their kind, showing significant evidence for a heterometallic citrate species present in solution.

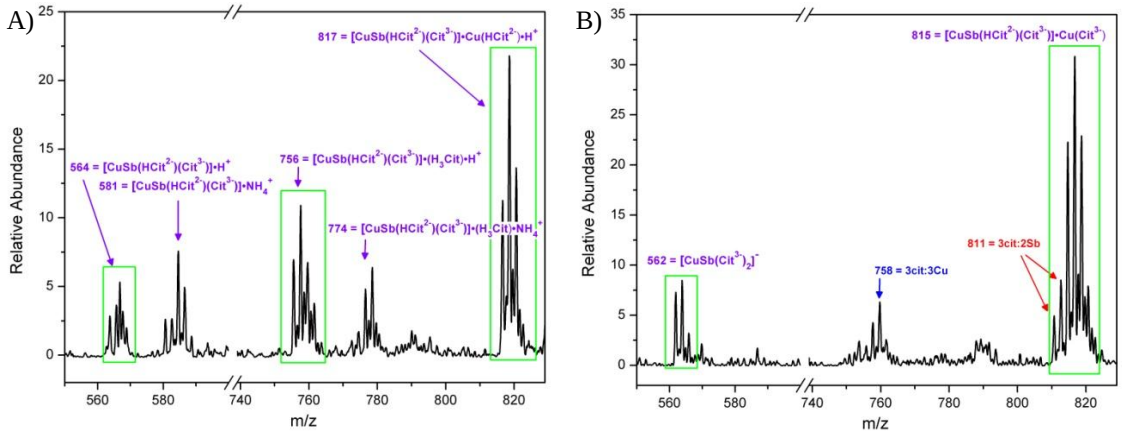

Figure 3.13. ESI-MS spectra from the average of 50 ion scans from a 4 mM $Cu(NO_3)_2$ and 1.25 mM Sb_2O_3 in 20 mM citric acid solution brought to pH 6 with ammonia in A) positive ion mode and B) negative ion mode. Labeled species match different adducts of the heterometallic species citrate [CuSb(HCit)(Cit)].

A summary the species identified in these ESI-MS studies is shown in Table 3.3. This table describes the complexes identified in solution, the literature source citing identification of each complex, and the m/z of each species detected.

Table 3.3 Complexes identified in solution by ESI-MS and confirmed in the literature.

Complex	**Reference**	**Species detected in ESI-MS (m/z)**
1:2 and 2:2 copper citrate species	Rode *et al.* [28]	444-, 446+ 505-, 507+
1:1 antimony citrate species	Das *et al.* [32],	309+
1:2 and 2:2 antimony citrate species	multiple sources[9, 35-39] (discussed in detail in conclusion),	501-, 503+ 621-, 623+
Antimony citrate hydroxide species	Hansen *et al.* [33-34]	361-
Copper antimony citrate species	Smith *et al.* [9]	564-, 566+

Figure 3.14A-C shows the structures of the species that are thought to exist in solution (the alpha hydroxyl groups are shown in red for clarity).

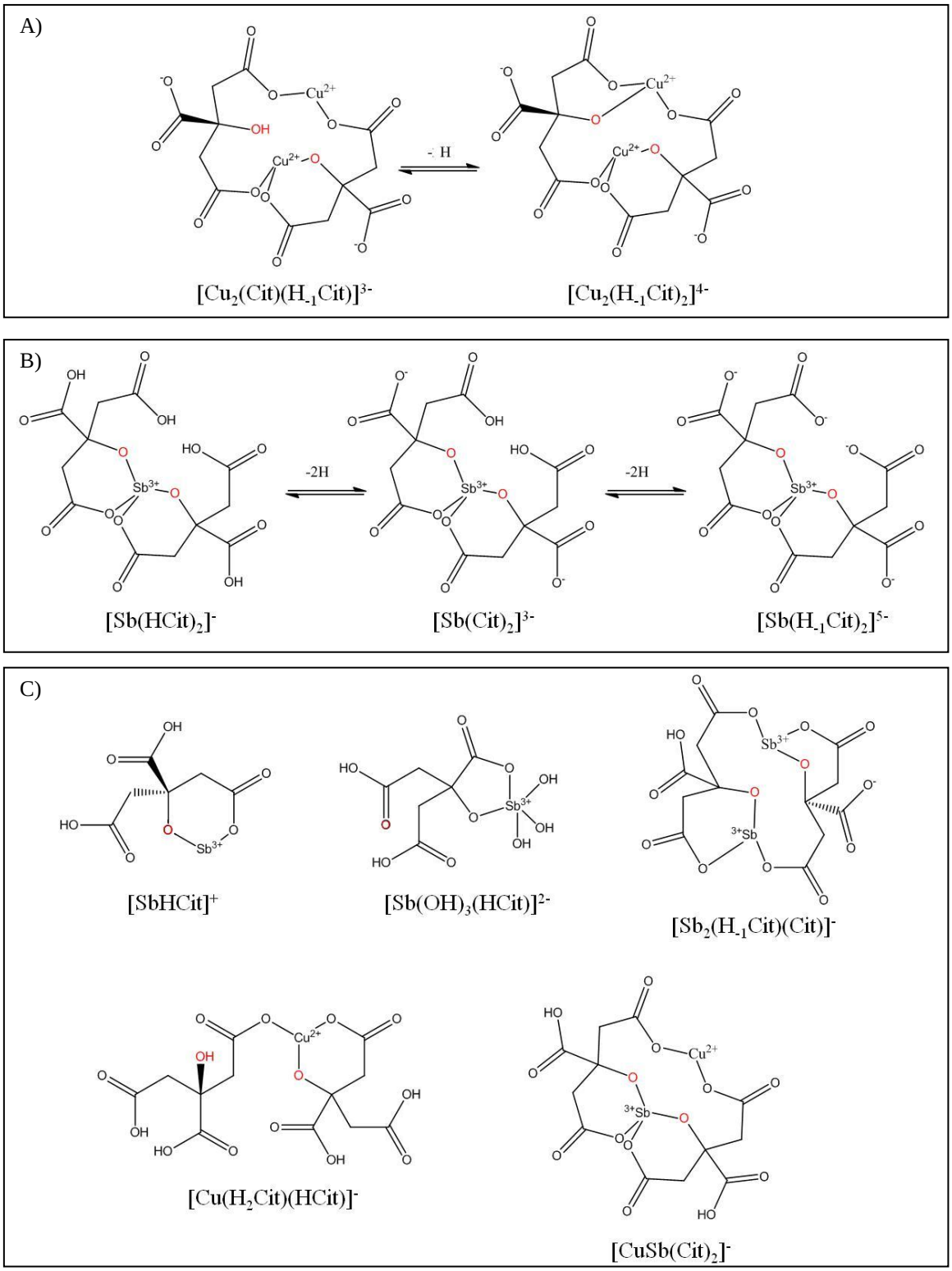

Figure 3.14. Proposed structures of species observed in solution using ESI-MS. In solution, the coordination sphere of the metals is completed with H_2O ligands. A) Main copper citrate species present in solution at pH 6 according to Rode et al., where $[Cu_2(Cit)(H_{-1}Cit)]^{3-}$ is responsible for copper deposition. B) Main antimony citrate species present in solution as determined by ESI-MS. The charge on the species is not known, but may deprotonated as shown as pH is raised. C) Other species found in ESI-MS results, including the heterometallic species $[CuSb(Cit)_2]^-$.

3.3.4. Discussion of Speciation of Antimony Citrate and Copper Antimony Citrate

To study the speciation of antimony citrate, several preliminary experiments were completed. To begin, several solutions were prepared from a stock solution of 0.2 M of citric acid by adding different amounts of antimony oxide. The solutions were left to stir for over a week to dissolve, to ensure they were all fully equilibrated, since the 3 most concentrated solutions still had solid un-dissolved. No pH adjustments were made. The initial pH values of all the solutions were between 1.7 and 1.9. The ratio of moles of citric acid to moles of antimony added ranged from 1:1 to 10:1. The antimony oxide dissolved in all but the three most concentrated solutions (1:1, 2:1, 3:1). To an aliquot of these solutions, copper was added so the Cu^{2+} concentration equaled 0.039 M. All of these solutions were then analyzed with the three techniques in consideration: UV-Vis Spectroscopy, ESI-MS, and potentiometric titration. A summary of the concentrations of each component added is shown in Table 3.4. The third entry (in italics) is a solution with the same ratios of all components as the Cu_2Sb deposition solution is composed of.

Table 3.4. Concentrations of solutions ran on UV-Vis, ESI-MS, and titrations. Solution in italics is at the same relative ratios that our deposition solution is run at.

Ratio Cit:Sb	Weighed Sb^{3+} (M)	Dissolved Sb^{3+} (M)	Measured Sb^{3+} (µM) UV-Vis	Cu^{2+} (µM) UV-Vis	Cu^{2+} (M) Visible	Ratio Cu:Sb	Ratio Sb:Cit
0	0	0	0	0	0	0	0
10	0.020	0.020	50	98	0.039	1.96	0.10
8	*0.025*	*0.025*	*63*	*98*	*0.039*	*1.57*	*0.13*
6	0.033	0.033	83	98	0.039	1.18	0.17
4.8	0.042	0.042	104	98	0.039	0.95	0.21
3.6	0.055	0.056	140	98	0.039	0.71	0.28
2	0.083	0.056	140	98	0.039	0.71	0.28
1	0.200	0.056	140	98	0.039	0.71	0.28
Citrate	n/a	n/a	n/a	n/a	n/a	n/a	n/a
Cu Cit	n/a	n/a	n/a	98	0.039	n/a	n/a
Cu Water	n/a	n/a	n/a	98	0.039	n/a	n/a

The dissolved portions of the solutions in Table 3.4 were diluted and the absorbance was measured in the UV-Vis. Since antimony citrate is a colorless solution, there is only one intense absorbance peak in the UV. This absorbance is due to ligand-to-

metal charge transfer from the binding carboxylate or hydroxyl group on the citric acid to the antimony ion. The absorbance spectra of the antimony citrate solutions are shown in Figure 3.15A, and the saturated solutions (not shown) have the same absorbance. At a wavelength of 205 nm, the absorbance was plotted versus concentration of antimony. From the best-fit line in Figure 3.15B, the concentration of the saturated solutions were calculated and corresponded to a ratio of 3.6 citrates per antimony, or 140 ± 2 µM.

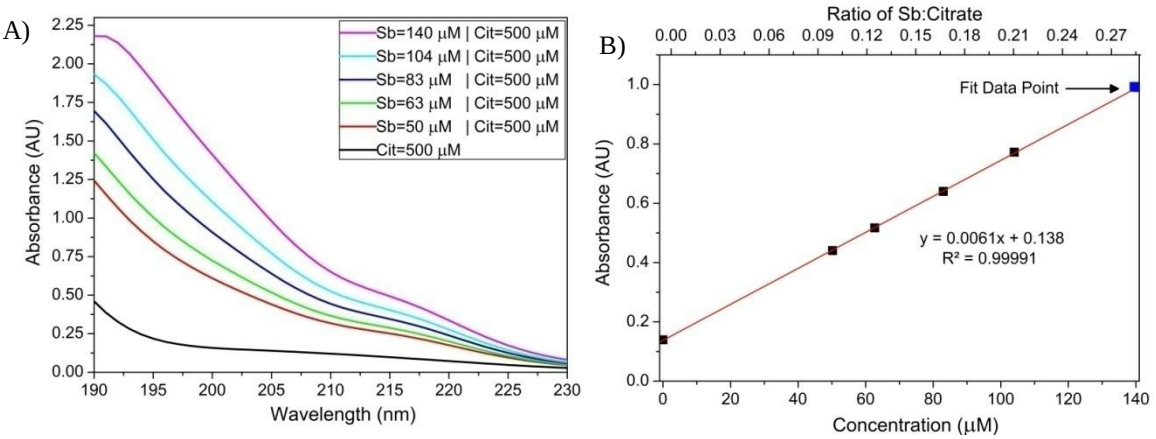

Figure 3.15. Absorbance of the antimony increases linearly with concentration until the saturation point of 3.6 citrates per antimony. A) UV spectra at initial pH of antimony citrate. B) The concentration of the saturated solution was calculated to be 140 ± 2 µM from the average of the three saturated solutions.

The results from UV-Vis indicate the minimum amount of citrate required to dissolve one antimony atom is 3.6 equivalents. This ratio points to an equilibrium in which multiple antimony citrate species must be involved in the dissolution of antimony oxide. It is established that, in water, antimony oxide is in equilibrium as shown in equation 3.6:[40-42]

$$Sb_2O_3 \leftrightarrow Sb(OH)_3 \leftrightarrow Sb(OH)_x^{n+} \leftrightarrow Sb^{3+} \quad \text{Eq. 3.6}$$

The antimony can then exchange in a stepwise process with citric acid, which is in equilibrium with various protonated species (shown in Eq. 3.7).

$$H_3Cit \leftrightarrow H_2Cit^- \leftrightarrow HCit^{2-} \leftrightarrow Cit^{3-} \leftrightarrow H_{-1}Cit^{4-} \quad \text{Eq. 3.7}$$

The overall equilibrium of all these species is what is in solution and what the ESI-MS spectra will report.

The solutions in Table 3.4 were run on ESI-MS, and the results from these antimony citrate solutions are shown in Figure 3.16A. These results were normalized to ($\overline{R}_k$) using equation 3.2. All the antimony species increased linearly in abundance with increasing antimony concentration, so the most abundant species $[Sb(HCit)_2]^-$ (m/z = 501) is the only antimony citrate plotted (for clarity). If the abundance of antimony citrate species is increasing with increasing antimony concentration, it is expected that the free citrate in solution simultaneously decreases, which is indeed the observed effect. The copper addition solutions were also run on the ESI-MS, and are shown in Figure 3.16B. Even with the added copper in solution, the ESI-MS results show that all antimony species increase in abundance with the increase in amount of antimony added, and that free citrate ions in solution decrease. The copper citrate species $[Cu(H_2Cit)(HCit)]^-$ (m/z = 444) is more abundant when there is more citrate to bind to. Interestingly, the heterometallic Cu-Sb-citrate species with a m/z ratio of 562 increases in a similar manner as the antimony citrate species, but the relative abundance is much lower. As the amount of antimony increases, a greater amount of the heterometallic species can form as the equilibrium shifts further in favor of the antimony species.

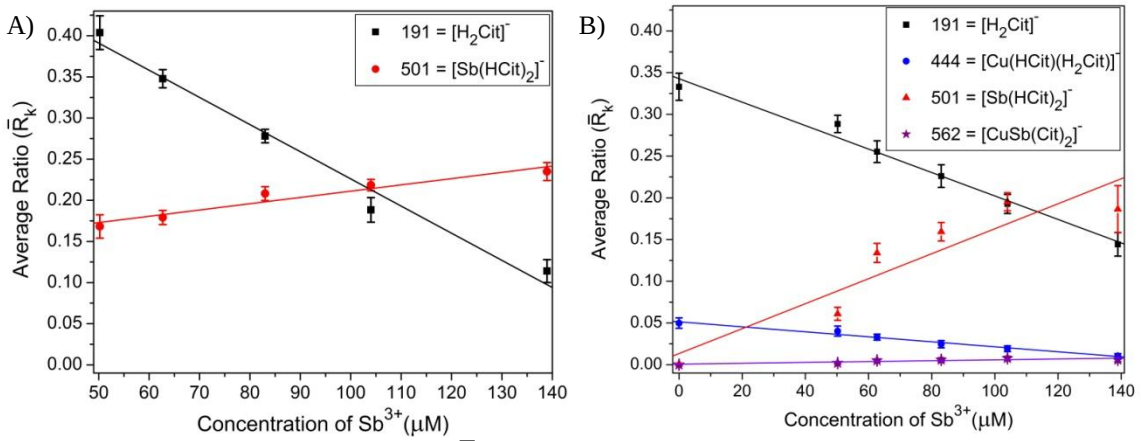

Figure 3.16. Normalized abundance ($\bar{R}_k$) as a function of pH of solutions containing increasing amounts of antimony and constant amounts of citrate. A) In a solution of Sb_2O_3 in 500 μM citric acid the citrate species $[H_2Cit]^-$ decreases with increasing antimony, while all antimony species increase with increasing antimony concentration. Only the most abundant species $[Sb(HCit)_2]^-$ (m/z = 501) plotted for clarity. B) In a solution of Sb_2O_3 in 500 μM citric acid spiked with 98 μM $Cu(NO_3)_2$ the citrate species $[H_2Cit]^-$ and $[Cu(H_2Cit)(HCit)]^-$ decrease with increasing antimony, while all antimony species and the heterometallic species $[CuSb(Cit)_2]^-$ increase with increasing antimony concentration.

It is useful for the discussion of the UV-Vis absorption spectra of copper to understand the likely electronic transitions it is undergoing. Molecular Orbital (MO) theory states that, for molecules with octahedral geometry, the d orbitals are split into two energies: $\underline{e_g}$ at higher energy and $\underline{t_{2g}}$ at lower energy (while the exact opposite is true for molecules of tetrahedral geometry). Because of Jahn-Teller distortions in copper, these orbitals further distort due to elongation or compression (for copper it is usually an elongation).[43] This Jahn-Teller distortion means that the t_{2g} splits into the $\underline{xz/yz}$ *(e_g orbital)* and $\underline{xy}$ *(b_{2g} orbital),* and the $\underline{e_g}$ splits into the $\underline{z^2}$ *(a_{1g} orbital)* and $\underline{x^2\text{-}y^2}$ *(b_{1g} orbital)* as shown in Figure 3.17A. When discussing the electronic transitions, these orbitals need to be lettered from the bottom up. The orbital with the highest energy gets the ground state and a capital letter. Figure 3.17B shows this for copper in the ^2D Free Ion Term, where the B_{1g} is the ground state.[43]

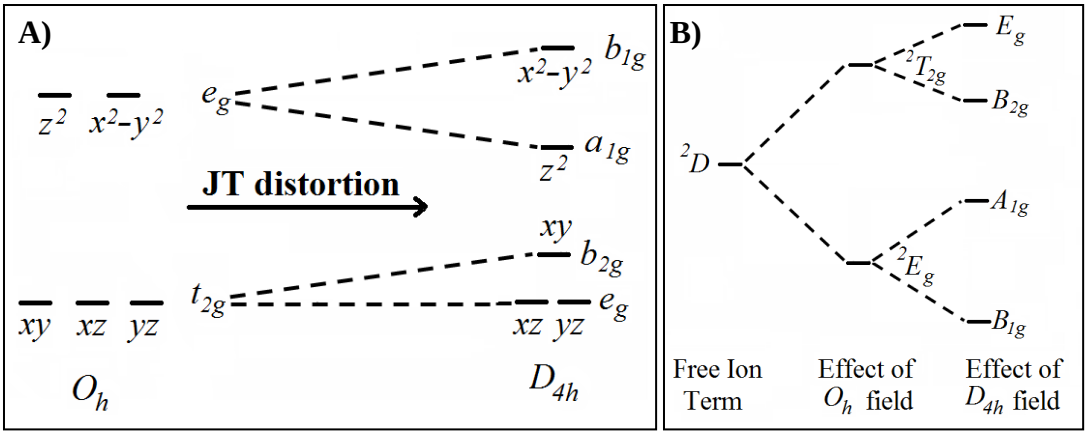

Figure 3.17. A) The d-d transitions allowed for copper as predicted from MO theory and B) corresponding ^{2}D Free Ion Term.

The absorbance spectrum of copper citrate consists of a broad d-d absorption centered at ~775 nm along with the carboxylate to copper charge-transfer band in the UV range.[44] The d-d transitions are namely:

- $d_{xz}(d_{yz}) \rightarrow d_{x2-y2}$
  - $B_{1g} \rightarrow A_{1g}$
- $d_{xy} \rightarrow d_{x2-y2}$
  - $B_{1g} \rightarrow B_{2g}$
- $d_{z2} \rightarrow d_{x2-y2}$
  - $B_{1g} \rightarrow E_g$

The λ_{max} of the d-d band transitions can be expressed as the sum of individual ligand-field contributions from all the donor atoms. For copper, the donor atoms are usually in the square plane and the axial ligands are generally water molecules, but in some cases they may be ligand donor atoms.[45] The energy of a transition is determined by the nature of the less strongly bonded axial ligands as well as by the four donor atoms in the plane.[46] Higher values of ε_{max} for a copper (II) complex can be obtained by coordinating more donor atoms in the square plane, which causes a blue shift in λ_{max}.[47] Increased axial coordination by other groups besides water decreases the energy of the transition and produces the so called "pentammine effect" observed for $Cu(NH_3)_5^{2+}$, which red shifts the λ_{max} back to higher wavelengths. Similar shifts to lower energy occur

with other groups in the axial position such as carboxylate or hydroxyl groups, but the effect is less dramatic.[45]

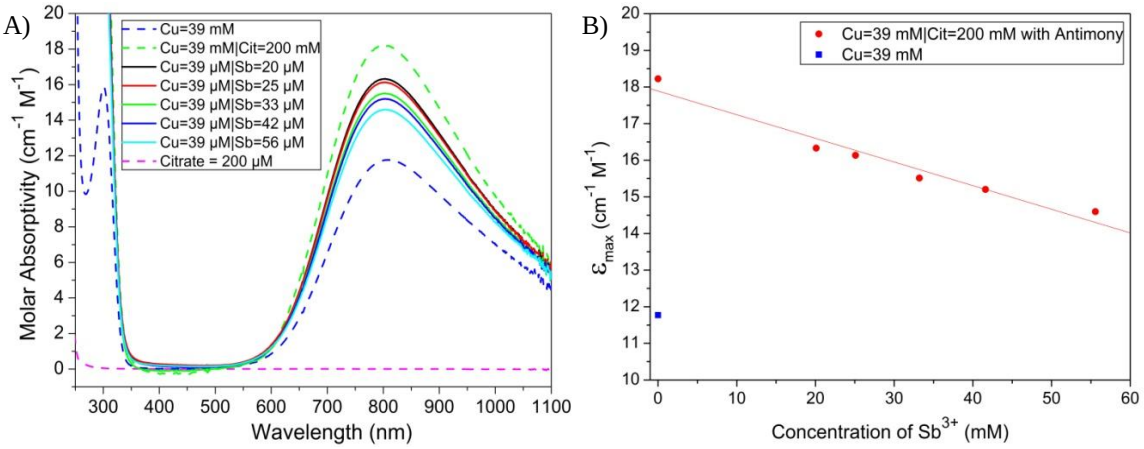

Figure 3.18. A) UV-Vis spectra of solutions containing the same amount of citric acid (200 µM) and copper with different amounts of antimony. (B) Corresponding ε_{max} versus change of antimony concentration.

An absorption spectrum of each of the copper containing solutions in Table 3.4 was collected and is shown in Figure 3.18A. The absorbance of this d-d absorption peak is dependent on the amount of copper citrate formed.[48] The copper citrate solution without any antimony in solution has the largest absorbance. A copper interacting with water without citrate or antimony has the lowest absorbance. The concentration of antimony affects the copper absorption linearly, as plotted in Figure 3.18B, where it shows that the higher the concentration of antimony, the lower the absorbance of the copper d-d electronic transition. This lower absorbance is most likely caused by a decrease in free citrate present available since more of it is binding in the antimony citrate species. This causes more free copper to interact only with water rather than citrate. It is interesting to note that the peak maximum absorbance of both the copper water and copper citrate solutions is at the same λ_{max}. UV-Vis spectra of the solutions were measured immediately upon copper addition and again 24 hours later. The

absorption spectra were identical, demonstrating that the system reaches equilibrium within five minutes.

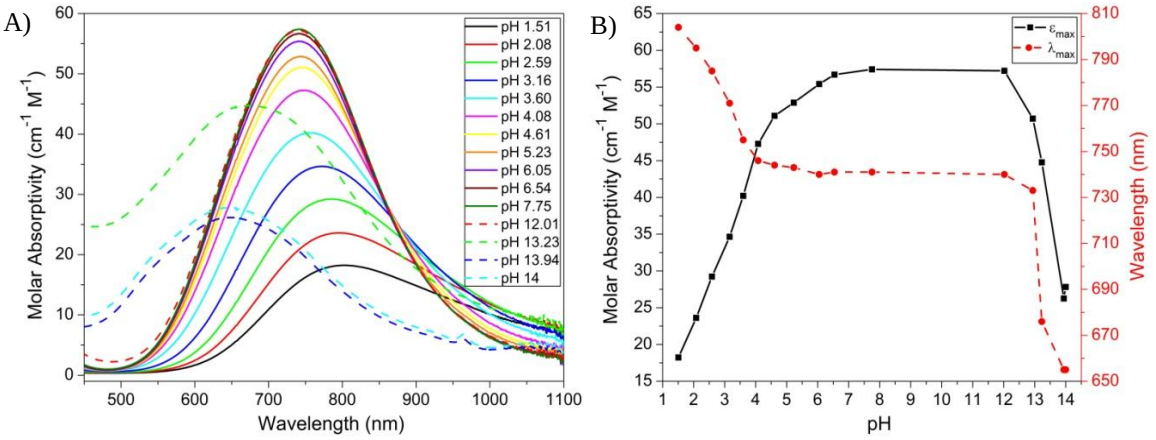

Figure 3.19. (A) Copper Antimony Citrate absorbance from pH 1.51-14. (B) Change in λ_{max} and ε_{max} versus pH of copper antimony citrate solution (Cu^{2+} = 20 mM | Sb^{3+} = 17 mM | citrate = 100 mM).

The spectrum of the copper citrate and copper antimony citrate solutions is much more interesting, since the absorbance spectrum changes with pH to a greater extent. The d-d absorption peak in the visible spectrum changed in intensity and wavelength with increasing pH. The absorbance spectrum is shown in Figure 3.19A. The absorptivity increases to a maximum value at pH 8 and then decreases due to the formation of hydroxo species.[49] The λ_{max} decreases and moves to higher energy. The plot of ε_{max} and λ_{max} versus pH is shown in Figure 3.19B. The ε_{max} change with pH in Figure 3.19B looks very similar to the copper citrate ESI-MS data taken for the $[Cu_2(Cit)(_{H-1}Cit)\bullet 4H]^+$ (m/z = 507 in Figure 3.9), and is comparable with the speciation diagram for the Cu_2Cit_2 species shown in Rode's work, where the abundance of the Cu_2Cit_2 increased with higher pH values.[28] The λ_{max} shifts to lower wavelengths due to the increase in the number of oxygen donors, meaning that in copper's case there are more citrates binding with increasing pH or oxygen functional groups from individual citrates.[7] The dimer structure could be two equivalent copper ions that are both coordinated by three carboxalate

groups and one alcoholate group, as proposed by Boas *et al.*[50] According to Lizama *et al.,* at lower pH values the absorbance spectrum is shifted to higher wavelength due to the dominance of $(Cu_2Cit_2H_{-1})^{3-}$ species, and at higher pH is shifted to lower wavelengths and higher absorbance values since the $(Cu_2Cit_2H_{-2})^{4-}$ species begins to dominate and is more optically active.[48]

Daniele *et al.* suggested that a substitution of one copper in the dimer by another metal could be accomplished without structural changes to the second copper when similar values of absorptivity and wavelength of maximum absorbance are obtained.[7] Both Lizama *et al.* and Petit-Ramel *et al.* have shown a very similar absorbance spectrum at different pH values for copper citrate.[48, 51] If a shift in λ_{max} occurs, it may indicate a binding change due to the presence of a copper antimony citrate species. Figure 3.20 is a plot of the copper antimony citrate and copper citrate solutions at different pHs: initial pH, pH 4 and pH 6. There is no change in λ_{max} in the copper antimony citrate solutions compared to the copper citrate solutions at any pH value. The ε_{max} for the solutions, on the other hand, *does* change. Looking at the initial pH solutions, the more antimony added the less intense the absorption is at 800 nm. This indicates that with more antimony citrate there are fewer copper citrate complexes, which leads to a lower overall absorbance for the heterometallic solution because there is additional free Cu^{2+} that interacts with water. However, at pH 4 and pH 6 the ε_{max} switches trends. The solutions with the highest amount of antimony have the highest absorbance. Since antimony does not absorb in this wavelength range, it is interesting that it is affecting the ε_{max} of copper.

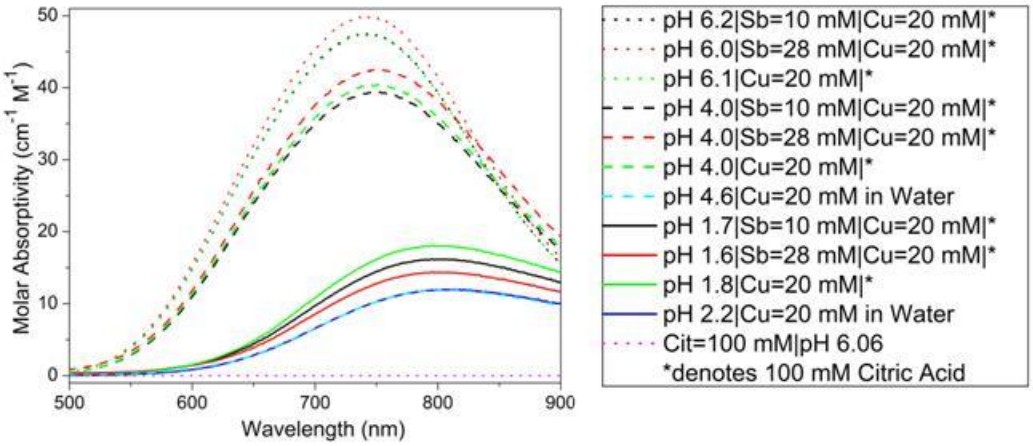

Figure 3.20. Visible absorbance spectra comparing the transitions from solutions of copper in water, copper citrate and different amounts of antimony in copper antimony citrate solutions

There are three possible explanations for the increase of ε_{max} with increased pH. (1) The first is that the antimony is binding in a heterometallic Cu-Sb-Cit complex and influencing the copper-carboxalate interaction, thus making the transition stronger. For example, if the antimony in the heterometallic was bound to two carboxylate and two hydroxyl ligands, it would leave the copper to bind to four carboxylates in the square plane of copper, making the transition stronger. This explanation seems unlikely since a slight shift in the wavelength would be expected, but is not observed. (2) The second possibility is that, since it was shown that heterometallic Cu-Sb-Cit species are present in solution, so or every Cu-Sb-Cit species formed, one copper would be left to go bind to something else. At pH 6, the most abundant species is the $(Cu_2Cit_2H_{-2})^{4-}$ species that has the highest ε_{max} for this citrate bath. (3) The third possibility is the large abundance of the $[Sb(HCit)_2]^-$ (m/z = 501) species in the ESI-MS spectra, even at pH values of 4 and 6 (see Figure 3.10B), are shifting the overall equilibrium further to the more deprotonated $(Cu_2Cit_2H_{-2})^{4-}$ species which is more optically active.[48]

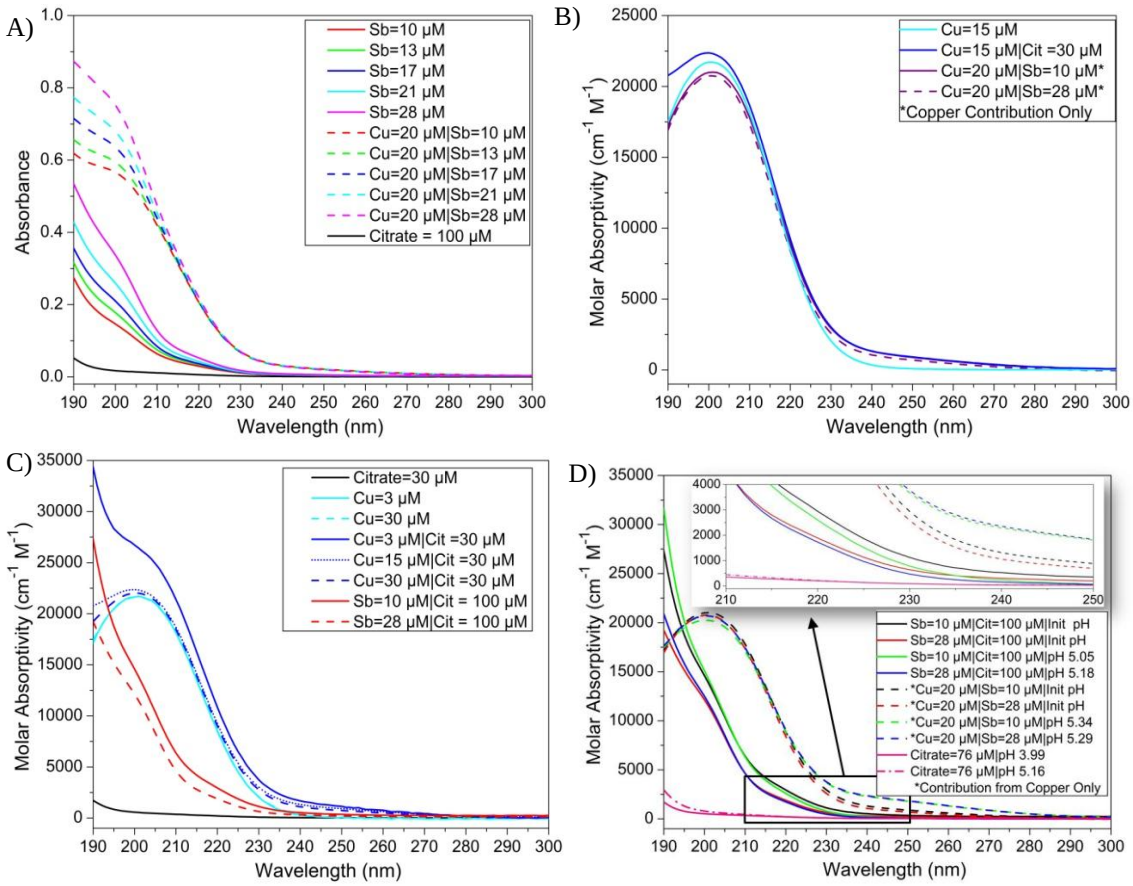

Figure 3.21. UV spectra comparing the different transitions in the UV range for from solutions of copper in water, copper citrate and different amounts of antimony in copper antimony citrate solutions. A) Absorbance in UV range of solutions antimony citrate compared to copper antimony citrate. Increased concentration of antimony increases absorbance. B) Molar absorptivity of the copper antimony citrate solutions with contribution from the absorbance of antimony subtracted from the spectra. C) Molar absorptivity of copper in citric acid compared to water plotted along with the antimony citrate molar absorptivity. Increased metal citrate binding increases the molar absorptivity for the copper, but decreases with antimony. D) Comparison of two different concentrations of antimony in citric acid and antimony in copper citrate at two different pH values.

Figure 3.21A is the absorbance plot in the UV region of the same solutions described above, but with a 1:1000 dilution. Increasing the concentration of antimony increases the absorbance of the antimony citrate solutions, as well as the solutions with the copper addition. In order to probe the increase in absorbance of the heterometallic solution, the absorbance of each antimony citrate solution was subtracted from the corresponding heterometallic solution. If there is significant contribution from a heterometallic Cu-Sb-Citrate species, there should be a change in molar absorptivity

based on how much Cu-Sb-Citrate species is formed. Figure 3.21B is the corresponding molar absorptivity plot of just the copper contribution to the UV absorbance of the heterometallic solution. As Figure 3.21B shows, the concentration of antimony does not affect the molar absorptivity of the copper portion of the absorbance. In fact, it looks very similar to the copper absorbance of the copper water solution. The copper citrate absorptivity is the only absorptivity that changes at all, and that is only in the far UV between 190-200 nm.

Figure 3.21C shows the corresponding molar absorptivity of the copper water, copper citrate, and antimony citrate solutions at different concentrations of metal ion. As expected, the copper water solution has the same molar absorptivity regardless of concentration, just as in the visible range spectra. The copper citrate, however, does show a change in absorptivity based on concentration. This change in absorptivity indicates a change in speciation. Most likely, the amount of free Cu^{2+} (copper water) decreases relative to the copper citrate species. The major species at this initial pH of 3.0 is the $Cu(Citrate)_2$, where the deprotonation is less than 2: ($[Cu(H_2Cit)(HCit)]^-$ and $[Cu(H_2Cit)_2]$).[28] The antimony citrate also has a change in molar absorptivity when the concentration is changed. For the antimony citrate solutions, there is a decrease in absorptivity when increasing the concentration. This indicates that there are at least two different antimony citrate species in solution. Looking back at the ESI-MS plot in Figure 3.10B, the ESI-MS results show the amount the species $[Sb(HCit)_2]^-$ decreasing with increased pH, but there is still a significant amount of the antimony species $[Sb(HCit)_2]^-$ present at a pH of 5 and above. Since all of the other antimony citrate species decrease in abundance with increased pH in the ESI-MS plot, the decrease must be due to a different

protonated species being the major absorber. For example, $[Sb(HCit)_2]^-$ may have a greater absorbance than $[Sb(Cit)_2]^{3-}$. This is similar to what happens with copper citrate, though in the opposite direction, where the absorptivity increases when the major species in solution shifted from $(Cu_2Cit_2H_{-1})^{3-}$ to $(Cu_2Cit_2H_{-2})^{4-}$ making it more optically active.[52]

Finally, Figure 3.21D is a plot of the antimony citrate species and copper contribution from the heterometallic solution at different pH levels. The molar absorptivity of the antimony citrate solution increases with increased pH at UV wavelengths between 190-200 nm. In this region, the slight increase in absorptivity with increased pH can be attributed to citric acid, since it is more optically active in the far UV as shown. However, the inset in Figure 3.21D, particularly around 220 nm shows that there is actually a local decrease in absorptivity with increased pH. There is no contribution from citric acid here, so absorbance at this wavelength can be used as an indicator of the antimony citrate complex. This decrease in absorptivity is expected since ESI-MS results show a decrease in the $[Sb(HCit)_2]^-$ (m/z = 501) species as the pH rises. Since the decrease is even more apparent at high pH, there must be a greater contribution from the higher deprotonated species, as mentioned above. Looking at the copper contribution of the heterometallic solution, there is no change in the absorbance peak at 250 nm, but around 240 nm there is a difference in the absorptivity. This peak follows the same trend as absorbance in the visible range, since this absorbance is for copper. See Figure 3.20 for a more detailed explanation of copper's visible transitions.

The UV and visible spectrophotometric results on the antimony citrate and copper antimony citrate solutions confirm the results obtained from ESI-MS and indicate the presence of a differently deprotonated $[Sb(Cit)_2]^X$ species present at higher pH values. It

is not possible to know the exact charge on the $[Sb(Cit)_2]^X$ species by either ESI-MS or UV-Vis, but the UV-Vis results seem to indicate more than one antimony citrate species present. The visible ε_{max} of copper changes with the addition of antimony. At different pH levels, the addition of antimony has different effects on the $\varepsilon_{max,}$ which again indicates multiple antimony citrate species present, a significant absorption from a heterometallic Cu-Sb-Cit complex, or an equilibrium shift to the more optically active $(Cu_2Cit_2H_{-2})^{4-}$ species. To learn the actual charge on the species found present in the ESI-MS and UV-Vis results, Potentiometric titrations are used.

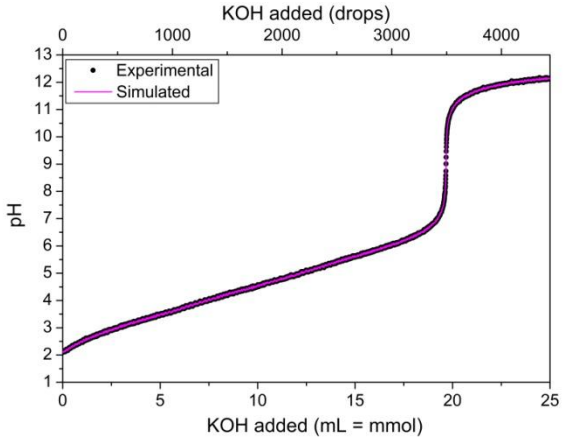

Figure 3.22. Slow titration curve of 0.2 M citric acid and 0.1 M KNO_3 with 0.1M KOH compared to simulated titration using Visual MINTEQ.

Potentiometric titrations are another way to determine equilibrium constants. However, in order to use this technique, the equivalence points of the different species must be far enough apart from one another to simulate the titration curve. The purpose of the initial study is to determine if it is possible to use titrations to gain species identification for the antimony citrate solutions and copper antimony citrate solutions. In addition, it is beneficial to do many different titrations, recording many data points for each curve, in order to see how the curves change with experimental conditions, if at all. Based on these desires, a drop counting "semi-auto" titration technique was adopted.

This technique was chosen because, ideally, a data point is recorded for each drop added. By adjusting the concentration of the titrant used, as many or few drops as desired can be recorded for each titration.

The first set of titrations completed were on citric acid. Citric acid is a triprotic acid with an equilibrium according to equation 3.8: [53-54]

$$H_3Cit \leftrightarrow H_2Cit^- \leftrightarrow HCit^{2-} \leftrightarrow Cit^{3-} \qquad \text{Eq. 3.8}$$

$pk_{a1} = 3.13$, $pk_{a2} = 4.76$, $pk_{a3} = 6.40$

Since the pk_a values are less than 2 pH units away from one another, the individual equivalence points for each deprotonation will not be seen.[55] There is an additional fourth proton that can be removed from the hydroxyl group. This hydroxyl is important in metal complexation, and it shifts to much lower pH values when metal ions are present. This is because the coordination effects with metal ions make the hydrogen of the hydroxyl group much more labile.[28] Without metals present it has a very high pk_a that was only recently measured.[54] This equilibrium and pk_a value are shown in equation 3.9:

$$Cit^{3-} \rightarrow H_{-1}Cit^{4-} \qquad \text{Eq. 3.9}$$

$pk_{a4} = 14.4$

The titration of citric acid with KOH completed with the drop counter is shown in Figure 3.22. KNO_3 was added to keep the ionic strength constant. The titration was done very slowly with dilute KOH, and therefore over 4000 data points were collected with many points recorded within the equivalence region. A simulated titration curve was produced with Visual MINTEQ 3.0, and it is an excellent match to the experimental curve.

Since a drop counter is employed, it is important to get an idea of the reproducibility of gathering data using this technique. Citric acid was titrated in triplicate and the data collected is shown in Figure 3.23A. The equivalence points do not match completely because the drop counter does not reliably count every single drop, and the drop volume could change over the course of the titration. However, the curves before the equivalence region match identically. Based on the consistency of the shape of the curve, the copper citrate, antimony citrate, and copper antimony citrate solutions were titrated. These results are shown in Figure 3.23B. Again, there is a small discrepency at the equivalence point from one trial to the next due to the drop counter, but the curves are still in close agreement. Based on these results, the drop counter titration method is great for obtaining the shape of titration curves for comparison between different solutions. As an added benefit, there is a low amount of time required to obtain the titration curves.

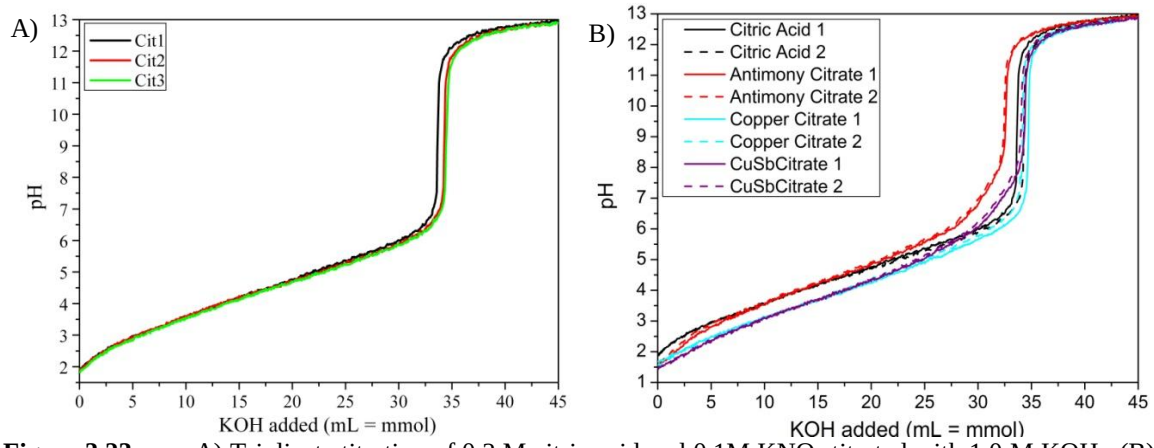

Figure 3.23. A) Triplicate titration of 0.2 M citric acid and 0.1M KNO_3 titrated with 1.0 M KOH. (B) duplicate titrations of citric acid, 0.0125 M Sb_2O_3 citrate, $Cu(NO_3)_2$ citrate, $Cu(NO_3)_2$ and 0.0125 M Sb_2O_3 citrate all with citric acid concentration 0.2 M and 0.1M KNO_3 titrated with 1.0 M KOH.

The solutions that had different ratios of antimony to citrate as described in Table 3.4 were titrated twice with 1.0 M KOH and contained 0.1 M KNO_3 to keep the ionic strength constant. The titration curves of the least and most concentrated antimony solutions are shown in Figure 3.24. In addition, the simulated titration curve for the

highest concentration of antimony is also shown in Figure 3.24. At the large equivalence region there is no trend between the titration cuves. However, with antimony in the solution there are additional equivalence points at around 14 millimoles and 1 millimole (indicated by arrows) of added KOH. These equivalence points are linear with respect to the concentration of antimony.

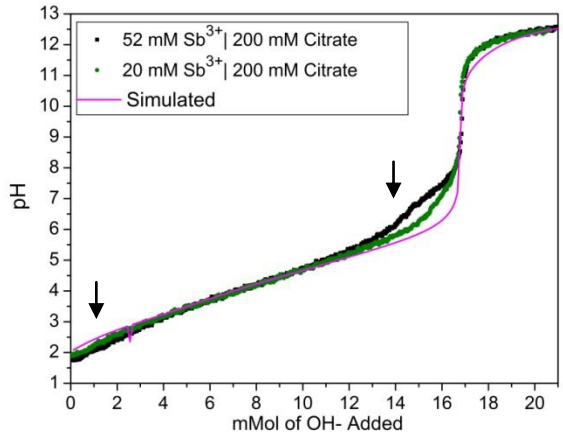

Figure 3.24. Titration curve of different concentrations of antimony added to 0.2 M citric acid and 0.1 M KNO_3 with 1.0 M KOH.

At the low equivalence point (pk_a ~ 2), more hydroxide is needed with increasing antimony concentration. This indicates an increase in the antimony citrate species, because as more antiomny citrate complexes are formed, more protons are released from citric acid by its complexation with antimony, and therefore more hydroxide is needed to maintain the same pH level. The equivalence point at around 14 millimoles of added hydroxide (pk_a ~ 4), shows the increased concentration of antimony requires fewer moles of hydroxide to obtain the same pH value. If a hydroxide antimony citrate species is formed, then it would still require additional hydroxide to neutralize it. So then, at this pH, the hydrolysis of antimony occurs and antimony is removed from the citric acid, which then takes protons from solution and increases the pH.

Based on the above results of ESI-MS, UV-Vis, and a qualitative look at the titration curve for this system, a set of equilibria have been established. Initially, $[Sb(HCit)_2]^-$ is present based on the dissolution given previously in equations 3.6 and 3.7. At the the first equivalence point, a different protonated species of antimony citrate is formed as shown in equation 3.10:

$$[Sb(HCit)_2]^- \leftrightarrow 2H^+ + [Sb(Cit)_2]^{3-} \qquad pk_{a1} \sim 2 \qquad \text{Eq. 3.10}$$

Subsequently, there is a transition to the higher deprotonated form $[Sb(Cit)_2]^{3-}$ through a set of equilibria, but since the pKa's are less than 2 pH units apart it is not possible to see this equivalence point in the titration curve. This transition is shown in equation 3.11:

$$[Sb(Cit)_2]^{3-} \leftrightarrow 2H^+ + [Sb(H_{-1}Cit)_2]^{5-} \qquad pk_{a2} \sim 3 \qquad \text{Eq. 3.11}$$

Once the deprotonation reaches 5-, the concentration of $[Sb(H_{-1}Cit)_2]^{5-}$ cannot be sustained and there is a separate equilibria started with an antimony citrate hydroxide:

$$[Sb(H_{-1}Cit)_2]^{5-} + 3OH \leftrightarrow Cit^{3-} + [Sb(OH)_3(H_{-1}H_3Cit)]^- \qquad pk_{a3} \sim 4 \qquad \text{Eq. 3.12}$$

Further deprotonation and the hydrolysis of antimony starts occurring with a set of steps as shown in equation 3.13:

$$[Sb(H_{-1}Cit)_2]^{5-} \leftrightarrow [Sb(OH)_3(H_{-1}H_3Cit)] \leftrightarrow Sb(OH)_x^{n+} \leftrightarrow Sb(OH)_3 \leftrightarrow Sb_2O_3 \qquad \text{Eq. 3.13}$$

The citrate is fully deprotonated, the pH spikes and Antimony precipitates.

Potentiometric titrations are a very useful technique from which quantitative information about the species in solution can be gleaned. In the future, the previous experiments should be done with lower concentrations of analytes. The concentration should be about one tenth of what they were here, in order for the ionic strength to be properly held constant with the 0.1 M KNO_3. In addition, it would be easier to calculate how the equivalence point changes if the concentration of antimony were held constant

and the citric acid concentration was changed. In the future, further experiments should be done to elucidate the quantitative make up of the solution.

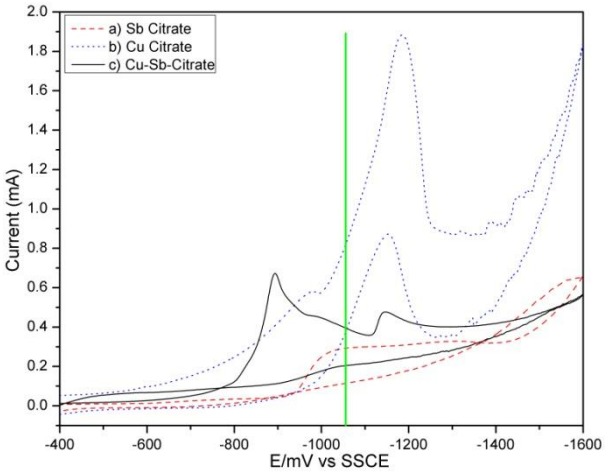

Figure 3.25. Overlay of cyclic voltammograms of different components in the deposition of Cu_2Sb solution. a) 0.025 M Sb_2O_3 in 0.4 M citric acid b) 0.05 M $Cu(NO_3)_2$ in 0.4 M citric acid, and c) 0.08 M $Cu(NO_3)_2$ and 0.025 M Sb_2O_3 in 0.4 M citric acid all at pH 6. Done at 100 mV/s on a 2.01 mm^2 platinum working electrode

From studying the solution chemistry of our system through ESI-MS, we have gained a much better idea of what species are in each solution attributing to the deposition of Cu_2Sb. We can apply this knowledge to better understand the electrochemistry of this system, which is already well studied.[3] The CVs of the individual solutions at different pH values are shown in Appendix 3.6 through Appendix 3.9. The area of interest for the deposition solution is the area of the CVs where the reduction to the Cu_2Sb occurs, between -400 and -1600 mV. An overlay of the copper citrate solution, antimony citrate solution, and deposition solution is shown in Figure 3.25. The antimony citrate CV (Figure 3.25a) appears to show the reduction of two or more peaks. The first is from the proposed species identified in the ESI-MS as $[Sb(HCit)_2]^-$, and the second is the species identified as $[Sb_2(HCit)(Cit)]^-$. Figure 3.26b shows two reduction peaks for copper citrate. The large peak is presumably $[Cu_2(_{H-1}Cit)_2]^{4-}$, while the smaller shoulder on the more positive side of this peak is the second

most abundant species, $[Cu_2(Cit)(_{H-1}Cit)]^{3-}$. Electrodeposition data in the literature suggest that the $[Cu_2(Cit)(_{H-1}Cit)]^{3-}$ species is responsible for copper deposition, and that the more abundant $[Cu_2(_{H-1}Cit)_2]^{4-}$) species is not able to facilitate copper deposition.[56] It is difficult to assign species to the reductions in the Cu-Sb-Citrate solution without more resolution, but based on ESI-MS results it can be hypothesized that one of the peaks is for the reduction of [CuSb(HCit)(Cit)].

To further understand how the concentration of antimony affects the electrochemistry of the system, CVs were collected for the solutions in Table 3.4. The ratio of antimony was varied, but the copper citrate was held constant. An overlay of the CVs of antimony citrate at pH 6 and 75 mV/sec is shown in Figure 3.26A, and an overlay of copper antimony citrate at pH 6 is shown in Figure 3.26B (Full CVs shown in Appendix 3.10). Looking specifically at the reductive portion of the curve, the current associated with each peak and the number of peaks vary from one sample to the next. The breakdown of what these peaks are likely to be is outlined below.

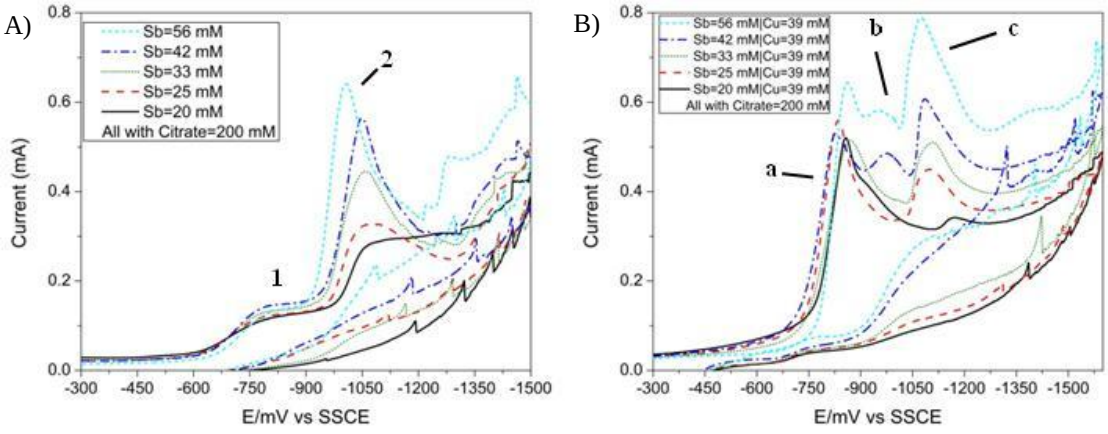

Figure 3.26. Cyclic Voltammograms of different amounts of antimony in citric acid compared to the same amounts of antimony in copper citrate solution at pH 6 as described by Table 3.4. (A) Different concentrations of Sb_2O_3 in 200 mM citric acid (B) Different concentrations of Sb_2O_3 in 39 mM $Cu(NO_3)_2$ in 200 mM citric acid all at pH 6. Done at 75 mV/s on a 2.01 mm^2 platinum working electrode.

Figure 3.26A shows two or more main reduction peaks in the antimony citrate The Peak 1 maybe from the proposed species identified in the ESI-MS $[Sb_2(HCit)(Cit)]^-$ since it was found to be at lower abundance. Peak 2 is the reduction of the antimony citrate species in the solution that leads to the electrodeposition of antimony metal. As shown in Figure 3.26A, peak 2 in the antimony citrate solution increases with increased antimony concentration. Peak 2 can be described by equation 3.14, in which the species identified is based off the ESI-MS results (keeping in mind that it may be further deprotonated):

$$[Sb(HCit)_2]^- + 2H_2O + 3e^- \rightarrow Sb^0 + 2Cit^{3-} + 2H_3O^+ \qquad \text{Eq. 3.14}$$

Examining Figure 3.26B, the antimony peak appears to shift to more negative potentials. It is labeled as peak (c) and is roughly the same size as peak 2 in antimony citrate solution. Peak (a) is the copper citrate species that gets reduced, which can be described by equation 3.15:

$$2[Cu_2Cit_2H_{-1}]^{3-} + 4e^- + 2H_2O \rightarrow 4Cu + 4Cit^{3-} + 2H_3O^+ \qquad \text{Eq. 3.15}$$

The current should decrease in Peak (a) with increased antimony concentration, since it was shown with ESI-MS that antimony concentration goes down with increased pH. This could be due to a gradient being established based on diffusion to the electrode surface, in which the overall concentration at the electrode may not change with increasing antimony concentration. A gradient being established may mean that only a certain amount of species can be electrodeposited before initialization of the second reaction at peak (b). The peak height of the current is linear with respect to antimony concentration with peak (b) and peak (c). Peak (b) is present at low scan rates and disappears at higher scan rates. It has been shown that, during the Cu_2Sb deposition,

pulse times need to be above two seconds in order for a gradient to be established to allow one species to deposit before the other.[57]

If the solution is stirred, copper-rich forms of copper antimonide are deposited instead of Cu_2Sb. (See Chapter One on the electrodeposition of copper antimonide for more information.) Cyclic voltammetry is a good technique to bridge the gap between solution analysis and electrochemical processes going on in solution. The behavior of these solutions in CV is quite interesting, and should be explored further. A rotating disk electrode experiment would be interesting to see how rotation of the electrode at various rates might change the results based on convection of the solution. In addition, a microelectrode could be used to run the CVs at even slower scan rates. A different electrode, such as a glassy carbon working electrode, will reduce the amount of hydrogen evolution by shifting it out to more negative potentials. In this way, the noise that is seen at potentials past -1.1V may be cleaned up.

This preliminary data for heterometallic species ([CuSb(HCit)(Cit)]), and the enlightenment that the antimony species originally thought to deposit $[SbCitH_{-1}]^-$ is not even present in our deposition solution, clearly shows that the solution is quite a bit more complicated than originally thought. Therefore, the reaction scheme needs to be updated from the original co-depositon reaction scheme[3] to incorporate the species now thought to be present based on the ESI-MS analysis. There are two reactions that can be proposed based on the speciation data gathered and the electrochemistry studies. The first is the simple co-deposition reaction, shown in equation 3.16, which was proposed in a previous paper, but has been modified with species identified in the ESI-MS spectra.[3]

The second is a more complicated reaction scheme involving the heterometallic species identified in the ESI-MS is shown in equation 3.17.

$$[Cu_2Cit_2H_{-1}]^{3-} + 2[CuSb(HCit)(Cit)]^{0} + H_2O + 14e^- \rightarrow 2Cu_2Sb + 6Cit^{3-} + H_3O^+ \quad \text{Eq. 3.16}$$

$$[Cu_2Cit_2H_{-1}]^{3-} + [Sb(HCit)_2]^- + H_2O + 7e^- \rightarrow Cu_2Sb + 4Cit^{3-} + H_3O^+ \quad \text{Eq. 3.17}$$

The more negative the potential in the electrodeposition of Cu_2Sb, the more antimony-rich the product will become.[3] The more antimony-rich product can be described by the previous reaction (in equation 3.14) where antimony citrate is reduced to antimony metal.

3.4. Conclusion

ESI-MS has been demonstrated to be a viable technique for studying the metal-ligand complexes in solution through the study of citric acid, copper citrate, antimony citrate, and copper antimony citrate solutions. The heterometallic species [CuSb(HCit)(Cit)], previously only reported in solids that had been crystallized out of solution, was discovered in solution through ESI-MS. It is hypothesized and shown that, through a simple balanced reaction, the heterometallic species could be the reason for the single deposition of Cu_2Sb in our system. In addition, based on the information gained by ESI-MS, the $[SbCitH_{-1}]^-$ species originally thought to be responsible for the deposition of antimony metal was shown to be present only in very small quantities of <1%. Instead, a new $[(H_{-1}Cit)(Cit)Sb_2]^-$ species is hypothesized to be responsible for the deposition of antimony-rich Cu_2Sb at more negative potentials. These results lead us closer to being able to predict what materials could be electrodeposited based on the speciation of complexes in solution. This includes knowledge of what ligands, what pH levels, and what concentrations would be best to produce the desired direct deposition of a given intermetallic.

3.5. References

1. Fransson, L. M. L.; Vaughey, J. T.; Benedek, R.; Edstrom, K.; Thomas, J. O.; Thackeray, M. M., Phase transitions in lithiated Cu_2Sb anodes for lithium batteries: an in situ X-ray diffraction study. *Electrochemistry Communications* **2001,** *3* (7), 317-323.

2. Fransson, L. M. L.; Vaughey, J. T.; Edstrom, K.; Thackeray, M. M., Structural transformations in intermetallic electrodes for lithium batteries - An in situ x-ray diffraction study of lithiated MnSb and Mn_2Sb. *Journal of the Electrochemical Society* **2003,** *150* (1), A86-A91.

3. Mosby, J. M.; Prieto, A. L., Direct Electrodeposition of Cu_2Sb for Lithium-Ion Battery Anodes. *J. Am. Chem. Soc.* **2008,** *130* (32), 10656-10661.

4. Roy, W. M. a. S., Electrochemical Characterization of copper deposition from citrate solution. *Proceedings of Electrochemical Society* **2000,** *99* (33), 61-70.

5. Amico, P.; Daniele, P. G.; Ostacoli, G.; Arena, G.; Rizzarelli, E.; Sammartano, S., Mixed Metal-Complexes in Solution .2. Potentiometric Study of Heterobinuclear Metal(Ii)-Citrate Complexes in Aqueous-Solution. *Inorganica Chimica Acta-Letters* **1980,** *44* (4), L219-L221.

6. Melnik, M.; Ondrejovic, G.; Kabesova, M.; Baloghovam, Z.; Broskovicova, A., *Heterometallic Coordination Copper (II) Compounds: Classification and Analysis of Crystallographic and Structural Data*. Nova Publishers: 1999.

7. Daniele, P. G.; Ostacoli, G.; Zerbinati, O.; Sammartano, S.; Derobertis, A., Mixed Metal-Complexes in Solution - Thermodynamic and Spectrophotometric Study of Copper(II)-Citrate Heterobinuclear Complexes with Nickel(II), Zinc(II) or Cadmium(II) in Aqueous-Solution. *Transit. Met. Chem.* **1988,** *13* (2), 87-91.

8. Rode, S.; Henninot, C.; Matlos, M., Complexation chemistry in nickel and copper-nickel alloy plating from citrate baths. *Journal of the Electrochemical Society* **2005,** *152* (4), C248-C254.

9. Smith, G.; Sagatys, D. S.; Bott, R. C.; Lynch, D. E.; Kennard, C. H. L., Crystallographic Evidence for the Presence of Both (2-) Citrate and (3-) Citrate Species in a Mixed-Metal Complex, $[CuSb(C_6H_6O_7^{2-})(C_6H_5O_7^{3-})(H_2O)_2]\bullet 2.5H_2O$. *Polyhedron* **1992,** *11* (6), 631-634.

10. Gautier-Luneau, I.; Merle, C.; Phanon, D.; Lebrun, C.; Biaso, F.; Serratrice, G.; Pierre, J.-L., New Trends in the Chemistry of Iron(III) Citrate Complexes: Correlations between X-ray Structures and Solution Species Probed by Electrospray Mass Spectrometry and Kinetics of Iron Uptake from Citrate by Iron Chelators. *Chemistry - A European Journal* **2005,** *11* (7), 2207-2219.

11. Lakatos, A.; Kiss, T.; Bertani, R.; Venzo, A.; Di Marco, V. B., Complexes of Al(III) with D-gluconic acid. *Polyhedron* **2008,** *27* (1), 118-124.

12. Somogyi, Á.; Pasilis, S. P.; Pemberton, J. E., Electrospray ionization of uranyl-citrate complexes: Adduct formation and ion-molecule reactions in 3D ion trap and ion cyclotron resonance trapping instruments. *International Journal of Mass Spectrometry* **2007,** *265* (2-3), 281-294.

13. Rellán-Álvarez, R.; Abadía, J.; Álvarez-Fernández, A., Formation of metal-nicotianamine complexes as affected by pH, ligand exchange with citrate and metal exchange. A study by electrospray ionization time-of-flight mass spectrometry. *Rapid Communications in Mass Spectrometry* **2008,** *22* (10), 1553-1562.

14. Di Marco, V. B.; Bombi, G. G., Electrospray mass spectrometry (ESI-MS) in the study of metal-ligand solution equilibria. *Mass Spectrometry Reviews* **2006,** *25* (3), 347-379.

15. Di Marco, V. B.; Bombi, G. G.; Ranaldo, M.; Traldi, P., Metal-ligand solution equilibria studied by electrospray ionization mass spectrometry: correlation between ion intensity and acid-base equilibria in solution. *Rapid Communications in Mass Spectrometry* **2007,** *21* (23), 3825-3832.

16. Di Marco, V. B.; Bombi, G. G.; Zambon, S.; Traidi, P., Metal-ligand solution equilibria studied by electrospray ionization mass spectrometry: effect of instrumental parameters. *Journal of Mass Spectrometry* **2009,** *44* (1), 120-127.

17. Dole, M.; Mack, L. L.; Hines, R. L., Molecular Beams of Macroions. *J. Chem. Phys.* **1968,** *49* (5), 2240-2249.

18. Schmelzeisenredeker, G.; Butfering, L.; Rollgen, F. W., Desolvation of Ions and Molecules in Thermospray Mass-Spectrometry. *Int. J. Mass Spectrom. Ion Process.* **1989,** *90* (2), 139-150.

19. Iribarne, J. V.; Thomson, B. A., Evaporation of Small Ions from Charged Droplets. *J. Chem. Phys.* **1976,** *64* (6), 2287-2294.

20. Thomson, B. A.; Iribarne, J. V., Field-Induced Ion Evaporation from Liquid Surfaces at Atmospheric-Pressure. *J. Chem. Phys.* **1979,** *71* (11), 4451-4463.

21. Kebarle, P.; Ho, Y., On the Mechanism of Electrospray Mass Spectrometry. In *Electrospray Ionization Mass Spectrometry: Fundamentals, Instrumentation, and Applications*, Cole, R. B., Ed. John Wiley and Sons, Inc: New York, 1997; pp 3-63.

22. Blades, A. T.; Ikonomou, M. G.; Kebarle, P., Mechanism of electrospray mass spectrometry. Electrospray as an electrolysis cell. *Anal. Chem.* **1991,** *63* (19), 2109-2114.

23. Ikonomou, M. G.; Blades, A. T.; Kebarle, P., Electrospray-ion spray: a comparison of mechanisms and performance. *Anal. Chem.* **1991,** *63* (18), 1989-1998.

24. Marco, V. B. D.; Raveane, L.; Dean, A.; Traldi, P., Perturbations produced by electrospray ionization mass spectrometry in the speciation of aluminium(III)/1,6-dimethyl-4-hydroxy-3-pyridinecarboxylate aqueous solutions. *Rapid Communications in Mass Spectrometry* **2010,** *24* (7), 868-874.

25. McNaught, A. D.; Wilkinson, A., *IUPAC. Compendium of Chemical Terminology (the "Gold Book")*. 2nd ed.; Blackwell Scientific Publications Oxford, 1997.

26. IPCS Citric Acid. http://www.cdc.gov/niosh/ipcsneng/neng0855.html.

27. ThermoFinnigan, T. I., LCQ Operator Course - Introductory Lecture. Thermo Electron Corporation, San Jose, CA: 2003.

28. Rode, S.; Henninot, C.; Vallieres, C. C.; Matlosz, M., Complexation chemistry in copper plating from citrate baths. *Journal of the Electrochemical Society* **2004,** *151* (6), C405-C411.

29. Skoog, D. A.; Holler, F. J.; Nieman, T. A., *Principles of Instrumental Analysis* 5th ed.; Saunders College Publishing: 1998.

30. Holstad, A., Numerical solution of nonlinear equations in chemical speciation calculations. *Computational Geosciences* **1999,** *3* (3), 229-257.

31. Benjamin, M. M., *Water Chemistry*. The McGraw-Hill Companies, Inc: 2002.

32. Das, R.; Pani, S., Citrate Complex of Trivalent Antimony. *Jour. Indian Chem. Soc.* **1955,** *32* (8), 537-543.

33. Hansen, H. R.; Pergantis, S. A., Detection of antimony species in citrus juices and drinking water stored in PET containers. *J. Anal. At. Spectrom.* **2006,** *21* (8), 731-733.

34. Hansen, H. R.; Pergantis, S. A., Identification of Sb(V) complexes in biological and food matrixes and their stibine formation efficiency during hydride generation with ICPMS detection. *Anal. Chem.* **2007,** *79* (14), 5304-5311.

35. Zheng, J.; Iijima, A.; Furuta, N., Complexation effect of antimony compounds with citric acid and its application to the speciation of antimony(III) and antimony(V) using HPLC-ICP-MS. *J. Anal. At. Spectrom.* **2001,** *16* (8), 812-818.

36. Tella, M.; Pokrovski, G. S., Antimony(III) complexing with O-bearing organic ligands in aqueous solution: An X-ray absorption fine structure spectroscopy and solubility study. *Geochimica et Cosmochimica Acta* **2009,** *73* (2), 268-290.

37. Palenik, R. C.; Abboud, K. A.; Palenik, G. J., Bond valence sums and structural studies of antimony complexes containing Sb bonded only to O ligands. *Inorganica Chimica Acta* **2005,** *358* (4), 1034-1040.

38. Mazali, I. O.; Las, W. C.; Cilense, M., Synthesis and characterization of antimony tartrate for ceramic precursors. *J. Mater. Synth. Process* **1999,** *7* (6), 387-391.

39. Smith, G.; Sagatys, D. S.; Bott, R. C.; Lynch, D. E.; Kennard, C. H. L., Group 15 complexes with carboxylic acids--VI. Preparation and crystal structures of potassium antimony(III) citrate, $\{[K_2Sb_4(citrate)_8(H_2O)_2]\}$ and lithium antimony(III) citrate, $\{[LiSb(citrate)_2(H_2O)]\cdot 2H_2O\}$. *Polyhedron* **1993,** *12* (12), 1491-1497.

40. Filella, M.; May, P. M., Computer simulation of the low-molecular-weight inorganic species distribution of antimony(III) and antimony(V) in natural waters. *Geochimica Et Cosmochimica Acta* **2003,** *67* (21), 4013-4031.

41. Filella, M.; May, P. M., Critical appraisal of available thermodynamic data for the complexation of antimony(III) and antimony(V) by low molecular mass organic ligands. *J. Environ. Monit.* **2005,** *7* (12), 1226-1237.

42. Filella, M.; Belzile, N.; Chen, Y. W., Antimony in the environment: a review focused on natural waters II. Relevant solution chemistry. *Earth-Sci. Rev.* **2002,** *59* (1-4), 265-285.

43. Miessler, G. L.; Tarr, D. A., *Inorganic Chemistry*. Third ed.; Pearson Prentice Hall: Upper Saddle River, New Jersey, 2004.

44. Mastropaolo, D.; Powers, D. A.; Potenza, J. A.; Schugar, H. J., Crystal structure and magnetic properties of copper citrate dihydrate, $Cu_2C_6H_4O_7\cdot 2H_2O$. *Inorg. Chem.* **1976,** *15* (6), 1444-1449.

45. Billo, E. J., Copper(II) Chromophores and Rule of Average Environment. *Inorganic & Nuclear Chemistry Letters* **1974,** *10* (8), 613-617.

46. Prenesti, E.; Daniele, P. G.; Prencipe, M.; Ostacoli, G., Spectrum-structure correlation for visible absorption spectra of copper(II) complexes in aqueous solution. *Polyhedron* **1999,** *18* (25), 3233-3241.

47. Prenesti, E.; Daniele, P. G.; Toso, S., Visible spectrophotometric determination of metal ions: the influence of structure on molar absorptivity value of copper(II) complexes in aqueous solution. *Analytica Chimica Acta* **2002,** *459* (2), 323-336.

48. Tzec, F. I. L.; Oskam, G. In *Electrodeposition of Copper in Trenches from a Citrate Plating Bath*, ECS Meeting Abstracts, 2009; p 2781.

49. Zaki, M. T. M.; Alqasmi, R., Spectrophotometric Determination of Copper(Ii) as Citrate or Edta Complex. *Fresenius Zeitschrift Fur Analytische Chemie* **1981,** *306* (5), 400-400.

50. Boas, J. F.; Dunhill, R. H.; Pilbrow, J. R.; Srivasta.Rc; Smith, T. D., Electron Spin Resonance Studies of Copper(II) Hydroxy-Carboxylic Acid Chelates in Aqueous and Non-Aqueous Solutions. *Journal of the Chemical Society a -Inorganic Physical Theoretical* **1969,** (1), 94-&.

51. Petitram.Mm; Khalil, I., Study of Mixed Bimetallic Complexes .1. Determination of Stability-Constants of Citric-Acid and Copper Citrates. *Bulletin De La Societe Chimique De France Partie I-Physicochimie Des Systemes Liquides Electrochimie Catalyse Genie Chimique* **1974,** (7-8), 1255-1258.

52. Daniele, P. G.; Ostacoli, G.; Rigano, C.; Sammartano, S., Ionic-Strength Dependence of Formation-Constants .4. Potentiometric Study of the System Cu^{2+}-Ni^{2+}-Citrate. *Transit. Met. Chem.* **1984,** *9* (10), 385-390.

53. Lide, D. R., *CRC Handbook of Chemistry and Physics*. 84th ed.; CRC Press: New York, 2003.

54. Silva, A. M. N.; Kong, X. L.; Hider, R. C., Determination of the pKa value of the hydroxyl group in the alpha-hydroxycarboxylates citrate, malate and lactate by 13C NMR: implications for metal coordination in biological systems. *Biometals* **2009,** *22* (5), 771-778.

55. Silberberg, M. S., *Chemistry: The Molecular Nature of Matter and Change* Fourth Edition ed.; McGraw Hill Higher Education: 2006.

56. Uksene, V.; Survila, A.; Zukauskaite, A., The electroreduction mechanism of copper(II) citrate complexes. *Russ. J. Electrochem.* **1996,** *32* (8), 884-888.

57. Mosby, J. M.; Johnson, D. C.; Prieto, A. L., Evidence of Induced Underpotential Deposition of Crystalline Copper Antimonide via Instantaneous Nucleation. *Journal of the Electrochemical Society* **2010,** *157* (6), E99-E105.

4. Chapter 4 – Application of the Cu_2Sb System for the Electrodeposition of Other Intermetallic Antimonides

4.1. Introduction

Intermetallic antimonides have a wide range of applications because of their interesting bonding characteristics.[1-2] Some of these applications include: thermoelectric devices,[3] infrared detection,[4] magnetoresistive sensing,[5] and possible replacements for graphite anodes in lithium ion batteries.[6-8] Recently Mosby *et al.* presented a method to produce highly crystalline films of the intermetallic Cu_2Sb at room temperature, in aqueous solutions, by direct electrodeposition.[9] This is a highly desirable technique since it is much more efficient than previous preparation methods such as: classical solid state reactions, chemical reduction from solution, ball milling, or pulsed laser deposition techniques.[8, 10-17] Electrodeposition also offers the benefit of the capability to deposit on a variety of surfaces that can serve in a wide range of applications. The highly crystalline films of Cu_2Sb are unusual for intermetallics, as this method typically yields amorphous films. It would be advantageous to study the system that was used for the electrodeposition of Cu_2Sb to learn why highly crystalline films deposit, in order to be able to apply it to other intermetallics of interest. For example, it would be of particular interest to substitute copper for other first row transition metals in order to electrodeposit a wide range of transition metal intermetallic antimonides.

The choice of an aqueous solution limits the choice of transition metals and complexing agents that are usually used to prevent hydrolysis of the metal at non acidic

pH values. The first three first row transition metals (scandium, titanium, and vanadium) are difficult to electrodeposit out of aqueous solution due to their fast oxidation in water. Since they have so few d-electrons they form strong covalent bonds with oxygen making it difficult to reduce the metal.[18] It is, however, possible to electrodeposit the transition metals chromium through zinc out of aqueous solutions. Preliminary work on ZnSb and MnSb has shown that it is possible to co-deposit the two metals using different electrolytes, but not in crystalline form.[19] Consequently, it has been shown that by changing the electrolyte to malic acid the product switches from Cu_2Sb to $Cu_{3.3}Sb$.[20] Therefore, to limit the vast multitude of electrolytes able to complex with these transition metals citric acid was chosen since it is known to complex with a variety of different metals and matches the original Cu_2Sb system.

The electrodeposition of Cu_2Sb films has been shown to be a sensitive system, in which the film quality can vary with many factors. These factors are mainly attributed to the experimental setup (Chapter 1), which can be held constant, and the solution chemistry (Chapter 3) that can be varied a number of different ways. Based on the results presented in Chapter 3, solution chemistry plays an important role in the electrodeposition of Cu_2Sb. The solution was characterized using ESI-MS, UV-Vis, titrations, and based on the results two different reaction schemes were proposed that could lead to the Cu_2Sb product:

$$[Cu_2Cit_2H_{-1}]^{3-} + 2[CuSb(HCit)(Cit)]^{0} + H_2O + 14e^- \rightarrow 2Cu_2Sb + 6Cit^{3-} + H_3O^+ \quad \text{Eq. 4.1}$$

$$[Cu_2Cit_2H_{-1}]^{3-} + [Sb(HCit)_2]^- + H_2O + 7e^- \rightarrow Cu_2Sb + 4Cit^{3-} + H_3O^+ \quad \text{Eq. 4.2}$$

These two equations can be identified by the reduction of a copper citrate species with a heterometallic species (equation 4.1) and the reduction of just the single metallic citrate species (equation 4.2). If the deposition proceeds by one of the above reactions then a

simple metal substitution should make it possible to deposit different intermetallic antimonides.

Citric acid, as mentioned in Chapter 3, forms a variety of stable complexes. Some of those complexes can be reduced to deposit the metal and some of them cannot. For example, electrodeposition data in the literature suggest that the $[Cu_2(Cit)(_{H-1}Cit)\ ]^{3-}$ species is responsible for copper deposition, but the more abundant $[Cu_2(_{H-1}Cit)_2]^{4-}$) species is not able to facilitate copper deposition.[21] In the literature, it was shown that a chromium metal electrodeposition from the chromium citrate complex is not possible and for this reason it was eliminated from this current study.[22] Manganese and zinc were not examined in this study since Noblitt *et al.* is currently studying these materials and has shown that they co-deposit at a single potential.[19] Following manganese in the periodic table is iron, which forms stable complexes that can be electrodeposited directly out of an aqueous citric acid bath.[23-24] Cobalt is able to be reduced from the citric acid complex, but two different intermetallic cobalt antimonies, $CoSb_3$ and $CoSb_2$, have already been electrodeposited out of aqueous citric acid solutions.[25-26] Finally, nickel has been well studied in the literature due to the abundant nickel copper alloys used for their wide range of corrosion stability. Rode *et al.* along with their speciation study on copper citrate complexes, followed up with a similar study on nickel citrate complexes.[27] It is easy to electrodeposit nickel out of a citrate bath as long as there is not a large excess of citrate present, since the species $[Ni(Cit)_2]^{4-}$ becomes predominant and impedes the deposition of the metal.[28] However, it has not been shown that nickel could be used to electrodeposit nickel antimonides at a single potential.

Using the above knowledge as a spring board, the metals iron and nickel were chosen for the electrodeposition of crystalline intermetallic antimonide out of aqueous solution. Intermetallic antimonides with these metals have been shown as a possible replacement anode for lithium ion batteries[29-32] as well as thermoelectric materials.[33-35] In addition to iron and nickel in this study, the electrodeposition of different copper rich antimonides were also studied, since there has been evidence of these present in some of the depositions of copper antimonide. The following copper rich phases of copper antimonide were targeted: Cu_3Sb, $Cu_{10}Sb_3$, $Cu_{11}Sb_3$, Cu_4Sb, and $Cu_{0.95}Sb_{0.05}$.

4.2. Experimental

The electrodeposition solution was prepared using units of molality (m) rather than molarity (M), (added a specified amount of solvent before the addition of the solutes). The following were combined and dissolved with the aid of mechanical stirring for 48 hours: doubly deionized 18Ω water (Milli-Q Plus System, 4-bowl, Millipore) 0.025 m antimony (III) oxide (Sb_2O_3 nanopowder, <250 nm particle size (BET), ≥99.9% trace metals basis, Sigma Aldrich) and 0.4 m anhydrous citric acid (denoted H_3Cit, puriss. p.a., 99.5+%, ACS reagent, Sigma Aldrich). After the Sb_2O_3 dissolved, different concentrations copper (II) nitrate trihydrate ($Cu(NO_3)_2•3H_2O$, purum. p.a., 98.0-103% RT, Sigma Aldrich) were added (specific concentrations are in the results section Tables 4.1 and 4.2). Solutions changed from clear to light blue following the addition of Cu. The pH probe (Thermo Orion 9157 BNMD Orion triode 3-in-1 pH electrode equipped with auto temperature compensation) was calibrated with buffers of pH 1.68 (Orion potassium tetraoxalate dehydrate buffer), 4.00 (Fisher potassium biphthalate buffer), 7.00 (potassium phosphate monobasic-sodium hydroxide buffer), and 10.00 (potassium

carbonate-potassium borate-potassium hydroxide buffer) using a Thermo Orion 3 star series pH meter. The solution was brought to pH 6.0 with saturated KOH, at which time the solution became much darker blue.

Nickel antimony citrate solutions were prepared in the same way as described above, only substituting 0.08 m nickel (II) nitrate hexahydrate ($Ni(NO_3)_2 \cdot 6H_2O$ (Mallinckrodt ACS grade) for copper (II) nitrate trihydrate. The solution was a light green color. Once the pH was raised to a pH of 6, the solution was a dark green with a slight hint of teal.

Iron antimony citrate solutions were prepared in the same way as described above, only substituting 0.05 m iron (III) nitrate nonahydrate ($Fe(NO_3)_3 \cdot 9H_2O$ (Fisher ACS grade) for copper (II) nitrate trihydrate. The iron citrate and iron antimony citrate solution were both a light yellow color at the initial pH. When the iron citrate solution was brought to pH 6, a brownish precipitate formed, but when antimony citrate was in solution the pH could be raised to pH 6 without any precipitate forming. This indicates that an iron citrate solid formed (in the iron citrate solution) due to the excess citrate or a significant amount of heterometallic Fe-Sb-Cit formed, which would decrease the amount of iron in solution preventing the formation of iron hydroxides at higher pH values.

SEM images were taken with a JEOL JSM-6500F equipped with an energy dispersive X-ray spectroscopy (EDS) detector from Thermo Electron. Images were taken at 15 kV. Powder X-ray Diffraction (XRD) data was collected using Cu Kα radiation from a Scintag X-2 Advanced Diffraction X-Ray cabinet system, equipped with a Peltier detector.

Cyclic voltammograms (CVs) and depositions were performed on a CH Instruments Model 660C Potentiostat/Galvanostat or 1232A Potentiostat. CVs were taken in a three electrode set up consisting of the following electrodes: (1) a saturated sodium calomel electrode (SSCE) reference electrode (+0.236 V versus standard hydrogen electrode), (2) a platinum disk electrode (2.01 mm^2) or glassy carbon electrode (7.07 mm^2) working electrode (WE), and (3) platinum wire (diameter 0.5 mm, Aldrich, 99.9% trace metals basis) counter electrode.

Deposition and open circuit potential (OCP) measurements were completed on a Gamry Instruments, Reference 3000, controlled by Gamry Framework version 5.60 software using a three electrode set up consisting of the following electrodes: (1) a saturated sodium calomel electrode (SSCE) reference electrode (+0.236 V versus standard hydrogen electrode), (2) copper working electrode (details described below), and (3) 25 x 25 mm platinum gauze (Aldrich, 52 mesh, 99.9% trace metals basis) counter electrode. Copper foil working electrode (0.25 mm thick, 99.98% metals basis, Sigma Aldrich) was punched out in 5/8 inch circles and mechanically polished to a mirror finish by first attaching the copper to a brass slug with Crystalbond adhesive (509 Amber, Aremco Products). Upon cooling, the copper was mechanically polished (Buehler) with 3 μm followed by 1 μm diamond paste (MetaDi Supreme, Buehler USA) on 8" Microcloth with pressure sensitive adhesive (PSA) (Buehler). The paste was kept wet during the process using MetaDi fluid (extender for diamond abrasive, Buehler). The electrodeposition was carried out at a temperature of 52°C using the jacketed beaker setup shown in Figure 1.9 (Chapter 1).

4.3. Results

4.3.1. Electrodeposition of other Crystalline Copper Antimonide Stoichiometries

The proposed reactions in equations 4.1 and 4.2 would imply that the copper citrate species $[Cu_2Cit_2H_{-1}]^{3-}$ can be reduced to copper metal following equation 4.3:

$$2[Cu_2Cit_2H_{-1}]^{3-} + 4e^- + 2H_2O \rightarrow 4Cu + 4Cit^{3-} + 2H_3O^+ \qquad \text{Eq. 4.3}$$

However, Mosby *et al.* states that copper metal does not deposit under the conditions of the Cu_2Sb deposition unless antimony is present first, where it acts as an activation site for the deposition of copper.[36] On the contrary Tzec *et al.* shows images of copper deposited in trenches from a pH 5.5 bath of citric acid.[37-38] Additionally, Kim *et al.* completed nucleation studies on the electrodeposition of copper onto TiN substrates out of a 1:1 copper sulfate to ammonium citrate bath (0.08 M $CuSO_4 \bullet 5H_2O$ and 0.08 M $(NH_4)_2HC_6H_5O_7$) from pH 1.5 to 7.4.[39-40] To investigate this discrepancy, a solution of just copper citrate was prepared following the original electrodeposition solution conditions (0.38 M citric acid, 0.071 M $Cu(NO_3)_2 \bullet 3H_2O$, pH 6.0).

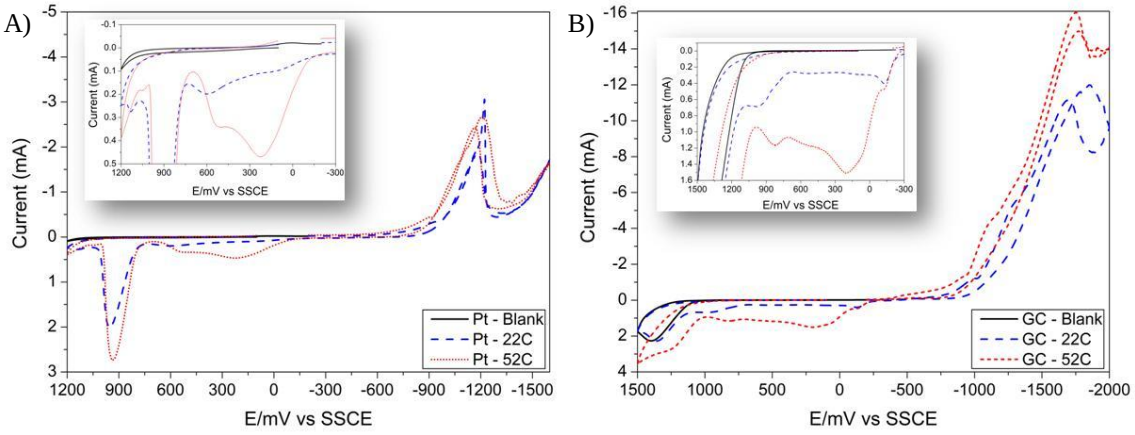

Figure 4.1. Cyclic voltammograms of 0.071 M $Cu(NO_3)_2$ 0.38 M citric at pH 6 on different working electrode surfaces. CVs at two different temperatures (22°C and 52°C) are overlaid with blank (only scanned positive of -300 mV); scan rate of 100 mV/s. Inset is a magnification of the stripping potential region more positive than -300 mV. A) On a 2.01 mm^2 platinum working electrode B) on a 7.07 mm^2 glassy carbon working electrode.

Several CVs were taken over a variety of potential ranges. A CV on a platinum working electrode is shown in Figure 4.1A, while Figure 4.1B shows CVs using a glassy carbon (GC) working electrode. The scan labeled blank is when the potential is just swept positive of the deposition potential of copper (around -200 mV) and brought back to +200 mV. At first glance there is no copper stripping peak at +200 mV, which would seem to indicate that no copper was deposited as mentioned by Mosby *et al.*[9] However, under magnification (Figure 4.1 inset) there is a slight current increase in this region. Figure 4.2B is the same solutions with GC electrode. When the deposition bath temperature is increased 52 °C the stripping peak current increases, which means more copper is able to deposit at higher temperature. It is not a triangular stripping peak, present typical of a metal deposition, which suggests a different process is occurring. Kim *et al.* noted that even when a constant positive potential of 1150 mV was applied the copper film was rarely etched in the citrate solutions and it was suggested that this was due to a protective copper oxide film formed on the copper surface from a local pH increase and the existence of citrate-complex ions when the applied potential is positive.[39] The presence of copper oxide and citrate complexes could explain why there is no sharp stripping peak seen in the CV in Figures 4.1A and B, however it should be noted that some copper was stripped when the potential was held a positive potential in our experiments.

As mentioned earlier, electrodeposition data in the literature suggest that $[Cu_2(Cit)(_{H-1}Cit)\ ]^{3-}$ species is responsible for copper deposition, but the more abundant $[Cu_2(_{H-1}Cit)_2]^{4-}$ species is not able to facilitate copper deposition.[21] It was shown by Rode *et al.* that the copper deposition potential drastically changes in the pH range where

the $[Cu_2(_{H\text{-}1}Cit)_2]^{4-}$ species appears, and it was suggested that the presence of $[Cu_2(_{H\text{-}1}Cit)_2]^{4-}$ species significantly inhibits the copper electroreduction.[41] This would seem to suggest that if *any* amount of $[Cu_2(_{H\text{-}1}Cit)_2]^{4-}$ species is present then the entire electroreduction of copper would not occur. However, this was not the case for the experimental results obtained when electrodepositing on the platinum WE at different potentials. It was observed that copper metal was electrodeposited on the surface of the WE at potentials greater than -200 mV all the way up to -1050 mV at a temperature of 22 or 52 °C. The current profiles of the depositions at 52 °C on the 2.01 mm^2 platinum working electrode are shown in Figure 4.2A. The inset is a magnification of the smaller potentials regions. All of the current profiles greater than -200 mV (-200 mV was not sufficiently negative to reduce copper ion) have the typical looking current transients, but at a potential -1050 mV the current transients change. The current transient for the -1050 mV deposition is different due to the added reduction of the $[Cu_2(_{H\text{-}1}Cit)_2]^{4-}$ species that starts occurring at approximately -1000 mV according to the CV in Figure 4.1A.

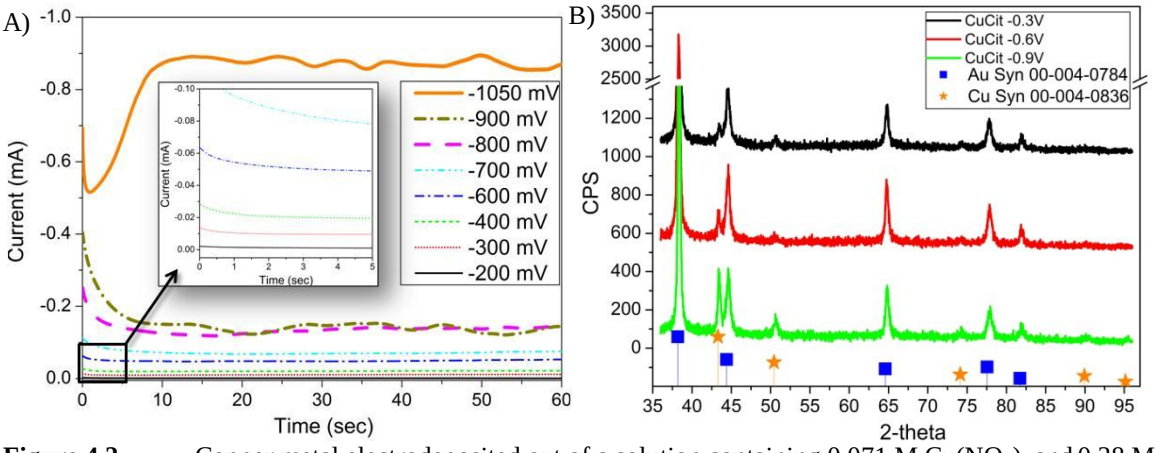

Figure 4.2. Copper metal electrodeposited out of a solution containing 0.071 M $Cu(NO_3)_2$ and 0.38 M citric at pH 6. A) Current transients of depositions onto a 2.01 mm^2 platinum working electrode completed at different potentials versus SSCE reference electrode. Copper deposited on the surface of the WE at potentials greater than -200 mV all the way up to -1050 mV. B) XRD powder patterns of films deposited onto gold substrate at potentials of -300 mV, -600 mV, and -900 mV, which index to copper standard.

As a confirmation three different copper depositions on gold were completed at an elevated bath temp of 52 °C at three different potentials: -0.3, -0.6, and -0.9 V. The XRD powder pattern of the electrodeposited copper on gold is displayed in Figure 4.2B. Crystalline copper was deposited as it indexed to the copper standard (PDF: 00-004-0836). Further confirmation was completed with EDS which indicated copper was deposited. The EDS spectra along with corresponding SEM images of the films deposited are shown in Appendix 4.1.

Since copper *can* be electrodeposited out of copper citrate bath at pH 6, the codeposition reaction of $[Cu_2Cit_2H_{-1}]^{3-}$ and $[Sb(HCit)_2]^-$ in Equation 4.2 seems like the more prominent mechanism for the electrodeposition of Cu_2Sb. This is consistent with the low amount of the heterometallic species $[CuSb(HCit)(Cit)]^0$ in comparison to the copper-citrate and antimony citrate species present in the solution at pH 6, according to ESI-MS results (Chapter 3). Based on the reaction scheme in equation 4.2, it should be possible to adjust the Cu:Sb ratio to produce copper rich films. Once the species deposit, solid state diffusion intermixes the compounds and if the ratio is close enough to a Gibbs free energy location where a stable crystal structure lies, then a crystalline copper antimonide should be deposited as was the case with Cu_2Sb (more information on this topic can be found in section 4.3.4).

Table 4.1. Concentrations of solution ranging from a 1:1 to a 2:1 ratio of copper to antimony used to deposit different alloy ratios of Cu_2Sb.

Targeted Compound	Cu (mM)	Sb (mM)	H_3Cit (mM)	Ratio Cu:Sb	Ratio Cit:Cu
Cu_2Sb	47	47	380	1.00	8.0
Cu_2Sb	59	47	380	1.25	6.4
Cu_2Sb	71	47	379	1.50	5.3
Cu_2Sb	77	47	379	1.64	4.9
Cu_2Sb	83	47	379	1.76	4.6
Cu_2Sb	95	47	378	2.01	4.0

Table 4.2. Concentrations of solution used to deposit antimony metal, copper metal, and copper rich copper antimonide compounds.

Targeted Compound	Cu (mM)	Sb (mM)	H_3Cit (mM)	Ratio Cu:Sb	Ratio Cit:Cu
antimony metal	0	46	732	n/a	n/a
Cu_2Sb	23	46	730	0.50	31.5
Cu_2Sb	46	46	728	1.00	15.7
Cu_2Sb	69	46	727	1.50	10.5
Cu_2Sb	93	46	725	2.03	7.8
Cu_3Sb	137	46	721	3.00	5.3
$Cu_{10}Sb_3$	152	46	720	3.33	4.7
$Cu_{11}Sb_3$	168	46	719	3.67	4.3
Cu_4Sb	182	46	718	4.00	3.9
$Cu_{0.95}Sb_{0.05}$	185	*9.7*	743	19.01	4.0
copper metal	69	0	732	n/a	10.6
copper metal	93	0	732	n/a	7.8
copper metal	182	0	732	n/a	4.0

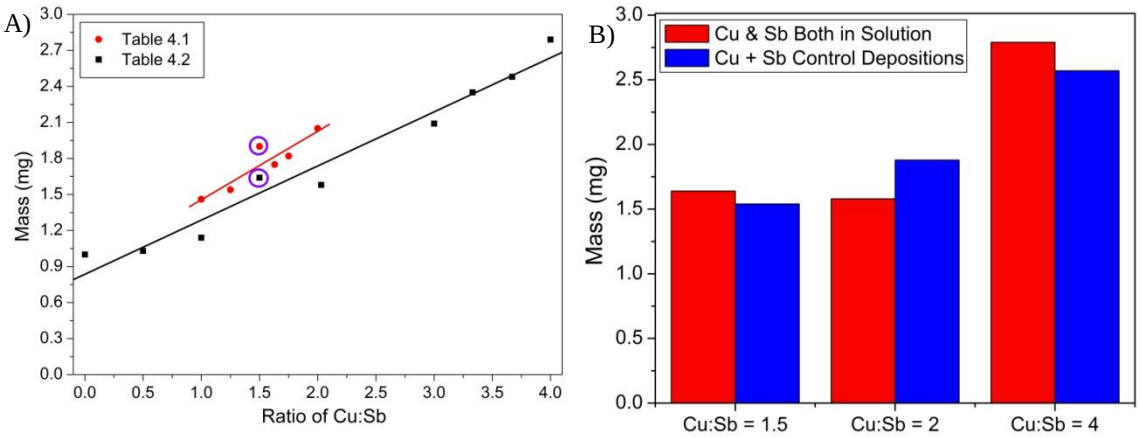

Figure 4.3. Mass Values of films deposited with different ratios of Cu:Sb. A) Mass of the deposited film increase linearly with increasing copper concentration. B) Mass of film of co-deposition of copper and antimony is the same as the mass of antimony and copper deposited separately. Films deposited at -1050 mV at 52° in solutions described in Tables 4.1 and 4.2 brought to pH 6.0 with KOH.

Working off the above hypothesis, several solutions were made by adjusting the amount of copper added, but keeping the amount of antimony and citrate constant. First the concentration of Cu to Sb was adjusted slightly, as shown in Table 4.1. In addition, to obtain a greater difference in the Cu to Sb ratio, the amount of citrate was doubled from the 0.38 M in order to compensate for the extra copper added. If the ratio of copper to citrate increases close to a 2:1 ratio citrate to copper, then the species distribution will

drastically change from the deposition conditions.[41] The concentration of Cu:Sb ratio in the solution was determined by targeting the specific crystal phases: Cu_3Sb, $Cu_{10}Sb_3$, $Cu_{11}Sb_3$, Cu_4Sb, and $Cu_{0.95}Sb_{0.05}$. Furthermore, control solutions were prepared using the same copper content as in the ratios where Cu:Sb = 1.5, 2, and 4, so that the amount of copper deposited could be weighed to further the co-deposition hypothesis. A control solution for the antimony content was also prepared at the same concentration as the set of copper antimony citrate solutions. These solutions with their respective concentrations are shown in Table 4.2.

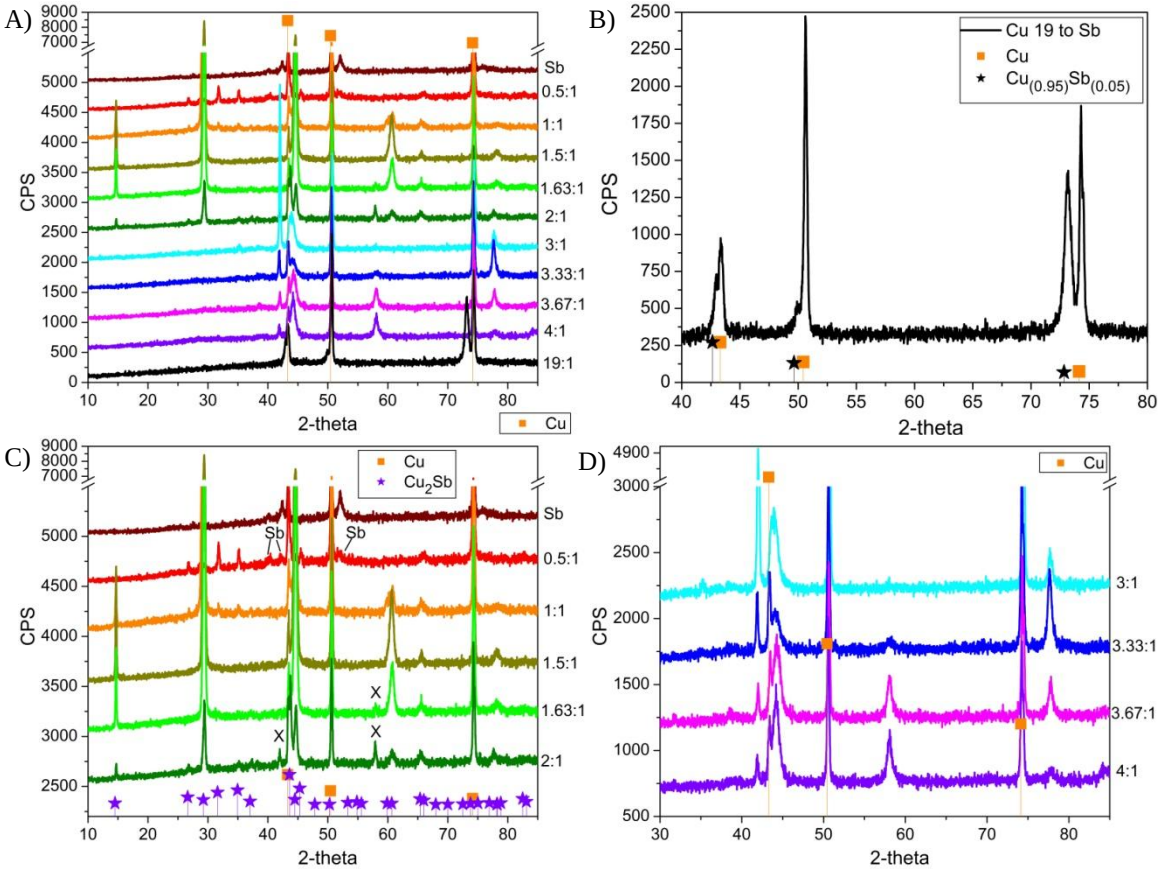

Figure 4.4. XRD powder patterns of films deposited for 10 minutes at -1050 mV at 52° in solutions described in Tables 4.1 and 4.2 brought to pH 6.0 with KOH. A) Overlay of all XRD powder patterns shows different peaks increasing and decreasing based on copper contented in solution. B) XRD powder patter of film deposited in a 19:1 Cu:Sb solution matches $Cu_{0.95}Sb_{0.05}$. C) XRD powder patterns of films deposited in solutions of antimony citrate and different ratios of Cu:Sb ranging from 0.5:1 to 2:1. Only 1:1 and 1.5:1 match Cu2Sb without impurity peaks. D) XRD powder patterns of films deposited in solutions of antimony citrate and different ratios of Cu:Sb ranging from 3:1 to 4:1 index to $Cu_{11}Sb_3$, but also index to other Cu_xSb_y patterns. This may indicate multiple phases of copper antimonide.

The solutions were brought to pH 6 and deposited at -1050 mV for 10 minutes at an elevated temperature of 52 °C using the jacketed beaker setup in Figure 1.9. The films were weighed and a plot of the mass values versus the ratio of Cu:Sb in the solution is shown in Figure 4.3A. The mass of the deposit increases linearly with the increasing concentration of copper. The smaller plot is a more fine tuned ratio between 1:1 and 2:1 copper to antimony from the solutions listed in Table 4.1. Note that the solutions in Table 4.1 were prepared with a slightly larger working electrode area, which is why the entire set of mass values lie above the films deposited from Table 4.2. Interestingly, both plots show an increased mass at the optimum Cu_2Sb deposition bath concentration of 1.5:1. This is most likely because this 1.5:1 ratio is the normal deposition solution concentration, where the conditions have been finely tuned to achieve the best product. Figure 4.3B is a plot of the mass of films co-deposited in the same solution versus the mass of the copper and antimony control depositions added together. Following the co-deposition model, the mass of the films deposited separately match the mass of the films co-deposited out of the same solution.

Powder patterns of selected films from Tables 4.1 and 4.2 were taken and an overlay of all the films is shown in Figure 4.4A. From the overlaid plot it is easy to see how different peaks grew and disappeared based on the concentration of copper in solution, which suggests different crystal phases are being reached from the increased copper concentration deposited in the film. Figure 4.4B is the powder pattern of the highest ratio of 19:1 copper to antimonide. The targeted compound of this 19:1 ratio was $Cu_{0.95}Sb_{0.05}$ and the powder pattern successfully matches the standard pattern (PDF: 01-071-7863) for $Cu_{0.95}Sb_{0.05}$. Figure 4.4C is the control antimony deposition film's powder

pattern and the Cu:Sb ratio solutions between 0.5:1 and 2:1 deposited films. The antimony deposition matches the antimony standard pattern (PDF: 00-035-0732). The different ratios of Cu:Sb solutions between 0.5:1 and 2:1 all mach the Cu_2Sb standard pattern (PDF: 03-065-2815), but only the 1:1 and 1.5:1 ratio do not have any impurity peaks present. The 0.5:1 deposition has impurity peaks due to antimony metal present, labeled as "Sb" in the pattern at 40, 42, and 52° 2-theta. The solutions more copper-rich than the 1.5:1 have impurity peaks labeled "X" at 42 and 58° 2-theta. These peaks labeled "X" match multiple indexes of copper-rich copper antimonide compounds. These peaks at 42 and 58° 2-theta are also found in the powder patterns for the ratios of Cu:Sb solutions between 3:1 and 4:1 shown in Figure 4.4D. The deposition prepared from the 3:1 bath has a very intense sharp peak at 42° 2-theta that decreases with further increase in copper concentration. The peak at 44° 2-theta changes shape, but is relatively constant for all powder patterns. The peak at 58° 2-theta is very small in the 3:1 Cu:Sb deposition, but increases with increasing copper. The peak at 77.5° 2-theta is largest in the 3.33:1 powder pattern and smaller in the other patterns. Finally, the peak at 84° 2-theta is only present in the 3.67:1 and 4:1 powder patterns.

All of the peaks mentioned index to multiple standard powder patterns. The standard for $Cu_{11}Sb_3$ (PDF: 03-065-9660) matches closest to all the peaks present. Furthermore, in the 3.67:1 powder pattern there are additional peaks at 32 and 38° 2-theta that also match the $Cu_{11}Sb_3$ standard. Further evidence for $Cu_{11}Sb_3$ being deposited is that the peaks at 38, 44, 58, and 77.5 are all related and lie along the (02ℓ) direction: (020), (021), (022), and (023). However, an issue arises in that the compounds Cu_3Sb, $Cu_{10}Sb_3$, $Cu_{11}Sb_3$, and Cu_4Sb are also a close match and have related planes at similar 2-

theta. These depositions most likely result in a mixture of the different copper-rich copper antimonide compounds being deposited, based on this observation. The deposition of a combination of these compounds would explain the increase and decrease of the peaks. The sharp peak at 42° 2-theta in the XRD pattern for the 3:1 ratio could be indexed to Cu_3Sb, whereas the broad peak at 84° 2-theta in the XRD pattern for the 4:1 ratio is consistent with Cu_4Sb. These results further suggest that multiple phases of copper-rich copper antimonide compounds being electrodeposited dictated by the concentration in solution.

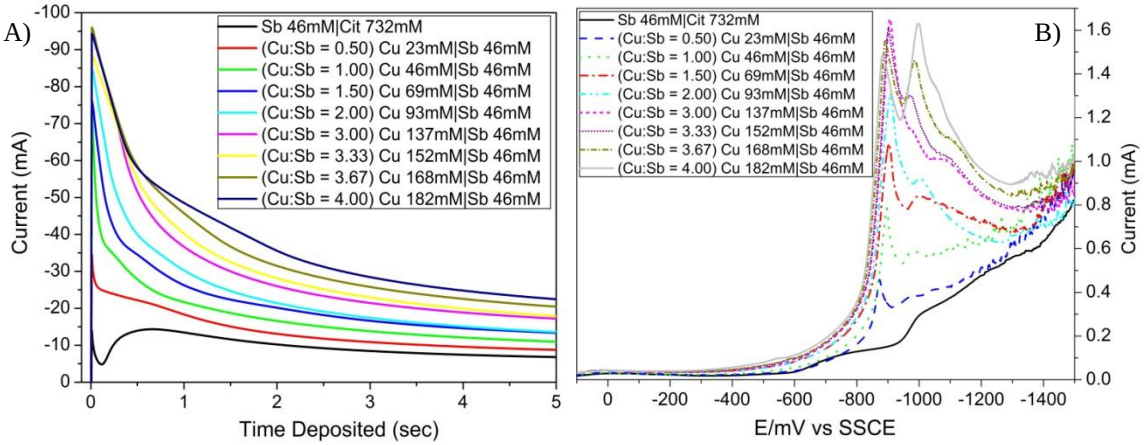

Figure 4.5. Current transients and CVs of a 0.023 M Sb_2O_3 in 0.38 M citric acid (pH 6) with varying amounts of $Cu(NO_3)_2$ added as described in Table 4.2. (A) Current transients during the deposition of solutions described in Table 4.2. Current increases with increasing copper concentration. B) Cyclic voltammograms of labeled solutions focused on reduction of the species to the metals done at 75 mV/s on a 2.01 mm^2 platinum working electrode.

Figure 4.5A shows the current transients of the depositions completed with the different ratios of copper to antimony and Figure 4.5B displays the reduction portion of the cyclic voltammograms (CVs) taken on these same solutions (the full CV taken of the solutions can be found in Appendix 4.2). Both the current transients and CVs of the solutions follow what has been proposed as a co-deposition model in equation 4.2. In Figure 4.5A the current transients show more current with increasing copper content as expected since there is more copper present to reduce at the electrode, but instead of just

decaying to steady state, between 0.5 seconds and 2 seconds there is a shoulder in the decay of the current, which looks like there is a different reduction process happening. Additionally, the steady state current is larger with increasing current, indicating that more copper is being reduced at the electrode surface. The open circuit potential becomes more positive, starting from -225 mV in the antimony citrate solution to an immediate jump of -200 mV in the 0.5:1 Cu:Sb solution and slowly increases up to -185 mV in the 4:1 Cu:Sb solution (a plot of this can be seen in Appendix 4.3). The OCP results indicate the reaction is becoming more favorable with increasing copper concentration. This is contrary to what is predicted by the Nernst equation of the redox couple Cu/Cu^{2+}, where the potential should become more negative with increasing copper concentration.

From the CVs in Figure 4.5B it is possible propose what species are being reduced in solution. As outlined at the end of Chapter 3 the two main species being reduced are $[Sb(HCit)_2]^-$ and $[Cu_2Cit_2H_{-1}]^{3-}$ described by equation 4.4 and the previously described equation 4.3.

$$[Sb(HCit)_2]^- + 2H_2O + 3e^- \rightarrow Sb^0 + 2Cit^{3-} + 2H_3O^+ \qquad \text{Eq. 4.4}$$

It is interesting to look at the CV for the 0.5:1 solution because even though there is a relatively small amount of copper present there is a sharp peak at 875 mV. This peak grows with increasing copper concentration. Similarly, the second peak in the CV at -1000 mV grows with increasing copper concentration. Interestingly, this peak also grows with increasing antimony concentration as discussed in Chapter 3, Figure 3.26B. Based on this, we attribute the peak at -1000 mV to either be a change in the reduction

potential of copper since the surface is changing from copper to copper antimonide, or to the reduction of a heterometallic antimony citrate species.

4.3.2. Electrodeposition of Crystalline Nickel Antimonide

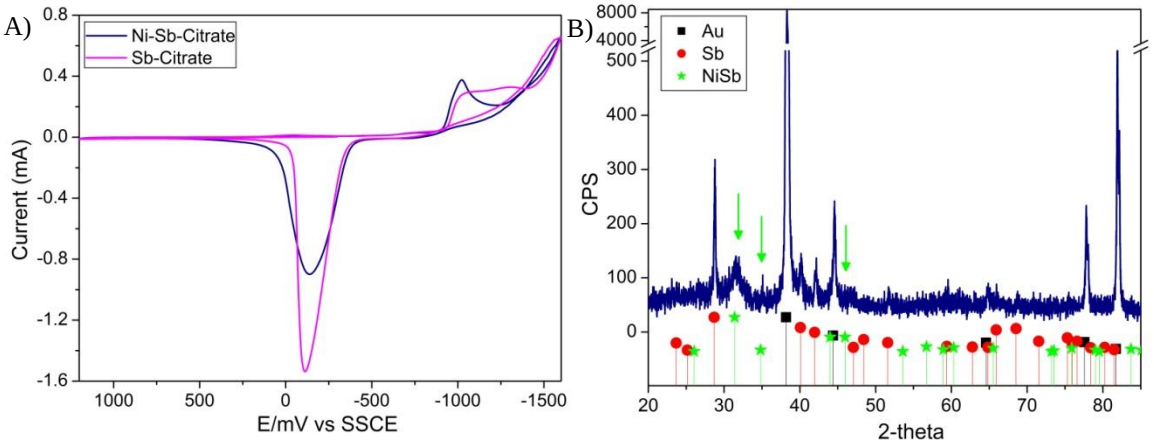

Figure 4.6. A) Cyclic voltammogram of 0.08 M $Ni(NO_3)_2$ and 0.025 M Sb_2O_3 in 0.4 M citric acid brought to pH 6 with potassium hydroxide, without nickel in solution at as scan rate of 100 mV/s on a 2.01 mm^2 platinum working electrode. B) XRD powder pattern of film deposited at -1500 mV for 10 minutes in the Ni-Sb-citrate solution described in (A). Films produce peaks that index to NiSb along with peaks that index to antimony metal.

Based off the co-deposition hypothesis nickel antimonide may deposit, as well, under similar conditions as the copper antimonide experiments. Nickel antimonide is a possible replacement anode material that could be used lithium-ion batteries due to its theoretical capacity of 532 mAh/g[31] (compared to 372 mAh/g for graphite).[42] CVs were taken of the prepared Ni-Sb-Citrate solution and were very similar to the already well studied Sb-citrate solution. Figure 4.6A shows CVs of both the antimony citrate and nickel antimony citrate solutions at a pH of 6. Individual nickel citrate CVs at different pH values can be seen in Appendix 4.4. There is no stripping peak of nickel in the CV similarly to what was seen with the copper citrate CV. As described earlier this may be due to the presence of oxides and complex citrate ions in this solution from a local pH increase during the reduction of the nickel citrate complex.[39]

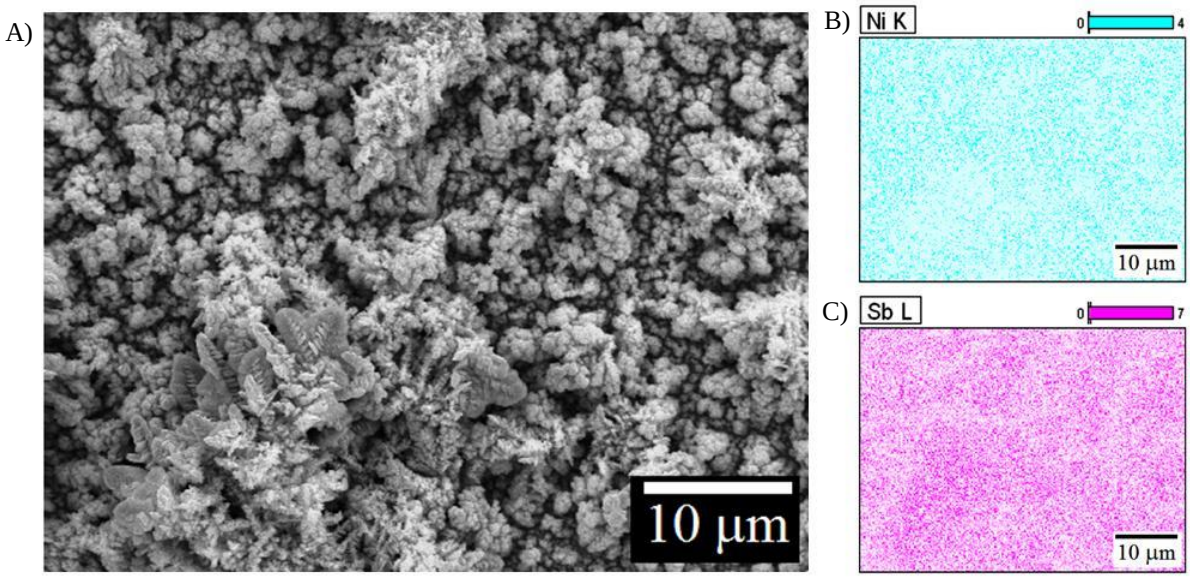

Figure 4.7. A) SEM image of a film deposited at -1500 mV for 10 minutes in a solution of 0.08 m $Ni(NO_3)_2$ and 0.025 m Sb_2O_3 in 0.4 m citric acid brought to pH 6 with potassium hydroxide. B) and C) Corresponding EDS mapping pattern for nickel and antimony rastered across film for five minutes.

Table 4.3. EDS results for the film deposited at -1500 mV for 10 minutes in a solution of 0.08 m $Ni(NO_3)_2$ and 0.025 m Sb_2O_3 in 0.4 m citric acid brought to pH 6 with potassium hydroxide. The gold detected is from the substrate.

Line	Atomic %
C K	27
O K	23
Ni K	17
Sb L	32
Au L	1
Molar Ratio	**Ratio Sb:Ni = 1.9**

Three potentials were chosen to deposit NiSb based on the CVs in Figure 4.6: -850 mV (initial current increase), -1050 mV (maximum current), and -1500 mV (past the reduction peak). Crystalline NiSb (PDF: 03-065-0935) was deposited at the -1500 mV potential as shown from the XRD powder pattern in Figure 4.6B. At least three peaks matched crystalline NiSb, but antimony metal was also deposited as evident by the four other peaks in the XRD which indexed to the antimony metal standard.

To confirm the results by XRD, the film was examined through SEM and analyzed with EDS (Figure 4.7 and Table 4.3). The EDS results in Table 4.3 show the presence of both antimony and nickel. According to EDS, antimony is abundant in about

twice the molar ratio as nickel, which is explained by the extra antimony metal peaks already discussed in the XRD pattern. Based off previous results with the copper-rich copper antimonide depositions this ratio could be brought closer to the 1:1 ratio by doubling the nickel content in solution. Figure 4.7A shows the SEM image in Figure 4.7A of the film deposited at -1500 mV. From the EDS mapping software images (Figure 4.7B), it appears that the nodal areas of the SEM are the NiSb and the area that appears "fern" like is the antimony metal. This "fern" type of morphology is expected from films electrodeposited at high overpotentials, further suggesting the different morphology is antimony metal over NiSb.[43]

An interesting trend was observed for the film deposited at a potential of -1050 mV. The XRD powder pattern of the film did not have any NiSb peaks, but there were far more peaks for antimony metal than seen in the past for antimony metal electrodeposition. A control deposition was performed using the same stock solution of antimony citrate to compare the crystallinity to that done with the nickel-antimony-citrate solution. Figure 4.8A shows the difference in the XRD patterns between the two films. There are a total of 15 antimony metal peaks when nickel is present suggesting polycrystalline growth, but only two when it is not present suggesting the film is more amorphous. This is consistent with the SEM images shown in Figure 14.8B. The dendritic growth occurred when the film depositing from the solution containing nickel, while without nickel (Figure 4.8C) there was much less material present and the film showed a far different morphology. This morphology difference might occur because slight impurities from the under potential deposition of nickel, which may facilitate the deposition of the antimony metal.

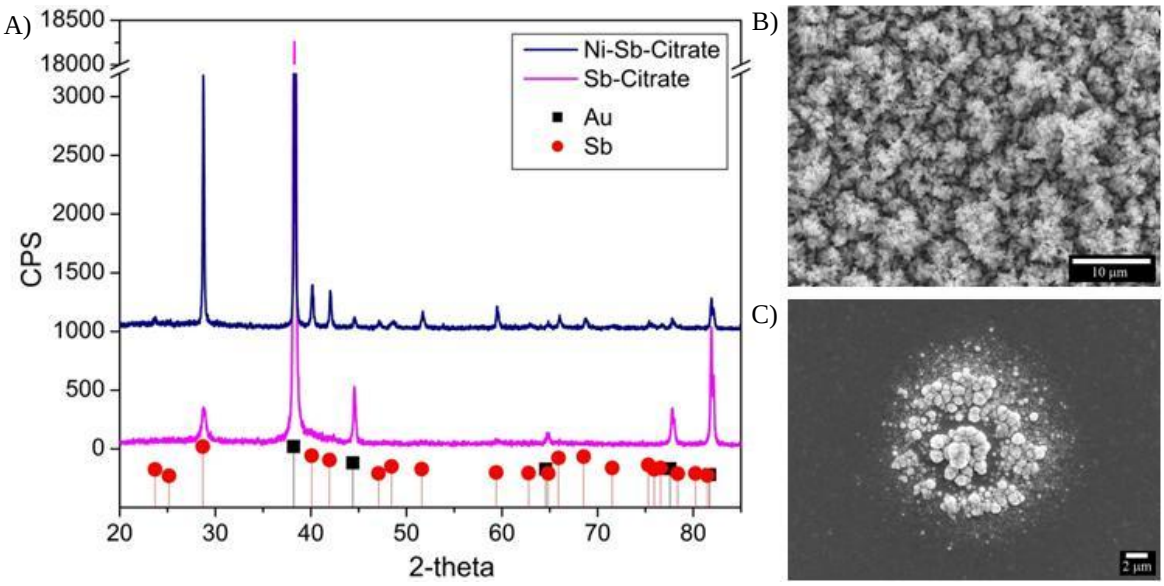

Figure 4.8. A) XRD powder pattern of a film deposited at -1050 mV for 10 minutes in a solution of 0.08 m $Ni(NO_3)_2$ and 0.025 m Sb_2O_3 in 0.4 m citric acid brought to pH 6 with potassium hydroxide compared to XRD powder pattern of film deposited at same potential, without nickel in solution. The same films were looked at with SEM and shown in B) and C). B) Film deposited from a solution containing nickel and C) Film deposited in a solution containing no nickel.

4.3.3. Co-deposition of Iron Antimonide

Iron antimonide is known to be a replacement anode for lithium ion batteries as well as a possible thermoelectric material.[29, 32-35] The crystal structure $FeSb_2$ has shown a very large Seebeck coefficient (S) = −45 mV/K at 12 K.[35] It has been shown that iron can be electrodeposited out of a citrate bath,[23] but more importantly, Sadana *et al.* demonstrated that both iron and antimony can be electrodeposited out of a citrate bath as an alloy.[44] Based on our previous data suggesting a co-deposition mechanism, we hypothesize that it may be possible to adjust the concentration of iron and antimony to target one of the four different iron antimonides: FeSb, $FeSb_2$, $Fe_{2.55}Sb_2$, and $Fe_{0.95}Sb_{0.05}$. It would be beneficial to be able to electrodeposit the material out of aqueous solution as a crystalline material.

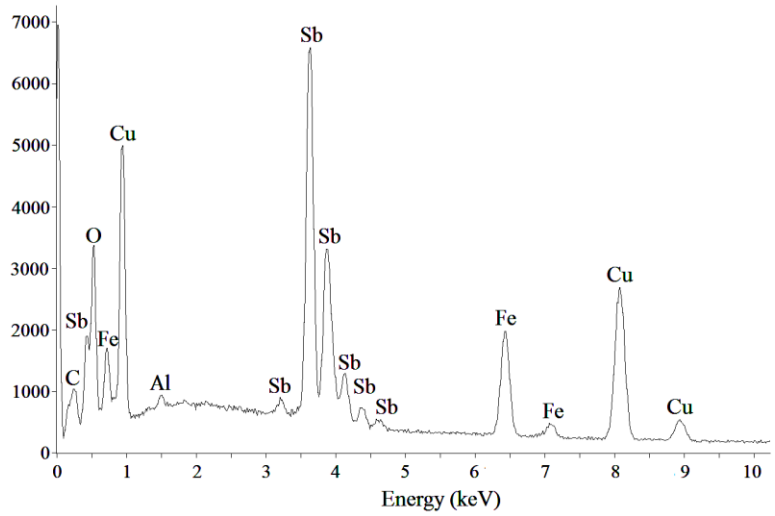

Figure 4.9. EDS spectra of a film deposited at -1500 mV for 10 minutes in a solution of 48 mM $Fe(NO_3)_3$ and 24 mM Sb_2O_3 in 380 mM citric acid brought to pH 5 with potassium hydroxide on copper substrate. Spectrum shows both iron and antimony present.

Table 4.4. EDS results for the film deposited at -1500 mV for 10 minutes in a solution of 48 mM $Fe(NO_3)_3$ and 24 mM Sb_2O_3 in 380 mM citric acid brought to pH 5 with potassium hydroxide on copper substrate.

Line	**Atomic %**
C K	20
O K	26
Ni K	10
Sb L	13
Cu L	30
Molar Ratio	**Ratio Sb:Fe= 1.4**

A deposition was done at -1500 mV for 10 minutes at pH 5 in a 1:1 ratio of iron (47 mM) to antimony (47 mM) in 0.38 M citric acid at 52 °C. The XRD powder pattern only showed the presence of crystalline antimony metal in both cases. The EDS results however, indicated both iron and antimony present as shown in Figure 4.9. The mole ratio according to EDS was approximately 1.4 to 1 antimony to iron as can be seen in Table 4.4. For comparison an SEM image of iron antimony film co-deposited onto a copper substrate is shown in Appendix 4.5.

If the concentrations or potential of the deposition were changed to increase/decrease the iron content in the deposit closer to the ratios of the above crystal

structures, it may be possible to obtain crystalline compound rather than an alloy, as was shown the case with copper-rich copper antimonide compounds.

4.3.4. Model for the Co-deposition of Crystalline Intermetallic Antimonides

Based on the understanding of the speciation in our system, we developed a method to reproducibly deposit films of various thicknesses (Chapter 1). We have shown that the solution chemistry (speciation) determines which species are present in solution (Chapter 3). These species can only diffuse so fast, based on their solution diffusion rate. Under the copper to antimony ratio of 1.5:1 the electrodeposition product is crystalline Cu_2Sb. If the concentration of copper is further increased or the solution is mixed, forcing copper species to reach the electrode faster, then the electrodeposition product changes to a copper-rich copper antimonide phase such as $Cu_{11}Sb_3$ (Chapter 1 and 4). Both copper and antimony are able to be electrodeposited out of separate metal citrate solutions where their mass values increase with solution concentration. The sum of the mass of these metals separately deposited is similar to the mass of a film electrodeposited out a bath containing both of these metals. These observations led to a co-deposition reaction being the likely process the electrodeposition of Cu_2Sb proceeds through (equation 4.2). Furthermore, this reaction can be used to predict the product, at higher concentrations of copper added to the solution, as was shown through the electrodeposition of different crystalline phases of copper antimonide: Cu_3Sb, $Cu_{11}Sb_3$, Cu_4Sb, $Cu_{0.95}Sb_{0.05}$.

The changes in crystallinity between Cu_2Sb, NiSb, and the co-deposited alloy FeSb do not depend directly on the starting ratio of the metals in solution. For example, the product Cu_2Sb is most crystalline when the solution is at a 1.5:1 ratio copper to

antimony in solution and crystalline NiSb was electrodeposited from a 1.5:1 ratio of nickel to antimony. The solution speciation dictates what is available to be electrodeposited and the rate of which these species diffuse in solution to the electrode surface is dependent on the diffusion rate. Furthermore the potential of the electrode dictates if and how fast the metal can be reduced from its' solution species. After the metal has been electrodeposited, the reduced metal atom will travel across the surface to find the lowest Gibbs free energy location. Depending on the concentration of the surrounding metals in the solid state, the final product may be an alloy or a stable crystal phase. This concept is best described in the diagram in Figure 4.10 adapted from Pfeiler *et al.*[45] The lowest energies maybe a crystalline phase, but in order to reach these crystal structures the concentration of the two compounds being deposited must be within a certain thermodynamic range.[45]

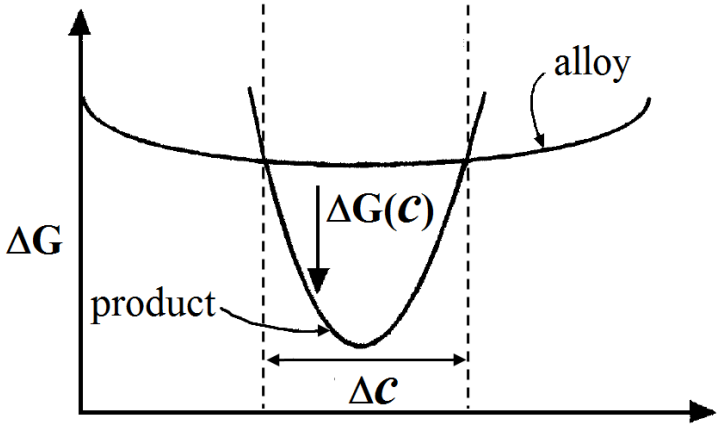

Figure 4.10. Cartoon depicting Gibbs free energy of alloy and crystalline product where the crystallized phase is only possible within a narrow range of concentration values. Adapted from Pfeiler *et al.*[45]

The diffusion of the metals across the surface and within a crystal structure are based on the solid-state diffusion rates. It is known that noble metals (Cu, Ag, Au), Ni-group elements (Ni, Pd, Pt), and Zn have diffusion rates which are three or more orders of magnitude faster than even self-diffusion in certain polyvalent metals such as In, Sn,

Sb, Ti, Zr, Hf, and most notably Pb.[46] These solid phase solvents that permit this fast diffusion are sometimes called open metals due to the large ratio of the atomic radii of the solvent (polyvalent metals) and solute (noble metals) in the solid state.[47] This high diffusion rate is known to occur through a process called interstitial diffusion and has been well studied in lead.[46, 48] This interstitial diffusion is able to occur because the metals mentioned above have an open structure where the smaller noble metals can diffuse through the open sites, as well as several factors outlighyned in greater detal in Neumann *et al.*[47]

Since antimony is one of the metals above listed as an open metal, fast diffusion is expected in this metal as well. The high crystallinity of the electrodeposited Cu_2Sb may be due to the high diffusion rate of copper through the interstitial diffusion mechanism in antimony. Nickel also has high diffusion rates in open metals, which could explain the success of the electrodeposition of the NiSb product above. Based on this we believe it is possible to electrodeposit other noble metal antimonides due to the fast interstitial diffusion.

4.4. Conclusion

We have shown that by understanding solution chemistry we can deposit other metal antimonides through the preliminary success of the electrodeposition of crystalline NiSb, the co-deposition of FeSb, and several copper-rich copper antimonide phases from aqueous citrate solutions. It is shown that a through co-deposition process, which is dependent on the solution chemistry and diffusion of the metals in the solid state, crystalline intermetallic antimonides can be deposited. This leads to a better understanding of the electrodeposition of the Cu_2Sb system, which can lead to further

improvement of the electrodeposition of other transition metal antimonides and intermetallics.

Thus, combining the solution chemistry with the proper ratio of elements in this accelerated solid-state diffusion, our model for Cu_2Sb electrodeposition can be applied to other intermetallics. We have therefore shown the electrodeposition of the following intermetallics using a citrate bath: NiSb, Cu_3Sb, $Cu_{11}Sb_3$, Cu_4Sb, $Cu_{0.95}Sb_{0.05}$, $CoSb_2$,[26] and $CoSb_3$[26] . Additionally, the co-deposition of FeSb, MnSb[19] and ZnSb[19] can be attributed to a similar co-deposition process in solution. Through an understanding of the solution chemistry, electrodeposition parameters, and solid state diffusion rates, a better electrodeposition model was proposed for the electrodeposition of Cu_2Sb and applied to a range of intermetallic compounds that can be used for other applications.

4.5. References

1. Mills, A. M.; Lam, R.; Ferguson, M. J.; Deakin, L.; Mar, A., Chains, planes, and antimonides. *Coordination Chemistry Reviews* **2002,** *233-234*, 207-222.

2. Kleinke, H., From molecular Sb units to infinite chains, layers, and networks: Sb-Sb interactions in metal-rich antimonides. *Chemical Society Reviews* **2000,** *29* (6), 411-418.

3. Caillat, T.; Borshchevsky, A.; Fleurial, J. P., Properties of single crystalline semiconducting $CoSb_3$. *Journal of Applied Physics* **1996,** *80* (8), 4442-4449.

4. Fulop, T.; Bekele, C.; Landau, U.; Angus, J.; Kash, K., Electrodeposition of polycrystalline InSb from aqueous electrolytes. *Thin Solid Films* **2004,** *449* (1-2), 1-5.

5. Solin, S. A.; Thio, T.; Hines, D. R.; Heremans, J. J., Enhanced room-temperature geometric magnetoresistance in inhomogeneous narrow-gap semiconductors. *Science* **2000,** *289* (5484), 1530-1532.

6. Vaughey, J. T.; Fransson, L.; Swinger, H. A.; Edstrom, K.; Thackeray, M. M., Alternative anode materials for lithium-ion batteries: a study of Ag_3Sb. *Journal of Power Sources* **2003,** *119*, 64-68.

7. Bruce, P. G.; Scrosati, B.; Tarascon, J. M., Nanomaterials for rechargeable lithium batteries. *Angew. Chem.-Int. Edit.* **2008,** *47* (16), 2930-2946.

8. Fransson, L. M. L.; Vaughey, J. T.; Edstrom, K.; Thackeray, M. M., Structural transformations in intermetallic electrodes for lithium batteries - An in situ x-ray diffraction study of lithiated MnSb and Mn_2Sb. *Journal of the Electrochemical Society* **2003,** *150* (1), A86-A91.

9. Mosby, J. M.; Prieto, A. L., Direct Electrodeposition of Cu_2Sb for Lithium-Ion Battery Anodes. *J. Am. Chem. Soc.* **2008,** *130* (32), 10656-10661.

10. Fransson, L. M. L.; Vaughey, J. T.; Benedek, R.; Edstrom, K.; Thomas, J. O.; Thackeray, M. M., Phase transitions in lithiated Cu_2Sb anodes for lithium batteries: an in situ X-ray diffraction study. *Electrochemistry Communications* **2001,** *3* (7), 317-323.

11. Song, S. W.; Reade, R. P.; Cairns, E. J.; Vaughey, J. T.; Thackeray, M. M.; Striebel, K. A., Cu_2Sb thin-film electrodes prepared by pulsed laser deposition for lithium batteries. *Journal of the Electrochemical Society* **2004,** *151* (7), A1012-A1019.

12. Sarakonsri, I.; Johnson, C. S.; Hackney, S. A.; Thackeray, M. M., Solution route synthesis of InSb, Cu_6Sn_5 and Cu_2Sb electrodes for lithium batteries. *Journal of Power Sources* **2006,** *153* (2), 319-327.

13. Vitkina, T. Z.; Zhigadlo, N. D.; Ryzhkovskii, V. M., Diamagnetism and Some Peculiarities of Interatomic Interactions in Cu_2Sb. *Cryst. Res. Technol.* **1988,** *23* (7), 945-948.

14. Kulifay, S. M., A Low Temperature Synthesis for Powder-form Intermetallics and Other Compounds. **1961,** *83*, 4916.

15. Morcrette, M.; Larcher, D.; Tarascon, J. M.; Edström, K.; Vaughey, J. T.; Thackeray, M. M., Influence of electrode microstructure on the reactivity of Cu_2Sb with lithium. *Electrochimica Acta* **2007,** *52* (17), 5339-5345.

16. Chazova, L., Cathodic Reduction of Antimony(III) in tartrate solutions on a platinum electrode. *Izvestia vyssih ucebnyh zavedenij. Himia i himiceskaa tehnologia* **1978,** *21* (8), 1163-.

17. Ren, J.; He, X.; Pu, W.; Jiang, C.; Wan, C., Chemical reduction of nano-scale Cu_2Sb powders as anode materials for Li-ion batteries. *Electrochimica Acta* **2006,** *52* (4), 1538-1541.

18. Takei, T., Consideration of the Electrodeposition of Metals. *Surface Technology* **1979,** *8* (6), 543-552.

19. Noblitt, J. M., Co-deposition of ZnSb and MnSb. Colorado State University: 2010.

20. Mosby, J. M., Electrodepositon of Crystalline $Cu_{3.3}Sb$ from Malic Acid complexing agent. Colorado State University: 2007.

21. Uksene, V.; Survila, A.; Zukauskaite, A., The electroreduction mechanism of copper(II) citrate complexes. *Russ. J. Electrochem.* **1996,** *32* (8), 884-888.

22. Popov, B. N.; Li, W.; White, R. E., A Study of the Stability of Ni-Cr-P Plating Solutions. *Plat. Surf. Finish.* **1992,** *79* (11), 72-78.

23. Danilov, F. I.; Protsenko, V. S.; Ubiikon, A. V., Kinetic regularities governing the reaction of electrodeposition of iron from solutions of citrate complexes of iron(III). *Russ. J. Electrochem.* **2005,** *41* (12), 1282-1289.

24. Lacnjevac, U.; Jovic, B. M.; Jovic, V. D., Morphology and composition of the Fe-Ni powders electrodeposited from citrate containing electrolytes. *Electrochimica Acta* **2009,** *55* (2), 535-543.

25. Cheng, H.; Hng, H. H.; Ma, J., A study on the electrodeposition behavior of cobalt antimonides in citric based solutions. In *Advanced Structural and Functional Materials for Protection*, Lau, W.; Min, S. H.; Sua, L. N.; Jan, M.; Tok, A., Eds. Trans Tech Publications Ltd: Stafa-Zurich, 2008; Vol. 136, pp 75-82.

26. Cheng, H.; Hng, H. H.; Ma, J.; Xu, X. J., Effect of various deposition parameters on the co-deposition behavior of cobalt antimony in citric-based solution. *J. Mater. Res.* **2008,** *23* (11), 3013-3020.

27. Rode, S.; Henninot, C.; Matlos, M., Complexation chemistry in nickel and copper-nickel alloy plating from citrate baths. *Journal of the Electrochemical Society* **2005,** *152* (4), C248-C254.

28. Eliaz, N.; Gileadi, E., Induced Codeposition of Alloys of Tungsten, Molybdenum and Rhenium with Transition Metals In *Modern Aspects of Electrochemistry*, Vayenas, C. G.; White, R. E.; Gamboa-Aldeco, M. E., Eds. Springer: New York, 2008; Vol. 42, pp 191-301.

29. Park, C.-M.; Sohn, H.-J., Antimonides ($FeSb_2$, $CrSb_2$) with orthorhombic structure and their nanocomposites for rechargeable Li-ion batteries. *Electrochimica Acta* **2010,** *55* (17), 4987-4994.

30. Xie, J.; Zhao, X. B.; Yu, H. M.; Qi, H.; Cao, G. S.; Tu, J. P., Low temperature solvothermal synthesis of nanosized NiSb as a Li-ion battery anode material. *J. Alloy. Compd.* **2007,** *441* (1-2), 231-235.

31. Li, C. H.; Hu, J.; Peng, Q.; Wang, X., Synthesis and characterization of nanocrystalline NiSb and NiSb2 at low temperature. *Mater. Chem. Phys.* **2008,** *110* (1), 106-109.

32. Xie, J.; Cao, G. S.; Zhao, X. B., Lithiation and delithiation behaviors of FeSb alloy. *Rare Metal Mat. Eng.* **2005,** *34* (6), 850-853.

33. Kumari, L.; Li, W.; Huang, J. Y.; Provencio, P. P., Nanosize Transition Metal Antimonides, NiSb and $FeSb_2$: Solvothermal Synthesis and Characterization. *The Journal of Physical Chemistry C* **2010,** *114* (21), 9573-9579.

34. Tomczak, J. M.; Haule, K.; Miyake, T.; Georges, A.; Kotliar, G., Thermopower of correlated semiconductors: Application to $FeAs_2$ and $FeSb_2$. *Physical Review B* **2010,** *82* (8).

35. Bentien, A.; Johnsen, S.; Madsen, G. K. H.; Iversen, B. B.; Steglich, F., Colossal Seebeck coefficient in strongly correlated semiconductor FeSb2. *Epl* **2007,** *80* (1).

36. Mosby, J. M.; Johnson, D. C.; Prieto, A. L., Evidence of Induced Underpotential Deposition of Crystalline Copper Antimonide via Instantaneous Nucleation. *Journal of the Electrochemical Society* **2010,** *157* (6), E99-E105.

37. Tzec, F. I. L.; Oskam, G. In *Electrodeposition of Copper in Trenches from a Citrate Plating Bath*, ECS Meeting Abstracts, 2009; p 2781.

38. Tzec, F. I. L.; Oskam, G., Electrodeposition of Copper in Trenches From a Citrate Plating Bath. *ECS Transactions* **2010,** *25* (27), 195-201.

39. Kim, S.; Duquette, D. J., Nucleation characteristics of directly electrodeposited copper on TiN. *Journal of the Electrochemical Society* **2006,** *153* (9), C673-C676.

40. Kim, S.; Duquette, D. J., Effect of chemical composition on adhesion of directly electrodeposited copper film on TiN. *Journal of the Electrochemical Society* **2006,** *153* (6), C417-C421.

41. Rode, S.; Henninot, C.; Vallieres, C. C.; Matlosz, M., Complexation chemistry in copper plating from citrate baths. *Journal of the Electrochemical Society* **2004,** *151* (6), C405-C411.

42. Bruce, P. G., Energy storage beyond the horizon: Rechargeable lithium batteries. *Solid State Ionics* **2008,** *179* (21-26), 752-760.

43. Choi, K. S., Shape control of inorganic materials via electrodeposition. *Dalton Trans.* **2008,** (40), 5432-5438.

44. Sadana, Y. N.; Kumar, R., Iron-Antimony Alloy Deposition from Citrate Solutions. *Plat. Surf. Finish.* **1979,** *66* (4), 58-64.

45. Pfeiler, W., *Alloy physics a comprehensive reference*. Wiley-VCH John Wiley, distributor: Weinheim, 2007; p 973.

46. Mehrer, H., *Diffusion in solids fundamentals, methods, materials, diffusion-controlled processes*. Springer: Berlin, 2007; p 651.

47. Neumann, G.; Tuijn, C., Interstitial impurity diffusion in metals; the apparent size effect. *Physica B* **2002,** *315* (1-3), 164-170.

48. Neumann, G.; Tuijn, C., *Self-diffusion and impurity diffusion in pure metals handbook of experimental data*. 1st ed. ed.; Elsevier: Amsterdam, 2009; p 349.

5. Appendices

AFM Data was analyzed by taking an average of the lines taken by the AFM over the step edge. A pictorial example of the area averaged is shown in Appendix 1.1A and the graph of the average height versus position of those averaged lines is shown in Appendix 1.1B. Those lines (always greater than 10) were averaged using the SPIP software, and then the difference between Cu_2Sb and the polished copper surface was measured using Excel. The whole region cannot be measured since it is not flat so just flat regions were measured as shown highlighted in Appendix 1.2B. Once a difference was measured this was one data point. A similar procedure was repeated for all films (2 images for each film and 3 films per deposition time point). The average and standard deviation reported are from these 6 data points for each deposition time point.

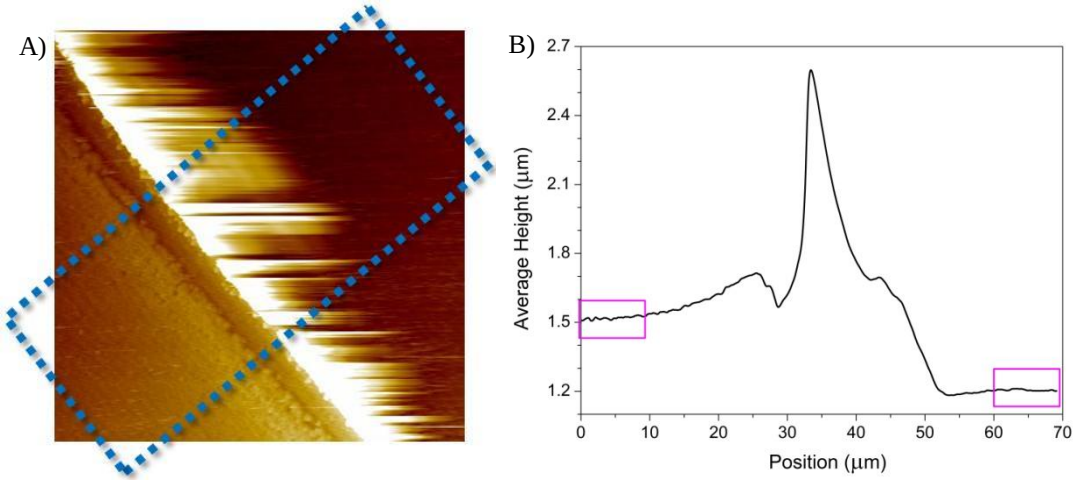

Appendix 1.1. Pictorial examples of how the data collected from the AFM results was extracted and a thickness of the film calculated. A) Image from AFM overlaid with box representing lines taken for average. B) Graph showing the averaged height versus position of image on left. Highlighted boxes show flat regions in graph that were used to take the difference in height.

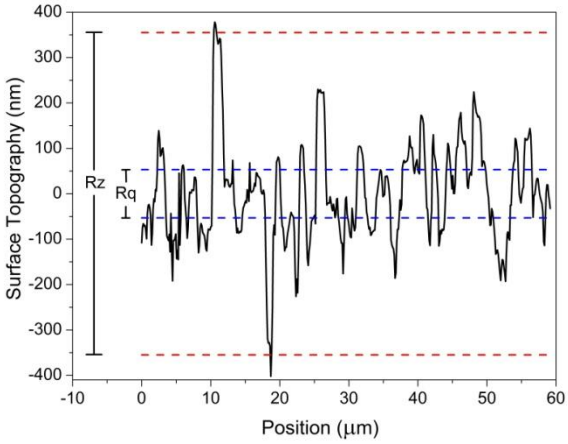

Appendix 1.2. Graphical example of calculated ten-point height roughness (Rz) the root mean square (RMS) roughness (Rq). Calculated using equations 1.1 and 1.2 respectively.

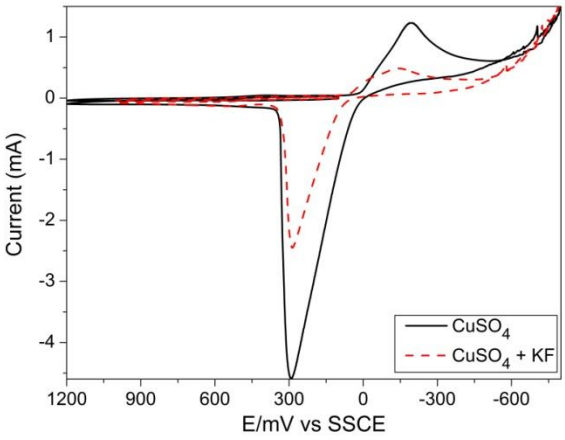

Appendix 2.1. Cyclic voltammogram of a 0.1 M $CuSO_4$ with 1% H_2SO_4 solution at 100 mV/s versus SSCE on a 2.01 mm^2 platinum working electrode compared to diluted solution with 1 M potassium fluoride addition.

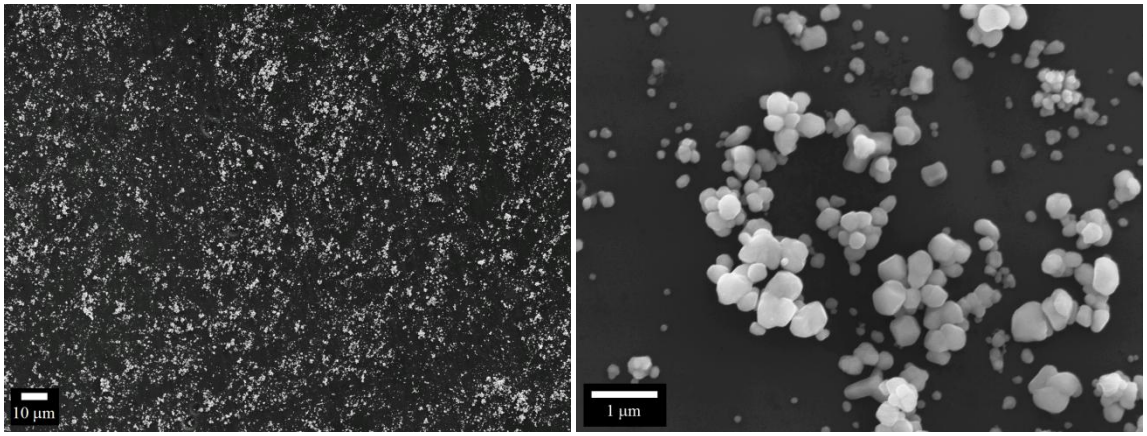

Appendix 2.2. SEM images of copper deposited onto an aluminum substrate out of a solution of 0.1 M $CuSO_4$ with 1% H_2SO_4 and 1 M potassium fluoride. Copper deposition completed at -0.6 V. Aluminum substrate previously had 2 µm of AAO template, which fluoride dissolved template completely.

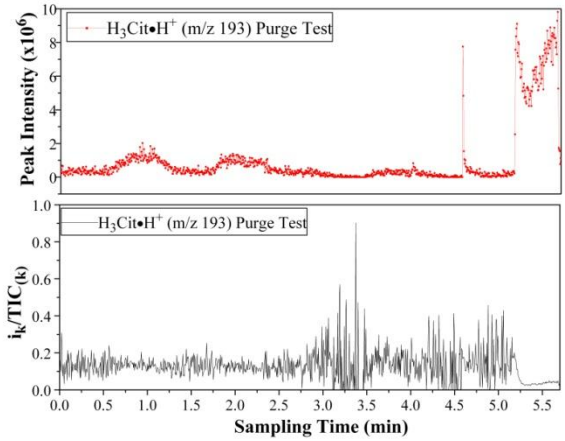

Appendix 3.1. Syringe pump was turned on and off every 100 scans for 500 total scans, and then the flow was turned off completely, which followed by pushing the back of the syringe manually. Intensity is shown in the top graph and the bottom graph shows what the data looks like after the normalization procedure in Equation 3.2. The plot of the ratio versus time is flat compared to the intensity plot (large spikes are where there is lower than normal flow rates.

m/z	+ or -	Formula	Exact Mass	Compound
111	-	$C_5H_3O_3$	111.01	(H_3Cit) - loss COOH, $(OH)_2$, $(H)_2$
129	+	$C_5H_5O_4$	129.02	(H_3Cit) - loss COOH, OH, H
147	+	$C_5H_7O_5$	147.03	(H_3Cit) - loss COOH
175	+	$C_6H_7O_6$	175.02	(H_3Cit) - loss OH
191	-	$C_6H_7O_7$	191.02	$[H_2Cit]^-$
193	+	$C_6H_8O_7H$	193.03	$[(H_3Cit)•H]^+$
210	+	$C_6H_8O_7NH_4$	210.06	$[(H_3Cit)•NH_4]^+$
213	-	$C_6H_6O_7Na$	213.00	$[(HCit)^{2-}•Na]^-$
215	+	$C_6H_8O_7Na$	215.02	$[(H_3Cit)•Na]^+$
229	-	$C_6H_6O_7K$	228.98	$[(HCit)^{2-}•K]^-$
231	+	$C_6H_8O_7K$	230.99	$[(H_3Cit)•K]^+$
269	+	$C_6H_7O_7K_2$	268.95	$[(H_2Cit)•K_2]^+$
383	-	$C_{12}H_{15}O_{14}$	383.05	$[(H_2Cit)^-(H_3Cit)]^-$
385	+	$C_{12}H_{17}O_{14}$	385.06	$[(H_3Cit)_2•H]^+$
400	-	$C_{12}H_{14}O_{14}NH_4$	400.07	$[(HCit)^{2-}•NH_4]^-$
402	+	$C_{12}H_{16}O_{14}NH_4$	402.09	$[(H_3Cit)_2•NH_4]^+$
405	-	$C_{12}H_{14}O_{14}Na$	405.03	$[(H_2Cit)_2•Na]^-$
407	+	$C_{12}H_{16}O_{14}Na$	407.04	$[(H_3Cit)_2•Na]^+$
421	-	$C_{12}H_{14}O_{14}K$	421.00	$[(H_2Cit)^-_2•K]^-$
423	+	$C_{12}H_{16}O_{14}K$	423.02	$[(H_3Cit)_2•K]^+$
459	-	$C_{12}H_{13}O_{14}K_2$	458.96	$[(HCit)^{2-}(H_2Cit)^-•K_2]^-$
461	+	$C_{12}H_{15}O_{14}K_2$	460.97	$[(H_3Cit)(H_2Cit)•K_2]^+$
615	+	$C_{18}H_{24}O_{21}K$	615.04	$[(H_3Cit)_3•K]^+$

Appendix 3.2. Citric acid species identified in solutions of citric acid at various pH values though ESI-MS in both positive and negative ion mode

m/z	+ or -	Formula	Exact Mass	Compound
111	-	$C_5H_3O_3$	111.01	$[(H_3Cit)]^-$ loss COOH, $(OH)_2$, $(H)_2$
129	+	$C_5H_5O_4$	129.02	$[(H_3Cit)]^+$ loss COOH, OH, H
147	+	$C_5H_7O_5$	147.03	$[(H_3Cit)]^+$ loss COOH
175	+	$C_6H_7O_6$	175.02	$[(H_3Cit)]^+$ loss OH
191	-	$C_6H_7O_7$	191.02	$[H_3Cit]^-$
193	+	$C_6H_8O_7H$	193.03	$[(H_3Cit)\bullet H]^+$
210	+	$C_6H_8O_7NH_4$	210.06	$[(H_3Cit)\bullet NH_4]^+$
213	-	$C_6H_6O_7Na$	213.00	$[(HCit)^{2-}\bullet Na]^-$
215	+	$C_6H_8O_7Na$	215.02	$[(H_3Cit)\bullet Na]^+$
229	-	$C_6H_6O_7K$	228.98	$[(HCit)^{2-}\bullet K]^-$
231	+	$C_6H_8O_7K$	230.99	$[(H_3Cit)\bullet K]^+$
269	+	$C_6H_7O_7K_2$	268.95	$[(H_2Cit)\bullet K_2]^+$
252	-	$C_6H_5O_7Cu$	251.93	$[(Cit)\bullet Cu]^-$
254	+	$C_6H_7O_7Cu$	253.95	$[(H_2Cit)\bullet Cu]^+$
269	+	$C_6H_7O_7K_2$	268.95	$[(H_2Cit)\bullet K_2]^+$
271	+	$C_6H_6O_7CuNH_4$	270.98	$[(HCit)\bullet Cu\bullet NH_4]^+$
273	+	$C_6H_7O_7CuH_2O$	272.97	$[(H_3Cit)\bullet Cu\bullet H_2O]^+$
315	+	$C_6H_5O_7Cu_2$	314.86	$[(Cit)\bullet Cu_2]^+$
400	-	$C_{12}H_{14}O_{14}NH_4$	400.07	$[(HCit)\bullet NH_4]^-$
405	-	$C_{12}H_{14}O_{14}Na$	405.03	$[(H_2Cit)_2\bullet Na]^-$
407	+	$C_{12}H_{16}O_{14}Na$	407.04	$[(H_3Cit)_2\bullet Na]^+$
421	-	$C_{12}H_{14}O_{14}K$	421.00	$[(H_2Cit)_2\bullet K]^-$
423	+	$C_{12}H_{16}O_{14}K$	423.02	$[(H_3Cit)_2\bullet K]^+$
444	-	$C_{12}H_{13}O_{14}Cu$	443.96	$[(H_2Cit)^-(HCit)^{2-}\bullet Cu]^-$
446	+	$C_{12}H_{15}O_{14}Cu$	445.98	$[(H_2Cit)^-(H_3Cit)\bullet Cu]^+$
459	-	$C_{12}H_{13}O_{14}K_2$	458.96	$[(HCit)(H_2Cit)\bullet K_2]^-$
463	+	$C_{12}H_{14}O_{14}CuNH_4$	463.00	$[(H_2Cit)_2\bullet Cu\bullet NH_4]^+$
505	-	$C_{12}H_{11}O_{14}Cu_2$	504.87	$[(HCit)^{2-}(Cit)^{3-}\bullet Cu_2]^-$
507	+	$C_{12}H_{13}O_{14}Cu_2$	506.89	$[(H_2Cit)^-(HCit)^{2-}\bullet Cu_2]^+$
523	-	$C_{12}H_{11}O_{14}Cu_2H_2O$	522.88	$[(HCit)^{2-}(Cit)^{3-}\bullet Cu_2\bullet H_2O]^-$
524	+	$C_{12}H_{13}O_{14}Cu_2NH_3$	523.92	$[(H_2Cit)^-(HCit)^{2-}\bullet Cu_2\bullet NH_3]^+$
541	+	$C_{12}H_{13}O_{14}Cu_2N_2H_6$	540.94	$[(H_2Cit)^-(HCit)^{2-}\bullet Cu_2\bullet (NH_3)]^+$
543	-	$C_{12}H_{10}O_{14}Cu_2K$	542.83	$[(Cit)^{3-}{}_2\bullet Cu_2\bullet K^+]^+$
545	+	$C_{12}H_{12}O_{14}Cu_2K$	544.85	$[(HCit)^{2-}{}_2\bullet Cu_2\bullet K^+]^+$
615	+	$C_{18}H_{24}O_{21}K$	615.04	$[(H_3Cit)_3\bullet K]^+$
636	-	$C_{18}H_{21}O_{21}Cu$	635.99	$[(H_2Cit)^-(HCit)^{2-}\bullet(H_3Cit)\bullet Cu]^-$
638	+	$C_{18}H_{23}O_{21}Cu$	638.00	$[(H_2Cit)^-(H_2Cit)\bullet(H_3Cit)\bullet Cu]^+$
689	-	$C_{18}H_{20}O_{21}K_3$	688.94	$[(HCit)(H_2Cit)_2\bullet K_3]^-$
697	-	$C_{18}H_{19}O_{21}Cu_2$	696.90	$[(HCit)^{2-}(Cit)^{3-}\bullet(H_3Cit)\bullet Cu_2]^-$
699	+	$C_{18}H_{21}O_{21}Cu_2$	698.92	$[(H_2Cit)^-(HCit)^{2-}\bullet(H_3Cit)\bullet Cu_2]^+$
758	-	$C_{18}H_{17}O_{21}Cu_3$	757.82	$[(Cit)(HCit)_2\bullet Cu_3]^-$
760	+	$C_{18}H_{19}O_{21}Cu_3$	759.83	$[(HCit)_2(H_2Cit)\bullet Cu_3]^+$
819	-	$C_{18}H_{15}O_{21}Cu_4$	818.73	$[(Cit)_3\bullet Cu_3]^-$
821	+	$C_{18}H_{17}O_{21}Cu_4$	820.74	$[(Cit)(HCit)_2\bullet Cu_4]^+$
919	-	$C_{24}H_{27}O_{28}K_4$	918.92	$[(HCit)(H_2Cit)_3\bullet K_4]^-$
952	-	$C_{24}H_{25}O_{28}Cu_3$	951.83	$[(HCit)_3(H_2Cit)\bullet Cu_3]^-$
954	+	$C_{24}H_{27}O_{28}Cu_3$	953.85	$[(HCit)(H_2Cit)_3\bullet Cu_3]^+$
1013	-	$C_{24}H_{23}O_{28}Cu_4$	1012.75	$[(Cit)(HCit)_3\bullet Cu_4]^-$
1015	+	$C_{24}H_{25}O_{28}Cu_4$	1014.75	$[(HCit)_3(H_2Cit)\bullet Cu_4]^+$
1074	-	$C_{24}H_{21}O_{28}Cu_5$	1073.66	$[(Cit)_3(HCit)\bullet Cu_5]^-$
1076	+	$C_{24}H_{23}O_{28}Cu_5$	1075.88	$[(Cit)(HCit)_3\bullet Cu_5]^+$
1205	-	$C_{30}H_{31}O_{35}Cu_4$	1204.77	$[(H_2Cit)_3(HCit)_2\bullet Cu_4]^-$
1207	+	$C_{30}H_{33}O_{35}Cu_4$	1206.79	$[(H_2Cit)_5\bullet Cu_4]^+$

Appendix 3.3. Copper citrate and citric acid species identified in solutions of 4.0 mM $Cu(NO_3)_2$ in 20.0 mM citric acid at various pH values though ESI-MS in both positive and negative ion mode. Species highlighted are those predicted from speciation in the literature.

m/z	+ or -	Formula	Exact Mass	Compound
111	-	$C_5H_3O_3$	111.01	(H_3Cit) - loss COOH, $(OH)_2$, $(H)_2$
129	+	$C_5H_5O_4$	129.02	(H_3Cit) - loss COOH, OH, H
147	+	$C_5H_7O_5$	147.03	(H_3Cit) - loss COOH
175	+	$C_6H_7O_6$	175.02	(H_3Cit) - loss OH
191	-	$C_6H_7O_7$	191.02	$[H_2Cit]^-$
193	+	$C_6H_8O_7H$	193.03	$[(H_3Cit)•H]^+$
210	+	$C_6H_8O_7NH_4$	210.06	$[(H_3Cit)•NH_4]^+$
213	-	$C_6H_6O_7Na$	213.00	$[(HCit)^{2-}•Na]^-$
215	+	$C_6H_8O_7Na$	215.02	$[(H_3Cit)•Na]^+$
231	+	$C_6H_8O_7K$	230.99	$[(H_3Cit)•K]^+$
269	+	$C_6H_7O_7K_2$	268.95	$[(H_2Cit)•K_2]^+$
311	**+**	**$C_6H_6O_7Sb$**	**310.92**	**$[(HCit)•Sb]^+$**
329	+	$C_6H_6O_7SbH_2O$	328.93	$[(HCit)•Sb•H_2O]^+$
333	+	$C_6H_6O_7SbNa$	332.90	$[(HCit)•Sb•Na]^+$
361	**-**	**$Sb(OH)_3C_6O_7H_5$**	**360.92**	**$[Sb•(OH)_3•(Cit)]^-$**
383	-	$C_{12}H_{15}O_{14}$	383.05	$[(H_2Cit)^-(H_3Cit)]^-$
385	+	$C_{12}H_{17}O_{14}$	385.06	$[(H_3Cit)_2•H]^+$
400	-	$C_{12}H_{14}O_{14}NH_4$	400.07	$[(HCit)•NH_4]^-$
402	+	$C_{12}H_{16}O_{14}NH_4$	407.04	$[(H_3Cit)_2•NH_4]^+$
405	-	$C_{12}H_{14}O_{14}Na$	405.03	$[(H_2Cit)_2•Na]^-$
407	+	$C_{12}H_{16}O_{14}Na$	407.04	$[(H_3Cit)_2•Na]^+$
421	-	$C_{12}H_{14}O_{14}K$	421.00	$[(H_2Cit)_2•K]^-$
423	+	$C_{12}H_{16}O_{14}K$	423.02	$[(H_3Cit)_2•K]^+$
459	-	$C_{12}H_{13}O_{14}K_2$	458.96	$[(HCit)(H_2Cit)•K_2]^-$
501	**-**	**$C_{12}H_{12}O_{14}Sb$**	**500.93**	**$[(HCit)_2•Sb]^-$**
503	**+**	**$C_{12}H_{14}O_{14}Sb$**	**502.94**	**$[(H_2Cit)_2•Sb]^+$**
518	-	$C_{12}H_{11}O_{14}SbNH_3$	517.95	$[(HCit)(Cit)•Sb•NH_3]^-$
520	+	$C_{12}H_{13}O_{14}SbNH_4$	519.97	$[(HCit)(H_2Cit)•Sb•NH_4]^+$
523	-	$C_{12}H_{11}O_{14}SbNa$	522.91	$[(HCit)(Cit)•Sb•Na]^-$
525	+	$C_{12}H_{13}O_{14}SbNa$	524.92	$[(HCit)(H_2Cit)•Sb•Na]^+$
615	+	$C_{18}H_{24}O_{21}K$	615.04	$[(H_3Cit)_3•K]^+$
621	**-**	**$C_{12}H_{11}O_{14}Sb_2$**	**620.82**	**$[(_{H-1}Cit)(Cit)•Sb_2]^-$**
623	**+**	**$C_{12}H_{13}O_{14}Sb_2$**	**622.84**	**$[(HCit)(Cit)•Sb_2]^+$**
640	+	$C_{12}H_{12}O_{14}Sb_2NH_4$	639.86	$[(Cit)_2•Sb_2•NH_4]^+$
645	+	$C_{12}H_{12}O_{14}Sb_2Na$	644.82	$[(Cit)_2•Sb_2•Na]^+$
661	+	$C_{12}H_{12}O_{14}Sb_2K$	660.79	$[(Cit)_2•Sb_2•K]^+$
695		$C_{18}H_{22}O_{21}Sb$	694.97	$[(H_2Cit)_2(H_3Cit)•Sb•NH_4]^+$
712	+	$C_{18}H_{21}O_{21}SbNH_4$	712.00	$[(H_2Cit)_3•Sb•NH_4]^+$
811	-	$Sb_2C_{18}H_{17}O_{21}$	810.83	$[(HCit)_2(Cit)•Sb_2]^-$
813	+	$Sb_2C_{18}H_{19}O_{21}$	812.85	$[(HCit)_2(H_2Cit)•Sb_2]^+$

Appendix 3.4. Antimony citrate and citric acid species identified in solutions of 1.25 mM Sb_2O_3 in 20.0 mM citric acid at various pH values though ESI-MS in both positive and negative ion mode. Species highlighted could be species present in solution.

m/z	+ or -	Formula	Exact Mass	Compound
191	-	$C_6H_7O_7$	191.02	$[H_2Cit]^-$
193	+	$C_6H_8O_7H$	193.03	$[(H_3Cit)\bullet H]^+$
444	-	$C_{12}H_{13}O_{14}Cu$	443.96	$[(H_2Cit)^-(HCit)^{2-}\bullet Cu]^-$
446	+	$C_{12}H_{15}O_{14}Cu$	445.98	$[(H_2Cit)^-(H_3Cit)\bullet Cu]^+$
501	-	$C_{12}H_{12}O_{14}Sb$	500.93	$[(HCit)_2\bullet Sb]^-$
503	+	$C_{12}H_{14}O_{14}Sb$	502.94	$[(H_2Cit)_2\bullet Sb]^+$
505	-	$C_{12}H_{11}O_{14}Cu_2$	504.87	$[(HCit)^{2-}(Cit)^{3-}\bullet Cu_2]^-$
507	+	$C_{12}H_{13}O_{14}Cu_2$	506.89	$[(H_2Cit)^-(HCit)^{2-}\bullet Cu_2]^+$
562	-	$CuSbC_{12}H_{10}O_{14}$	561.84	$[(Cit^{3-})_2\bullet Cu\bullet Sb]^-$
564	+	$CuSbC_{12}H_{11}O_{14}H$	563.86	$[(HCit)^{2-}(Cit)^{3-}\bullet Cu\bullet Sb\bullet H]^+$
621	-	$C_{12}H_{11}O_{14}Sb_2$	620.82	$[(_{H-1}Cit)(Cit)\bullet Sb_2]^-$
623	+	$C_{12}H_{13}O_{14}Sb_2$	622.84	$[(HCit)(Cit)\bullet Sb_2]^+$
636	-	$C_{18}H_{21}O_{21}Cu$	635.99	$[(H_2Cit)^-(HCit)^{2-}\bullet(H_3Cit)\bullet Cu]^-$
638	+	$C_{18}H_{23}O_{21}Cu$	638.00	$[(H_2Cit)^-(H_3Cit)\bullet(H_3Cit)\bullet Cu]^+$
697	-	$C_{18}H_{19}O_{21}Cu_2$	696.90	$[(HCit)^{2-}(Cit)^{3-}\bullet(H_3Cit)\bullet Cu_2]^-$
699	+	$C_{18}H_{21}O_{21}Cu_2$	698.92	$[(H_2Cit)^-(HCit)^{2-}\bullet(H_3Cit)\bullet Cu_2]^+$
754	-	$CuSbC_{18}H_{18}O_{21}$	753.87	$[(HCit^{2-})_3\bullet Cu\bullet Sb]^-$
756	+	$CuSbC_{18}H_{20}O_{21}$	755.88	$[(HCit)^{2-}(H_2Cit^-)_2\bullet Cu\bullet Sb]^+$
815	-	$Cu_2SbC_{18}H_{16}O_{21}$	814.78	$[(HCit)^{2-}(Cit^{3-})_2\bullet Cu_2\bullet Sb]^-$
817	+	$Cu_2SbC_{18}H_{18}O_{21}$	816.80	$[(Cit^{3-})_3\bullet Cu_2\bullet Sb]^+$

Appendix 3.5. Species identified in solutions of 4.0 mM $Cu(NO_3)_2$ and 1.25 mM Sb_2O_3 in 20.0 mM citric acid at various pH values though ESI-MS in both positive and negative ion mode. Most of the other species identified in Appendix 3.2, 3.3, and 3.4 are present as well in Cu-Sb-Cit solution.

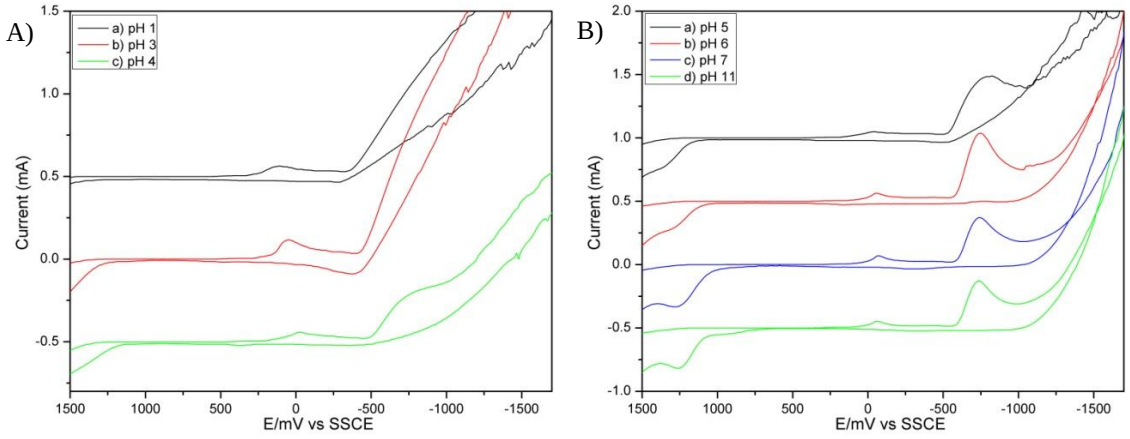

Appendix 3.6. Cyclic voltammograms of 0.4 M citric acid brought to different pH values with potassium hydroxide at a scan rate of 100 mV/s on a 2.01 mm^2 platinum working electrode. Work completed by James Mosby Fall 2006

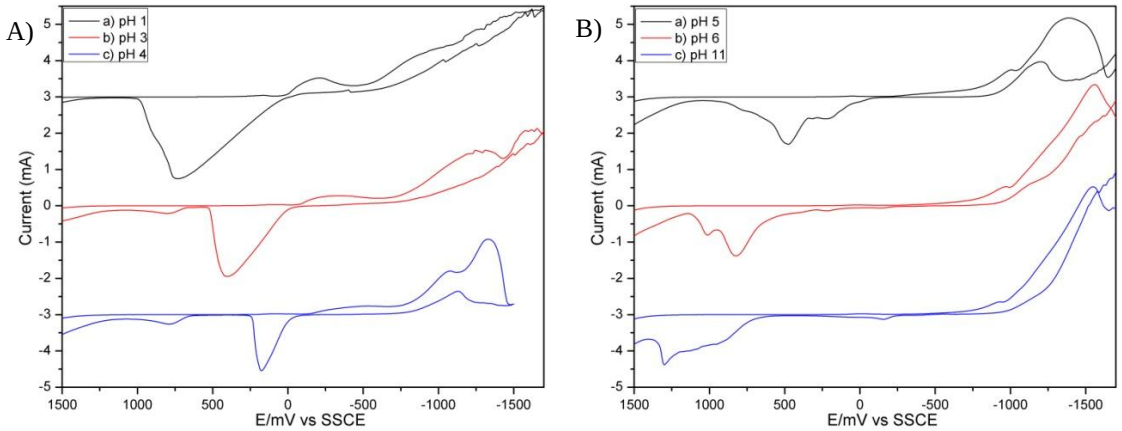

Appendix 3.7. Cyclic voltammograms of 0.08 M $Cu(NO_3)_2$ in 0.4 M citric acid brought to different pH values with potassium hydroxide at a scan rate of 100 mV/s on a 2.01 mm^2 platinum working electrode. Work completed by James Mosby Fall 2006

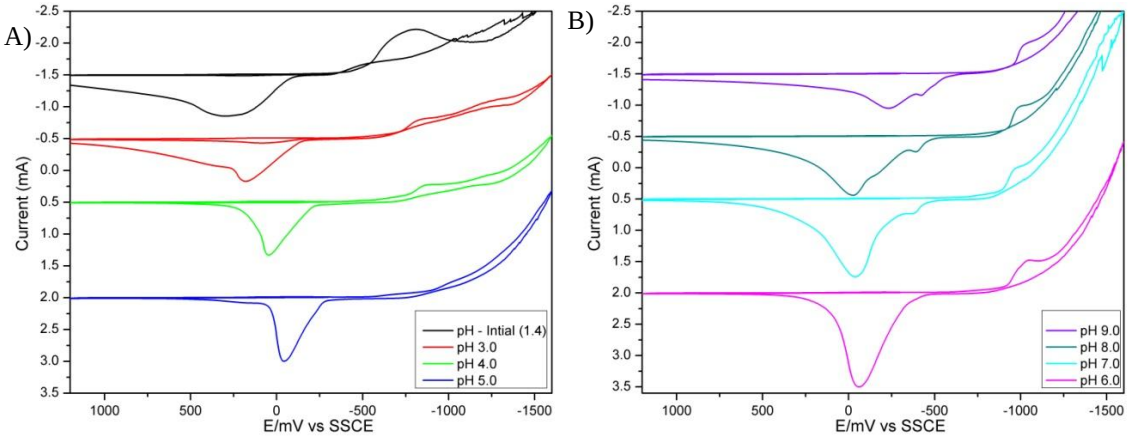

Appendix 3.8. Cyclic voltammograms of 0.025 M Sb_2O_3 in 0.4 M citric acid brought to different pH values with potassium hydroxide at a scan rate of 100 mV/s on a 2.01 mm^2 platinum working electrode.

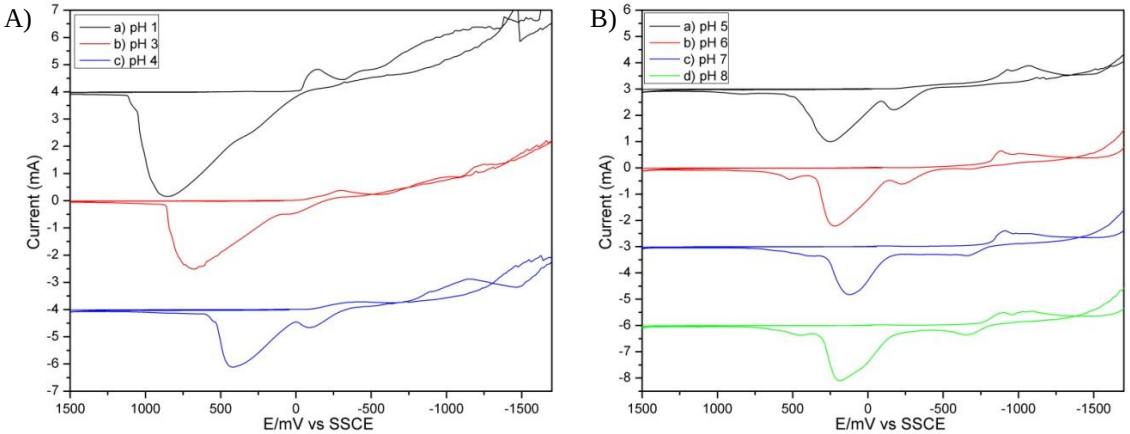

Appendix 3.9. Cyclic voltammograms of 0.08 M $Cu(NO_3)_2$ and 0.025 M Sb_2O_3 in 0.4 M citric acid brought to different pH values with potassium hydroxide at a scan rate of 100 mV/s on a 2.01 mm^2 platinum working electrode. Work completed by James Mosby Fall 2006

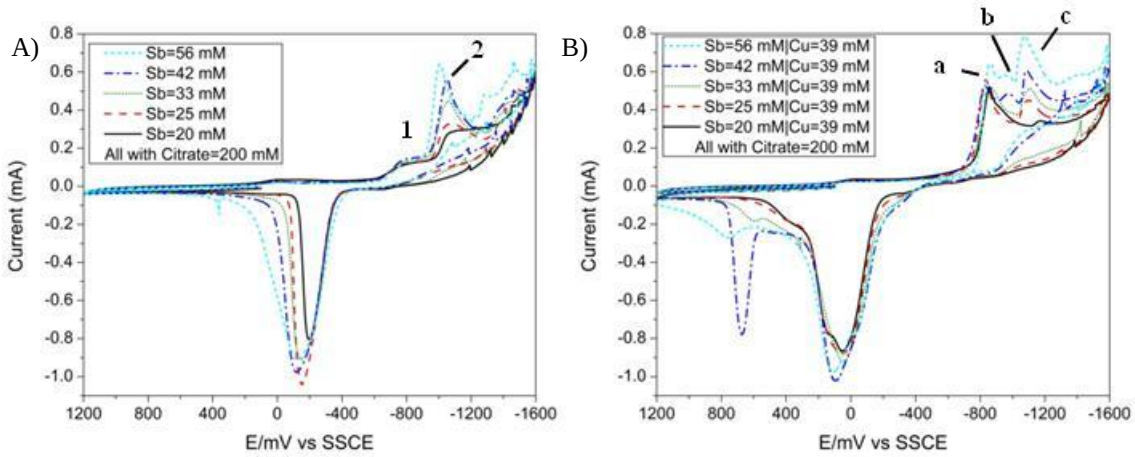

Appendix 3.10. Cyclic voltammograms of different amounts of antimony in citric acid compared to the same amounts of antimony in copper citrate solution at pH 6 as described by Table 3.4. (A) Different concentrations of Sb_2O_3 in 200 mM citric acid (B) Different concentrations of Sb_2O_3 in 39 mM $Cu(NO_3)_2$ in 200 mM citric acid all at pH 6. Done at 75 mV/s on a 2.01 mm^2 platinum working electrode.

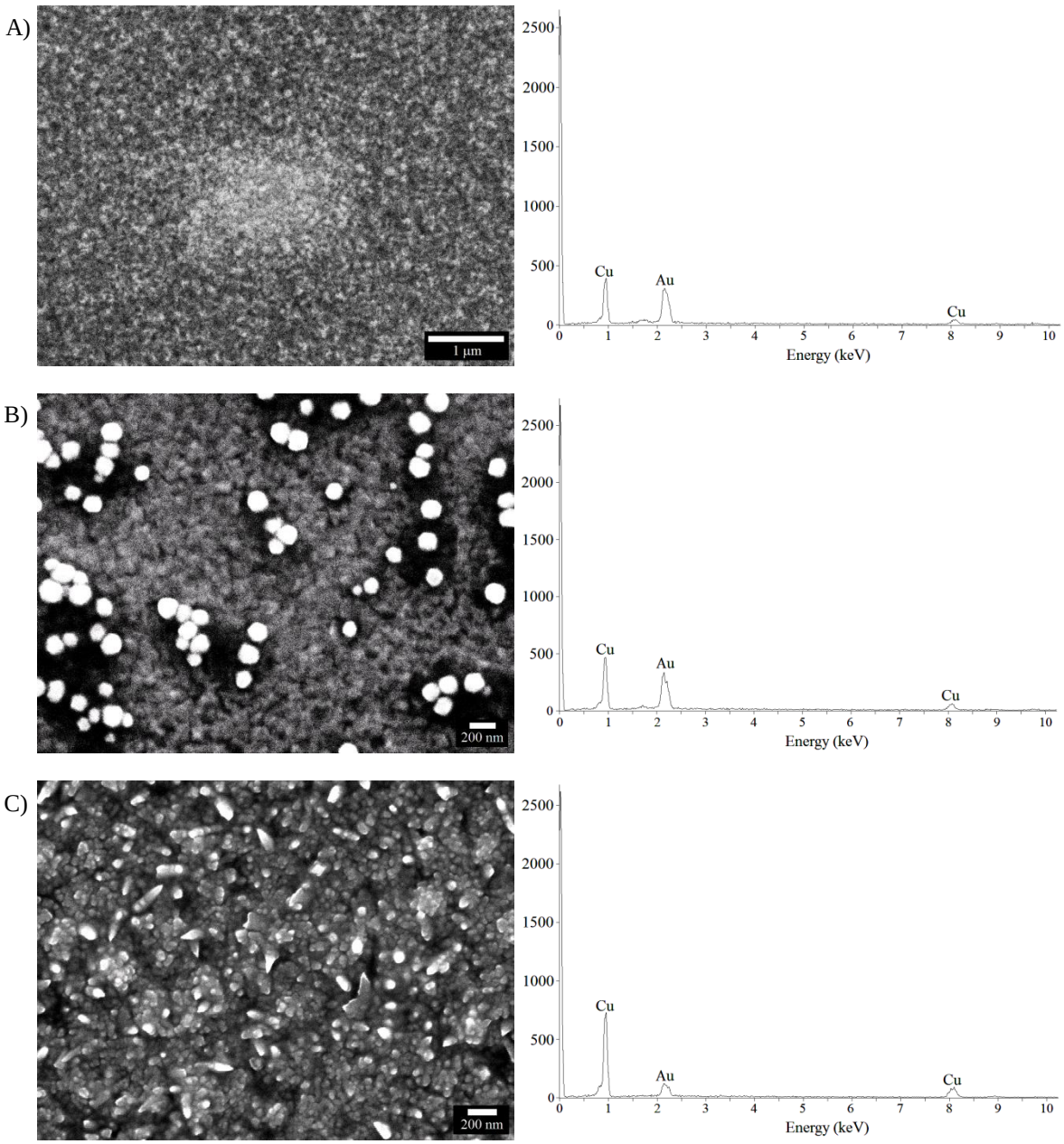

Appendix 4.1. SEM images and corresponding EDS spectra of copper deposition of films deposited onto gold substrate at potentials of A) -300 mV, B) -600 mV, and C) -900 mV which all show copper present.

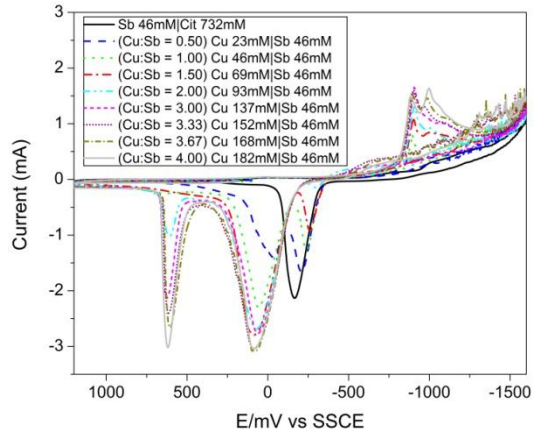

Appendix 4.2. Cyclic Voltammograms of a 0.023 M Sb_2O_3 in 0.38 M citric acid with varying amounts of copper $Cu(NO_3)_2$ added at pH 6 as described in Table 4.2. Done at 75 mV/s on a 2.01 mm^2 platinum working electrode.

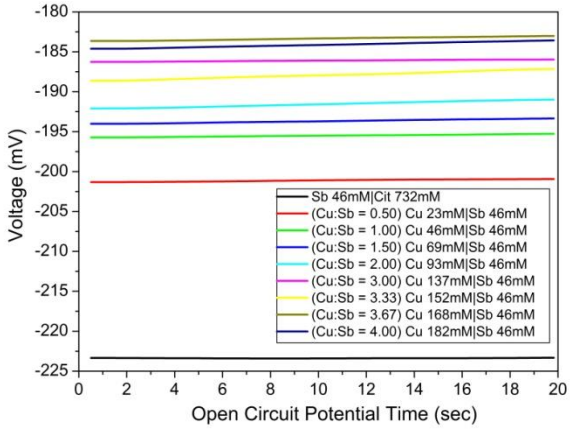

Appendix 4.3. Open circuit potential measurements of a 0.023 M Sb_2O_3 in 0.38 M citric acid with varying amounts of copper $Cu(NO_3)_2$ added at pH 6 as described in Table 4.2.

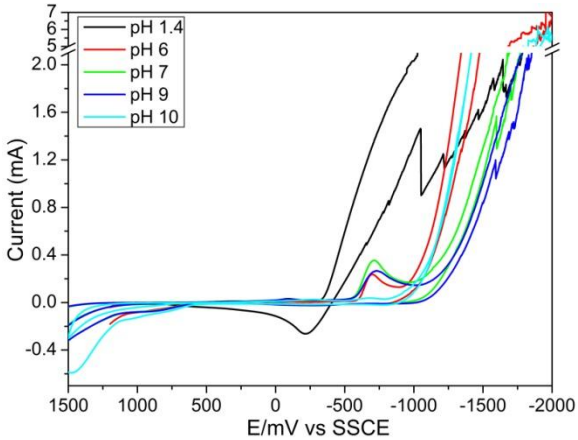

Appendix 4.4. Cyclic voltammograms of 0.08 M $Ni(NO_3)_2$ in 0.4 M citric acid brought to different pH values with potassium hydroxide at a scan rate of 100 mV/s on a 2.01 mm^2 platinum working electrode. Oxidation peak (stripping peak) for pH 1.4 solution is at -300 mV. Nickel citrate does not have a stripping peak at high pH similar to copper citrate. Reduction peak at -600 mV is due to citric acid (see Appendix 3.6).

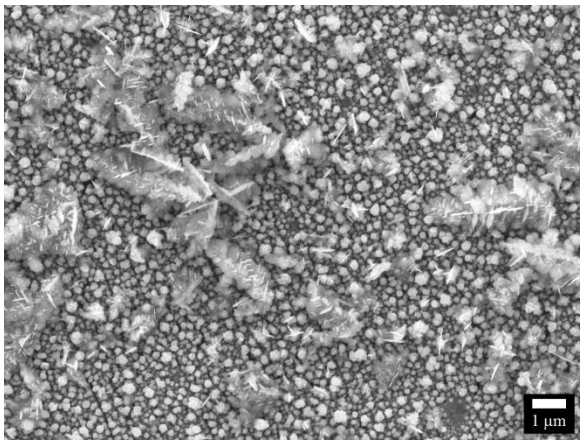

Appendix 4.5. SEM image of iron antimony film co-deposited onto a copper substrate at -1.5 V for 10 minutes from a solution of 0.048 M $Fe(NO_3)_3$ and 0.024 M Sb_2O_3 in 0.38 M citric acid brought to pH 5 with potassium hydroxide.